Ultrahigh Speed Optical Coherence Tomography for Ophthalmic Imaging Applications

by

Jonathan Jaoshin Liu

B.S. Electrical Engineering
National Taiwan University, 2005

S.M. Electrical Engineering and Computer Science
Massachusetts Institute of Technology, 2008

Submitted to the

DEPARTMENT OF ELECTRICAL ENGINEERING AND COMPUTER SCIENCE

in partial fulfillment of the requirements for the degree of

DOCTOR OF PHILOSOPHY IN ELECTRICAL ENGINEERING AND COMPUTER SCIENCE

at the

MASSACHUSETTS INSTITUTE OF TECHNOLOGY

February 2014

Signature of Author: _____
Department of Electrical Engineering and Computer Science
January 22, 2014

Certified by: _____
James G. Fujimoto
Professor of Electrical Engineering and Computer Science
Thesis Supervisor

Accepted by: _____
Leslie A. Kolodziejski
Chair, Department Committee on Graduate Students

Ultrahigh Speed Optical Coherence Tomography for Ophthalmic Imaging Applications

by

Jonathan Jaoshin Liu

Submitted to the Department of Electrical Engineering and Computer Science in January 2014 in Partial Fulfillment of the Requirements for the Degree of Doctor of Philosophy in Electrical Engineering and Computer Science

ABSTRACT

Optical coherence tomography (OCT) is a non-contact, non-invasive, micron-scale optical imaging technology that has become a standard clinical tool in ophthalmology. Fourier domain OCT detection methods have enabled higher sensitivity and imaging speeds compared to previous generation time-domain OCT. Spectral / Fourier domain OCT (SD-OCT) detects the interference spectrum using a broadband light source and spectrometer. Swept-source / Fourier domain OCT (SS-OCT) detects the interference spectrum over time using a wavelength-swept laser. Current standard commercial ophthalmic clinical systems based on SD-OCT technology have imaging speeds of 20,000 – 40,000 axial scans per second and axial resolutions of 5 – 7 μm.

In this thesis, ultrahigh speed OCT for ophthalmic imaging applications are presented. SD-OCT systems using high speed CMOS camera technology can achieve imaging speeds over 70,000 axial scans per second. Axial resolutions better than 3 μm can be achieved with multiplexed broadband superluminescent diodes. A novel registration motion-correction algorithm for volumetric OCT datasets reducing motion artifacts and improving signal quality is investigated. Ultrahigh speed, ultrahigh resolution SD-OCT ophthalmic imaging applications including small animal retinal imaging and clinical imaging of age-related macular degeneration (AMD) are illustrated. SS-OCT systems using short cavity wavelength-swept laser light sources can achieve imaging speeds over 100,000 axial scans per second with 6 μm axial resolution for small animal and clinical imaging. The high sensitivity of SS-OCT enables enhanced vitreous imaging, visualizing features in the vitreous and vitreoretinal interface. Finally, a new vertical cavity surface-emitting (VCSEL) technology based wavelength-swept laser light source SS-OCT system with tunable speed and wavelength range as well as long coherence length enabling ultrahigh speed and ultralong range OCT imaging applications is demonstrated. In addition to comprehensive structural imaging, the emergence of functional OCT imaging of retinal blood flow using ultrahigh speed OCT may also improve the understanding of ocular disease pathogenesis. Therefore, ultrahigh speed OCT is a promising tool for the diagnosis and management of diseases in ophthalmology.

Thesis Supervisor: James G. Fujimoto

Title: Elihu Thomson Professor of Electrical Engineering and Computer Science

ACKNOWLEDGEMENTS

This thesis was made possible by the collaboration of my outstanding colleagues who have each made significant contribution to the work involved. Many of them have also laid the groundwork for the field of optical coherence tomography. I would like to especially thank Prof. James Fujimoto for the opportunity of working in a world-class laboratory and excellent research group. It has truly been an opportunity of a lifetime. It has also been a privilege working closely with amazing clinical and scientific collaborators at the New England Eye Center and the University of Pittsburgh Medical Center Eye Center, headed by Dr. Jay Duker and Dr. Joel Schuman.

Throughout my time at MIT, I have learned a great deal from each and every extraordinary team member. I have spent the most time working with Dr. Ireneusz Grulkowski and Dr. Benjamin Potsaid, providing me guidance not only with experiments but also with life. Dr. Vivek Srinivasan, Dr. Iwona Gorczynska, Dr. Bernhard Baumann, Dr. Yueli Chen, Dr. Maciej Wojtkowski, Dr. Robert Huber, and Dr. Tony Ko have paved the way before me and have personally passed on extensive knowledge to me. It has also been a great experience working with Martin Kraus, WooJhon Choi, Chen Lu, ByungKun Lee, Kathrin Mohler, Dr. Al-Hafeez Dhalla, and Dr. Zhao Wang on projects in ophthalmology as well as Hsiang-Chieh Lee, Osman Ahsen, Dr. Tsung-Han Tsai, Dr. Chao Zhou, and Dr. Aaron Aguirre on projects in microscopy and endoscopy. I thank Dr. Desmond Adler, Dr. Umit Demirbas, Dr. Yu Chen, Dr. Shu-Wei Huang, Dr. Jung-Ho Chung, Dr. Yu Gu, Dr. Alphan Sennaroglu, Dr. Yuankai Tao, Dr. Michael Giacomelli, Kaicheng Liang, Eric Moult, Ning Zhang, Duo Li, and Jing Wang for being great labmates. It has been a pleasure working with Dr. Mehreen Adhi, Dr. Andre Witkin, Dr. Nadia Waheed, Dr. Daniela Ferrara, Dr. Caroline Baumal, Dr. Chandru Krishnan, Dr. Nora Laver, Dr. Elias Reichel, Dr. Tarek Alasil, Dr. Jason Zhang, Dr. Ahmad Alwassia, Dr. Lauren Branchini, Dr. Caio Regatieri, Dr. Varsha Manjunath, Dr. Laurel Vuong, Dr. Alan Sull, Dr. Joseph Ho, Dr. Royce Chen, and Dr. Bryan Monson at the New England Eye Center, Dr. Gadi Wollstein, Dr. Hiroshi Ishikawa, Dr. Richard Bilonick, Dr. Bo Wang, Jessica Nevins, and Dr. Larry Kagemann at the University of Pittsburgh Medical Center, Dr. Yali Jia, Dr. Ou Tan, Dr. Yimin Wang, Dr. Jason Tokayer, Dr. Yan Li, and Dr. David Huang at the Oregon Health Science University, as well as Allen Clermont and Dr. Edward Feener at the Joslin Diabetes Center. I want to thank Prof. Erich Ippen, Prof. Franz Kaertner, Prof. Fatih Yanik, Ms. Dorothy Fleischer, and Ms. Donna Gale for being part of my delightful MIT experience.

My family and friends have always been my biggest supporters. Thank you, Mom and Dad, for everything that I have and everything that I am. And thank you, Yu-Chieh, for your everlasting support, companionship, and patience. Thanks to all my wonderful friends, especially Hsin-Hsiao and Yu-Pei for taking care of me for a couple years as well as Ting-Sheng and Lu-Di for many random phone calls and visits from Taiwan.

你要專心仰賴耶和華，

不可倚靠自己的聰明，

在你一切所行的事上都要認定他，

他必指引你的路。

箴言 3:5-6

TABLE OF CONTENTS

CHAPTER 1

Introduction

1.1 Overview

The work presented in this thesis aims to develop ultrahigh speed optical coherence tomography technology for applications in the field of ophthalmology. Optical coherence tomography (OCT) is a medical imaging technology that can perform micron scale imaging of microstructure in biological tissues *in situ* and in real time.[1-7] OCT is analogous to ultrasound B-mode imaging, except that it measures the echo time delay and intensity of back-reflected or backscattered light rather than acoustical waves. Cross-sectional and three-dimensional (3D) images are generated by scanning an optical beam across the tissue and measuring the echo time delay and intensity of backscattered light. In ophthalmology, OCT provides information impossible to obtain by any other noninvasive technique. OCT is now a clinical standard for diagnosis and management of ocular diseases.[8, 9] OCT has also demonstrated its potential for imaging a wide range of tissues other than the eye including arterial, gastrointestinal, urinary, respiratory, and female reproductive tracts.[10-14] In cardiology, intravascular OCT is an emerging imaging tool for clinical assessment. OCT has also been applied to developmental biology, surgical guidance, and neuroscience applications.[15-18]

Since the propagation speed of light is much faster than photodetector response times, light echo time delays cannot be measured electronically as in ultrasound. Instead, OCT uses a fundamentally different technique based on a Michelson interferometer, also known as low-coherence interferometry. Figure 1.1 illustrates the principle of low-coherence interferometry with a basic time-domain OCT system schematic implementing a simple Michelson interferometer. Light from a source is divided into a reference beam and a sample probe beam. Reflected light from the sample arm is recombined with the reflected light from the reference arm at a photodetector to produce interference fringes. If the light source is monochromatic, interference is seen over a wide range of sample and reference arm path length mismatches. When using a low-coherence broadband light source, interference is only seen when the reference arm path length matches the sample arm path length to within the coherence length of the light source. As the reference arm path is scanned, interference fringes detected with the photodetector generate a profile of backscattering versus depth from the sample arm. Low-coherence light can be generated by superluminescent semiconductor diodes or other sources, such as solid state lasers. Higher axial resolution can be achieved by increasing the bandwidth of the light source.[7] Low-coherence interferometry permits the echo delay time (or optical path length) and magnitude of the light reflected from internal tissue microstructures to be measured with extremely high accuracy and sensitivity.

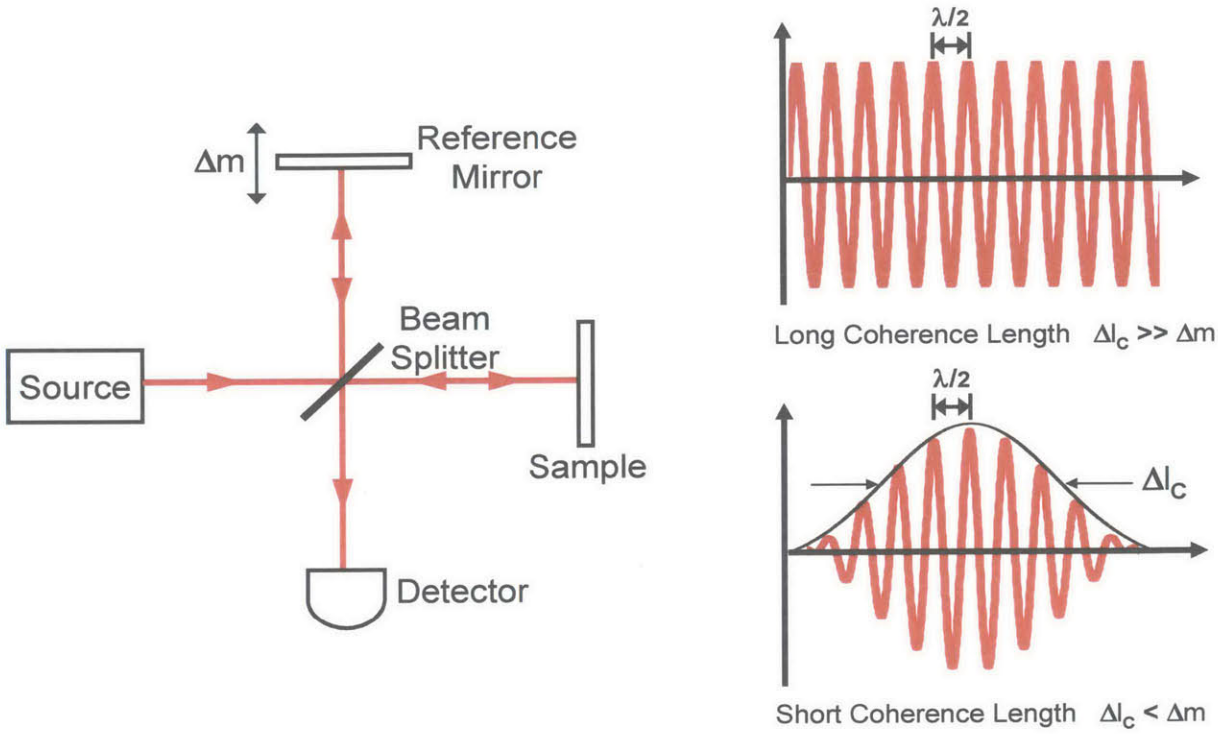

Figure 1.1 Schematic illustrating the principle of low-coherence interferometry using a Michelson interferometer. Light is divided into the reference and sample paths and the reflected light is recombined. For monochromatic light sources, interference is seen over a wide range of sample and reference arm path length mismatches. For low-coherence broadband light sources, interference is only seen when the reference path length matches the sample path length to within the coherence length of the light source.

The principle of generating two-dimensional images and three-dimensional datasets using OCT is shown in Figure 1.2. Scanning the reference arm path length and plotting the envelope of the interference as a function of this path length generates a map of the backscattered light intensity from the sample. Additionally, translating the sample with respect to the incident beam or scanning the incident beam across the sample results in a two-dimensional array dataset which represents the optical backscattering or reflections within a cross-sectional slice of the sample. Successive adjacent two-dimensional cross-sectional slices form a three-dimensional dataset of the sample.

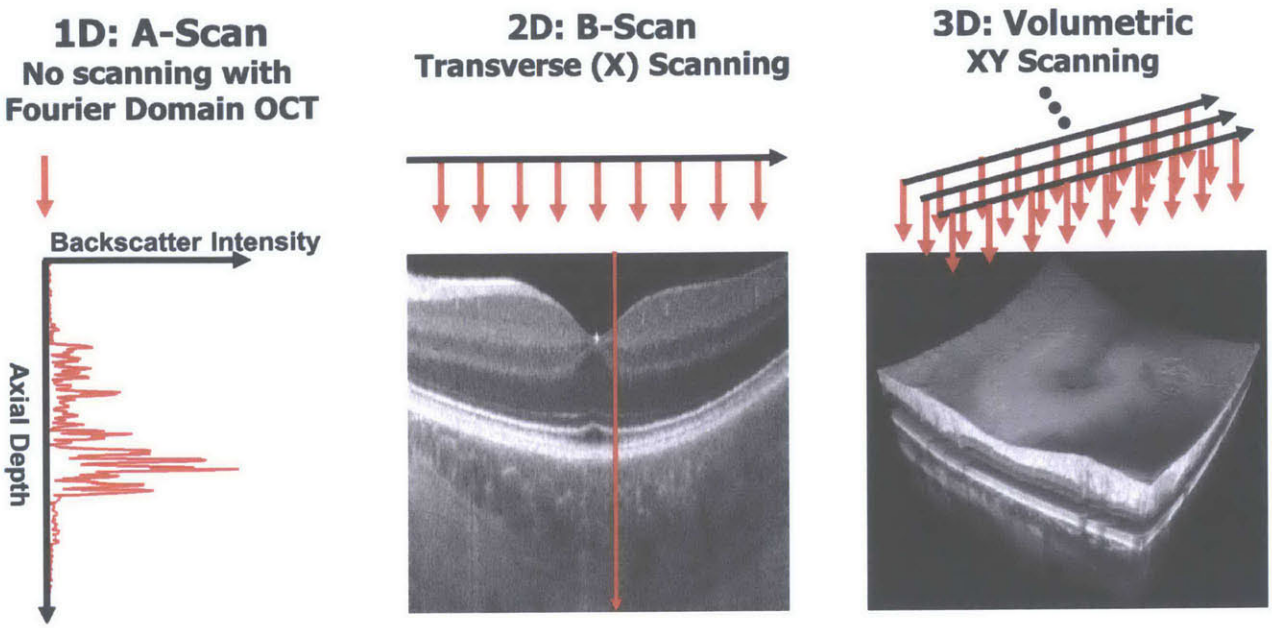

Figure 1.2 Formation of an OCT image and OCT dataset. The backscattered intensity is mapped as a function of depth known as an axial scan or an A-scan. A two-dimensional image, also known as a B-scan, is formed by scanning the incident beam with respect to the sample. A three-dimensional dataset is formed by acquiring successive adjacent two-dimensional images over the sample.

1.2 Optical Coherence Tomography in Ophthalmology

Optical coherence tomography (OCT) was first invented and reported in 1991 imaging the human retina and coronary artery in vitro by Dr. David Huang in Prof. James G. Fujimoto's group at Massachusetts Institute of Technology.[1] In collaboration with Dr. Carmen A. Puliafito and Dr. Joel S. Schuman of the New England Eye Center and Tufts University School of Medicine, and Eric. A. Swanson of MIT Lincoln Laboratory, OCT was further developed and demonstrated for in vivo ophthalmic imaging.[3, 19, 20] Clinical imaging studies on ocular diseases began in 1993 using a clinical OCT prototype deployed at the New England Eye Center. The first OCT studies investigated a wide range of ophthalmic diseases including macular holes, glaucoma, age-related macular degeneration, macular edema, and diabetic retinopathy.[3, 20-25] OCT can also provide direct information on the dimensions of retinal structures, thereby permitting the quantitative measurement of retinal nerve fiber layer (RNFL) thickness for the diagnosis and monitoring of glaucoma.[26, 27] The protocol that was developed for RNFL assessment in the first studies demonstrating OCT for nerve fiber layer assessment and diagnosis of glaucoma have become clinical standards and are used in the commercial OCT systems today. In addition, the OCT scanning

protocol developed in initial studies mapping macular thickness in macular edema has also become a clinical standard.[21, 25]

Since these initial studies in ophthalmology, OCT technology was patented and subsequently transferred to industry. Carl Zeiss Meditec first introduced its time-domain OCT product to the ophthalmic market in 1996. The first and second generation time-domain OCT products (OCT1/2) gained critical clinical evidence and validation on utility with about 400 units shipped. The third generation time-domain OCT model (Stratus OCT) was introduced in 2002 and became a gold standard imaging device for ophthalmology with more than 9,000 units in the marketplace today. This standard clinical OCT imaging system has a 10 μm axial resolution and can acquire a 512 axial scan (transverse pixel) image in 1.3 seconds.

Fourier domain OCT detection methods have enabled dramatic increases in speed and sensitivity over conventional time-domain OCT detection methods.[28-30] In comparison to time-domain OCT, these methods are called "Fourier domain" because echo time delays are measured by Fourier transforming the interference spectrum of the light and do not require mechanical scanning of the reference path length in time. There are two embodiments of Fourier domain OCT. The first embodiment uses a broadband light source and is known as "spectral / Fourier domain" OCT because the interference spectrum is detected by a high speed, high resolution spectrometer. The second embodiment uses a frequency tunable light source and a photodiode or pair of photodiodes for detection and is known as "swept-source / Fourier domain" OCT.

The first commercial ophthalmic spectral / Fourier domain OCT system developed by Optovue was approved by the FDA in 2006. Several other systems soon followed. Commercial spectral / Fourier domain OCT systems have ~50 to 175 to times faster imaging speed and up to 3 times better axial resolution than commercial time-domain OCT. Higher imaging speed enables improved retinal coverage, increased scan density, reduced motion artifacts, and more accurate visualization of topography. Better axial resolution enables visualization of the architectural morphology of internal retinal layers. With these advances, it is possible to generate a series of high pixel density OCT images that visualize retinal microstructure with excellent quality while preserving the true retinal topography. Three-dimensional OCT data that achieves comprehensive cross-sectional coverage of the retina can also be acquired and registered to fundus photos. These advantages over time-domain OCT have made spectral / Fourier domain OCT the new gold standard for clinical ophthalmic imaging.

Swept-source / Fourier domain OCT systems typically operate in longer wavelengths compared to commercial time-domain and spectral / Fourier domain systems. Longer wavelength light provides

improved penetration into tissue, enables better detection through ocular opacities, and is invisible to the subject. Swept-source / Fourier domain OCT also has longer imaging range, improved sensitivity with imaging depth, and reduced fringe washout compared to spectral /Fourier domain OCT. Recently, commercial ophthalmic swept-source / Fourier domain OCT systems have been developed by several companies and are available for sale in Japan and Europe.

Table 1.1 Commercial ophthalmic OCT devices available for sale in the US for retinal imaging.

Device	Manufacturer	Axial Resolution	Imaging Speed	Imaging Range
StratusOCT	Carl Zeiss Meditec	10 μm	400 A-scans per second	2 mm
RTVUE-100	Optovue	5 μm	26,000 A-scans per second	2.3 mm
SDOCT	Bioptigen	6 μm	20,000 A-scans per second	2.2 mm
Cirrus HD-OCT	Carl Zeiss Meditec	5 μm	27,000 A-scans per second	2 mm
Optos OCT SLO	Optos	5-6 μm	27,000 A-scans per second	2.3 mm
3D-OCT 1000 / 3D-OCT 2000	Topcon	5-6 μm	18,000 / 27,000 A-scans per second	1.68 / 2.3 mm
Optopol SOCT Copernicus	Canon	5 μm	27,000 A-scans per second	2 mm
Spectralis HRA+OCT	Heidelberg Engineering	7 μm	40,000 A-scans per second	1.9 mm
RTVue XR	Optovue	5 μm	70,000 A-scans per second	3 mm

1.3 Scope of Thesis

The aims of this thesis are as follows. 1) To demonstrate ultrahigh speed, ultrahigh resolution spectral / Fourier domain OCT and ultrahigh speed swept-source / Fourier domain OCT imaging for small animal imaging. 2) To develop ultrahigh speed, ultrahigh resolution spectral / Fourier domain OCT and ultrahigh speed swept-source / Fourier domain OCT imaging systems for clinical deployment. 3) To investigate the reproducibility of a novel registration motion-correction algorithm. 4) To study the morphological changes in the retina observed in eyes with age-related macular degeneration using motion corrected, three-dimensional, ultrahigh speed, ultrahigh resolution spectral / Fourier domain OCT datasets. 5) To demonstrate enhanced vitreous imaging using motion corrected, three-dimensional, ultrahigh speed swept-source / Fourier domain OCT and investigate vitreal and vitreoretinal features observed in healthy eyes. 6) To develop ultrahigh speed swept-source / Fourier domain OCT using vertical-cavity surface-emitting laser light sources and demonstrate ultralong range OCT imaging.

The thesis is organized according to these aims. Chapter 2 presents a summary of system designs and imaging results using ultrahigh speed, ultrahigh resolution spectral / Fourier domain OCT in small animal and human eyes. Chapter 3 describes a novel registration motion-correction algorithm and presents results from a reproducibility study using the algorithm to perform retinal nerve fiber layer thickness measurements in normal and glaucomatous eyes. Chapter 4 presents initial results from a pilot study of non-exudative (dry) age-related macular degeneration using motion-corrected three-dimensional, ultrahigh speed, ultrahigh resolution spectral / Fourier domain OCT. Chapter 5 presents small animal and human ultrahigh speed swept-source / Fourier domain OCT imaging. Chapter 5 also describes the design of clinical ultrahigh speed swept-source / Fourier domain OCT systems. Chapter 6 describes enhanced vitreous imaging using motion-corrected, three-dimensional, ultrahigh speed swept-source / Fourier domain OCT. Chapter 6 also presents results from an observational study imaging features in the vitreous and vitreoretinal interface in healthy eyes. Chapter 7 details the development of ultrahigh speed swept-source / Fourier domain OCT using vertical-cavity surface-emitting laser light source technology, which enables improved imaging speed, imaging range, and multimodal ophthalmic imaging of the anterior eye, posterior eye, and full eye length. Chapter 8 concludes the thesis by providing perspectives for future studies.

1.4 References

1. Huang D, Swanson EA, Lin CP, Schuman JS, Stinson WG, Chang W, Hee MR, Flotte T, Gregory K, Puliafito CA, Fujimoto JG. Optical Coherence Tomography. Science. 1991;254(5035):1178-81. PubMed PMID: ISI:A1991GQ83400038.

2. Swanson EA, Huang D, Hee MR, Fujimoto JG, Lin CP, Puliafito CA. High-speed optical coherence domain reflectometry. Opt Lett. 1992;17:151-3.

3. Hee MR, Izatt JA, Swanson EA, Huang D, Schuman JS, Lin CP, Puliafito CA, Fujimoto JG. Optical coherence tomography of the human retina. Arch Ophthalmol. 1995;113(3):325-32. PubMed PMID: PMID: 7887846; Medline: 95194246 Provider: OCLC.

4. Fujimoto JG, Brezinski ME, Tearney GJ, Boppart SA, Bouma B, Hee MR, Southern JF, Swanson EA. Optical biopsy and imaging using optical coherence tomography. Nat Med. 1995;1(9):970-2. PubMed PMID: PMID: 7585229; Medline: 96071609 Provider: OCLC.

5. Brezinski ME, Tearney GJ, Bouma BE, Izatt JA, Hee MR, Swanson EA, Southern JF, Fujimoto JG. Optical coherence tomography for optical biopsy. Properties and demonstration of vascular pathology. Circulation. 1996;93(6):1206-13. PubMed PMID: PMID: 8653843; Medline: 96220131 Provider: OCLC.

6. Tearney GJ, Brezinski ME, Bouma BE, Boppart SA, Pitvis C, Southern JF, Fujimoto JG. In vivo endoscopic optical biopsy with optical coherence tomography. Science. 1997;276(5321):2037-9.

7. Drexler W, Morgner U, Kartner FX, Pitris C, Boppart SA, Li XD, Ippen EP, Fujimoto JG. In vivo ultrahigh-resolution optical coherence tomography. Opt Lett. 1999;24(17):1221-3.

8. Schuman JS, Puliafito CA, Fujimoto JG, Duker JS. Optical coherence tomography of ocular diseases. 3rd ed. Thorofare, NJ: SLACK Inc.; 2013.

9. Yanoff M, Duker JS. Ophthalmology. 4th ed. Philadelphia, PA: Saunders; 2013.

10. Tearney GJ, Brezinski ME, Boppart SA, Bouma BE, Weissman N, Southern JF, Swanson EA, Fujimoto JG. Catheter-based optical imaging of a human coronary artery. Circulation. 1996;94(December):3013.

11. Bouma BE, Tearney GJ, Compton CC, Nishioka NS. High-resolution imaging of the human esophagus and stomach in vivo using optical coherence tomography. Gastrointest Endosc. 2000;51(4) Pt 1:467-74. PubMed PMID: PMID: 10744824; Medline: 20209224 Provider: OCLC.

12. Pitris C, Brezinski ME, Bouma BE, Tearney GJ, Southern JF, Fujimoto JG. High resolution imaging of the upper respiratory tract with optical coherence tomography: a feasibility study. Am J Resp Crit Care. 1998;157(5) Pt 1:1640-4. PubMed PMID: PMID: 9603149; Medline: 98264288 Provider: OCLC.

13. Tearney GJ, Brezinski ME, Southern JF, Bouma BE, Boppart SA, Fujimoto JG. Optical biopsy in human urologic tissue using optical coherence tomography. The Journal of urology. 1997;157(5):1915-9. PubMed PMID: PMID: 9112562; Medline: 97266839 Provider: OCLC.

14. Escobar PF, Belinson JL, White A, Shakhova NM, Feldchtein FI, Kareta MV, Gladkova ND. Diagnostic efficacy of optical coherence tomography in the management of preinvasive and invasive cancer of uterine cervix and vulva. Int J Gynecol Cancer. 2004;14(3):470-4. PubMed PMID: ISI:000221794500008.

15. Boppart SA, Bouma BE, Brezinski ME, Tearney GJ, Fujimoto JG. Imaging developing neural morphology using optical coherence tomography. J Neurosci Methods. 1996;70(1):65-82.

16. Boppart SA, Brezinski ME, Bouma BE, Tearney GJ, Fujimoto JG. Investigation of developing embryonic morphology using optical coherence tomography. Developmental biology. 1996;177(1):54-63. PubMed PMID: PMID: 8660876; Medline: 96299421 Provider: OCLC.

17. Boppart SA, Bouma BE, Pitris C, Tearney GJ, Fujimoto JG, Brezinski ME. Forward-imaging instruments for optical coherence tomography. Opt Lett. 1997;22(21):1618-20.

18. Boppart SA, Bouma BE, Pitris C, Tearney GJ, Southern JF, Brezinski ME, Fujlmoto JG. Intraoperative assessment of microsurgery with three-dimensional optical coherence tomography. Radiology. 1998;208(1):81-6.

19. Swanson EA, Izatt JA, Hee MR, Huang D, Lin CP, Schuman JS, Puliafito CA, Fujimoto JG. In vivo retinal imaging by optical coherence tomography. Opt Lett. 1993;18(21):1864-6.

20. Puliafito CA, Hee MR, Lin CP, Reichel E, Schuman JS, Duker JS, Izatt JA, Swanson EA, Fujimoto JG. Imaging of macular diseases with optical coherence tomography. Ophthalmology. 1995;102(2):217-29. PubMed PMID: PMID: 7862410; Medline: 95166518 Provider: OCLC.

21. Hee MR, Puliafito CA, Wong C, Duker JS, Reichel E, Rutledge B, Schuman JS, Swanson EA, Fujimoto JG. Quantitative Assessment of Macular Edema with Optical Coherence Tomography. Arch Ophthalmol. 1995;113(8):1019-29. PubMed PMID: ISI:A1995RN89100025.

22. Hee MR, Puliafito CA, Wong C, Duker JS, Reichel E, Schuman JS, Swanson EA, Fujimoto JG. Optical coherence tomography of macular holes. Ophthalmology. 1995;102(5):748-56. PubMed PMID: PMID: 7777274; Medline: 95296060 Provider: OCLC.

23. Hee MR, Puliafito CA, Wong C, Reichel E, Duker JS, Schuman JS, Swanson EA, Fujimoto JG. Optical coherence tomography of central serous chorioretinopathy. Am J Ophthalmol. 1995;120(1):65-74. PubMed PMID: PMID: 7611331; Medline: 95335718 Provider: OCLC.

24. Hee MR, Baumal CR, Puliafito CA, Duker JS, Reichel E, Wilkins JR, Coker JG, Schuman JS, Swanson EA, Fujimoto JG. Optical coherence tomography of age-related macular degeneration and choroidal neovascularization. Ophthalmology. 1996;103(8):1260-70. PubMed PMID: PMID: 8764797; Medline: 96350288 Provider: OCLC.

25. Hee MR, Puliafito CA, Duker JS, Reichel E, Coker JG, Wilkins JR, Schuman JS, Swanson EA, Fujimoto JG. Topography of diabetic macular edema with optical coherence tomography. Ophthalmology. 1998;105(2):360-70. doi: Doi 10.1016/S0161-6420(98)93601-6. PubMed PMID: ISI:000071932600032.

26. Schuman JS, Hee MR, Puliafito CA, Wong C, Pedut-Kloizman T, Lin CP, Hertzmark E, Izatt JA, Swanson EA, Fujimoto JG. Quantification of nerve fiber layer thickness in normal and glaucomatous eyes using optical coherence tomography. Arch Ophthalmol. 1995;113(5):586-96. PubMed PMID: PMID: 7748128; Medline: 95267006 Provider: OCLC.

27. Schuman JS, PedutKloizman T, Hertzmark E, Hee MR, Wilkins JR, Coker JG, Puliafito CA, Fujimoto JG, Swanson EA. Reproducibility of nerve fiber layer thickness measurements using optical coherence tomography. Ophthalmology. 1996;103(11):1889-98. PubMed PMID: ISI:A1996VU09700040.

28. Leitgeb R, Hitzenberger CK, Fercher AF. Performance of Fourier domain vs. time domain optical coherence tomography. Optics Express. 2003;11(8):889-94.

29. de Boer JF, Cense B, Park BH, Pierce MC, Tearney GJ, Bouma BE. Improved signal-to-noise ratio in spectral-domain compared with time-domain optical coherence tomography. Opt Lett. 2003;28(21):2067-9. PubMed PMID: 14587817.

30. Choma MA, Sarunic MV, Yang CH, Izatt JA. Sensitivity advantage of swept source and Fourier domain optical coherence tomography. Optics Express. 2003;11(18):2183-9. PubMed PMID: ISI:000185185000012.

CHAPTER 2

Spectral / Fourier Domain Optical Coherence Tomography

2.1 Principles of Spectral / Fourier Domain Optical Coherence Tomography

In spectral / Fourier domain OCT, interference signal between the sample and reference arm light is detected by a spectrometer using a photodiode array detector or a high speed multi-element CCD or CMOS detector. The delay and magnitude of the optical reflections from the sample can be determined by Fourier transforming the spectral interference signal. Spectral / Fourier domain OCT allows reconstruction of the depth resolved scattering profile at a certain point on the sample using the optical spectrum modulation caused by interference of light beams.

In spectral / Fourier domain OCT, the photoelectron density I at the CCD detector is given by:

$$I = \frac{\eta(\omega)T}{2\eta_0\hbar\omega}\left[\left|A_R(\omega)\right|^2 + \left|A_s(\omega)\right|^2 + 2\,\mathrm{Re}\left\{E_S(\omega)E_R^*(\omega)\right\}\right] = I_{\mathrm{DC}} + I_{\mathrm{int}} \tag{2.1}$$

Hence, the interference signal can be written as:

$$I_{\mathrm{int}} \propto \mathrm{Re}\left\{E_R(\omega)E_S(\omega)^*\right\} = \mathrm{Re}\left\{S(\omega)e^{-j\Delta\phi(\omega)}\right\} \tag{2.2}$$

where $S(\omega) = A_R(\omega)A_S(\omega)$ and $\Delta\phi(\omega) = 2k_R(\omega)l_R - 2k_S(\omega)l_S$.

If the total field from the sample arm is assumed to be composed of a superposition of fields generated by reflections from different delays or depths, equation (2.2) then becomes:

$$I_{\mathrm{int}} \propto \mathrm{Re}\left\{E_R(\omega)\sum_n E_{S,n}(\omega)^*\right\} = \mathrm{Re}\left\{\sum_n S_n(\omega)e^{-j\Delta\phi_n(\omega)}\right\} \tag{2.3}$$

with

$$S_n(\omega) = A_R(\omega)A_{S,n}(\omega) \tag{2.4}$$

and

$$\Delta\phi_n(\omega) = 2k_R(\omega)l_R - 2k_S(\omega)l_{S,n} \tag{2.5}$$

In the case where the sample and reference arms consist of non-dispersive material $k_R(\omega) = k_S(\omega) = k(\omega) = k(\omega_0) + k'(\omega_0)(\omega - \omega_0)$ and $1/k'(\omega_0) = c$. The phase mismatch in equation (2.5) becomes

$$\Delta\phi_n(\omega) = k(\omega_0)\cdot 2\Delta l_n + k'(\omega_0)(\omega-\omega_0)\cdot 2\Delta l_n = \frac{2\Delta l_n\cdot\omega}{c} + \Phi_n(\Delta l_n) \tag{2.6}$$

where $\Delta l_n = l_{S,n} - l_R$ and $\Phi_n(\Delta l_n)$ is the ω independent constant phase term. Therefore, equation (2.3) can be rewritten as:

$$I_{\text{int}} \propto \sum_n S_n(\omega)\cos(\frac{2\Delta l_n \cdot \omega}{c} + \Phi_n(\Delta l_n)) \tag{2.7}$$

The mismatch of optical path length between the reference and sample arms can be obtained by calculating the inverse Fourier transform of equation (2.7):

$$\mathrm{I} = \mathbb{F}^{-1}\{I_{\text{int}}(\omega)\} \propto \sum_n e^{-i\Phi_n(\Delta l_n)} G_n(z) \otimes \delta(z \pm 2\Delta l_n) \tag{2.8}$$

Assuming that parameters such as dispersion and the spectral transfer function are depth-independent, the resolution of spectral / Fourier domain OCT is therefore determined by $G_n(z) = \int_{-\infty}^{\infty} S_n(\omega)\frac{d\omega}{2\pi}$, linked to the Wiener-Khinchin theorem. The resolution equation is same for time domain and spectral / Fourier domain OCT. Notice the "mirror images" expressed by $\delta(z \pm \Delta l_n)$, which results in the total number of pixels carrying unique information about the axial scan being reduced by a factor of two. This is because the Fourier transform of the real spectrum has conjugate symmetry about the zero delay.[1] Assuming that the light source has a Gaussian power spectral density $S(\omega - \omega_0) = \sqrt{\frac{2\pi}{\sigma_\omega^2}} e^{-\frac{(\omega-\omega_0)^2}{2\sigma_\omega^2}}$, the resolution is given by $\Delta l_{FWHM} = \frac{2\ln 2}{\pi}\frac{{\lambda_0}^2}{\Delta\lambda}$.

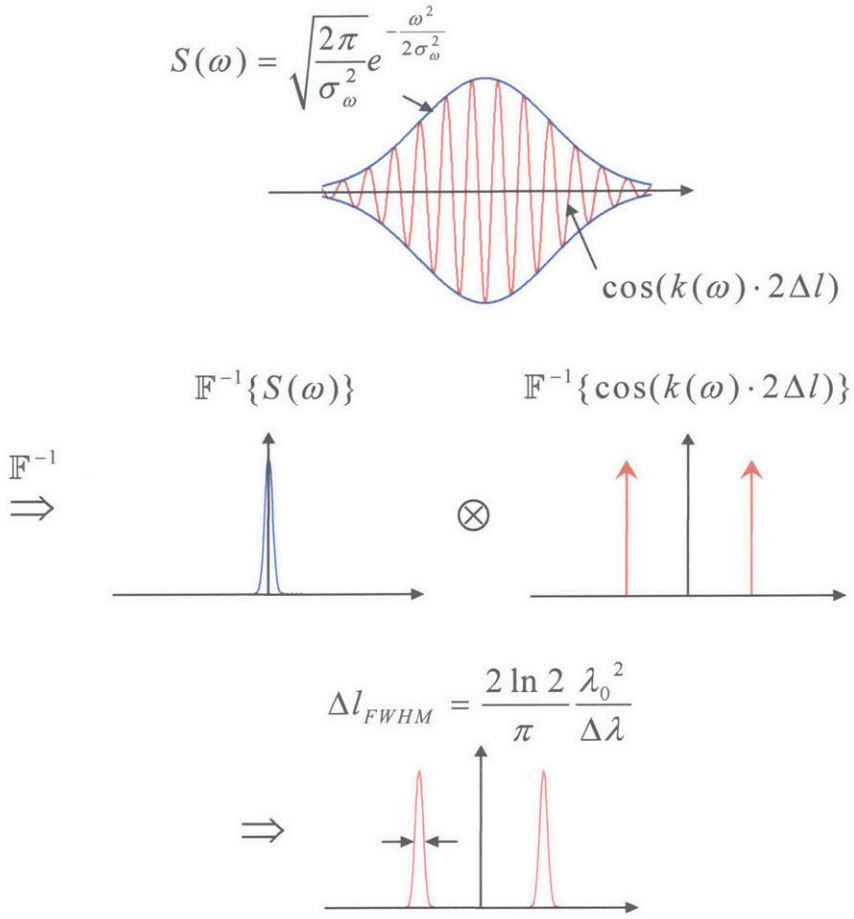

Figure 2.1 Inverse Fourier transformation of I_{int}. The inverse Fourier transform of the Gaussian envelope $S(\omega)$ is the point spread function, and therefore determines the resolution. On the other hand, the cosine term holds information on the path length difference Δl.

2.1.1 Dispersion Compensation

Dispersion causes different optical frequencies to propagate with nonlinearly related velocities dependent on the propagation constants for materials. In ultrafast lasers, short pulses will broaden without proper dispersion compensation. In OCT, the interferometric autocorrelation will broaden if there is dispersion mismatch between the reference and sample arm paths. Therefore, to achieve optimal resolution, the dispersion mismatch between the two arms must be compensated.

The propagation constant $k(\omega)$ can be expanded as a Taylor series near the light source center frequency ω_0:

$$k(\omega) = k(\omega_0) + k'(\omega_0)(\omega-\omega_0) + \frac{k''(\omega_0)}{2}(\omega-\omega_0)^2 + \frac{k'''(\omega_0)}{6}(\omega-\omega_0)^3 + \ldots \qquad (2.9)$$

The constant term $k(\omega_0)$ is the propagation constant at center frequency ω_0. In ultrafast optics, this term corresponds to the phase delay of the carrier at ω_0 passing through a material with propagation constant $k(\omega_0)$. The second term, $k'(\omega_0)$, is the inverse group velocity. This term corresponds to the group delay, or the temporal delay of a pulse passing through a medium with a propagation constant varying linearly as a function of frequency.

Higher order terms in the Taylor expansion result in broadening of the point spread function as well as loss of resolution. The third term in function (2.9) describes the group velocity dispersion which is a variation in group velocity with frequency. This is the term that causes pulse broadening in femtosecond optics and broadening of the axial resolution in OCT. The fourth term is referred to as third-order dispersion, which produces asymmetric pulse distortion in femtosecond optics and asymmetric distortion of the point spread function in OCT. Higher order terms may also be present and can have an effect on the point spread function and resolution.

Equation (2.7) can be rewritten as

$$I_{\text{int}} \propto \sum_n S_n(\omega)\cos\left(\frac{2\Delta l_n \cdot \omega}{c} + \Phi_n(\omega, \Delta l_n)\right) \tag{2.10}$$

The phase term $\Phi_n(\omega, \Delta l_n)$ incorporates all non-linear components of the phase in ω, along with any constant (ω independent) phase. As the above equations show, the combination of dispersion and recalibration errors results in two types of phase terms to compensate: a depth dependent (Δl_n dependent) phase error and a depth independent (Δl_n independent) phase error. In most spectral / Fourier OCT imaging applications, the axial range $\Delta l_{\max}$ over which imaging is performed is short, limited by the number of camera pixels. In scattering tissues, the imaging depth is further limited by optical scattering and absorption. Therefore, the variation of dispersion over the axial image range is usually negligible, while the dispersion is predominantly caused by fixed material in front of the axial imaging range. Since the frequency-dependent phase distortion is treated as the same for all depths in one axial scan, the dispersion is not depth dependent, giving $\Phi_n(\omega, \Delta l_n) = \Phi_n(\omega)$.

In spectral / Fourier domain OCT, dispersion compensation can be done numerically by canceling the frequency-dependent nonlinear phase, which arises from the dispersion mismatch between the two arms of the interferometer. Because the interference signal from the spectrometer is a real function, a Hilbert transform can be used to generate the imaginary part of the complex analytic signal $\text{Im}\left\{\hat{I}_{\text{int}}\right\}$. Note that this is not equivalent to acquiring the complex interference signal directly, since the number of

pixels carrying unique information about the axial measurement is only half of the number of pixels in the spectrum if directly Fourier transformed. The real and imaginary parts of the interference signal are used to construct the complex analytic representation of the spectral fringe pattern. The phase of the complex analytic signal is then adjusted by adding a phase correction to compensate for dispersion:

$$\overline{\Phi}(\omega) = -a_2(\omega - \omega_0)^2 - a_3(\omega - \omega_0)^3 \tag{2.11}$$

The coefficient a_2 is adjusted to cancel the group velocity dispersion imbalance (second-order term in equation 2.9) and a_3 is adjusted to cancel the third-order dispersion imbalance (third-order term in equation 2.9). This method may be applied to higher orders; however, compensation to third-order is usually sufficient, assuming that the interferometer arms were approximately dispersion matched initially. Finally, the corrected spectrum is Fourier transformed to obtain the axial scan. If the appropriate phase correction has been applied, this new axial scan is compensated for dispersion mismatch between the interferometer arms and has optimum axial resolution.[2]

2.1.2 Doppler OCT

Doppler OCT provides information on flow as well as wavelength scale thickness variations and displacements in samples and tissues in the axial direction. Doppler flow is measured by acquiring multiple axial scans at or near the same transverse position and extracting and comparing the relative interferometric phases of sequential scans. Assuming that a reflective layer has distance mismatch Δl_n and velocity v, equation (2.7) can be rewritten using $\Delta l_n + v\tau$, where τ is the time period between measurements and $v\tau << \Delta l_n$:

$$\Delta\phi_n = \frac{2(\Delta l_n + v\tau)\cdot\omega}{c} + \Phi_n(\Delta l_n) = \frac{2\Delta l_n \cdot \omega}{c} + \frac{4\pi v\tau}{\lambda} + \Phi_n(\Delta l_n) = \frac{2\Delta l_n \cdot \omega}{c} + \psi_n(v) + \Phi_n(\Delta l_n) \tag{2.12}$$

The distance mismatch between the reference and sample arm at the same position sequential in time can be written as:

$$\mathrm{I} = \mathbb{F}^{-1}\left\{I_{\mathrm{int}}(\omega)\right\} \propto \sum_n e^{-i\Phi_n(\Delta l_n) - \psi_n(v)} G_n(z) \otimes \delta(z \pm 2\Delta l_n) \tag{2.13}$$

Notice the additional phase term $\psi_n(v)$ compared with equation (2.8).

In spectral / Fourier domain OCT, the phase of the interferometric signal is directly accessible after Fourier transform. The phase data can be used to provide quantitative sub-wavelength measurements of optical path variations within a sample, and to obtain highly sensitive Doppler flow

information. Flow velocity in the direction parallel to the axial OCT probe beam can be measured and is calculated by

$$v(z) = \frac{\Delta\Phi(z)\lambda}{4\pi\tau} \tag{2.14}$$

where $\Delta\Phi(z)$ is the phase difference between the same transverse position of adjacent scans, λ is the center wavelength, and τ is the time difference between adjacent scans.[3, 4]

2.2 Clinical Ultrahigh Speed, Ultrahigh Resolution Spectral / Fourier Domain OCT System

Standard clinical spectral / Fourier domain OCT (SD-OCT) systems operate at 5-7 μm resolution and 25,000-50,000 axial scans per second. Advances in high speed CMOS camera technology has enabled ultrahigh speed SD-OCT imaging with imaging speeds up to 312,000 axial scans per second.[5] In a collaborative effort with Dr. Benjamin Potsaid, Dr. Bernhard Baumann, and WooJhon Choi, we engineered and developed a clinical prototype ultrahigh speed, ultrahigh resolution SD-OCT instrument and began studies at NEEC in 2009. The system has gone through two iterations, and currently operates at an imaging speed of 91,000 axial scans per second. The system uses a high performance compact broadband superluminescent diode light source, avoiding the need for femtosecond lasers and achieving an axial resolution of ~3 μm, which is ~2 times finer than standard commercial SD-OCT instruments.

2.1.1 Spectral / Fourier domain OCT Image Processing Algorithm

In order to improve image processing speed for ultrahigh speed Fourier domain OCT datasets, the image processing algorithms for the clinical prototype system were optimized. This work was done in collaboration with WooJhon Choi and Martin Kraus. Prior to the ultrahigh speed, ultrahigh resolution spectral / Fourier domain OCT system deployment, imaging processing performed in LabVIEW and MATLAB were usually completed in a reasonable amount of time. However, the increased data rates of the new high speed CMOS camera translates to more than 5 times more data flow within the same amount of imaging time compared to the previous generation high speed CCD cameras.

To take advantage of the faster processing speeds in the C++ environment, dlls were created and called under a LabVIEW graphical user interface. First of all, the Fastest Fourier Transform in the West (FFTW) software library for computing discrete Fourier transforms was used to perform high speed Fourier transforms. In addition, a cubic b-spline was used for improved computational cost.[6] Finally, the OpenMP application programming interface in C++ was used to perform multithreading programming. This allows adding parallelism into C++ code without significantly writing. Figure 2.2 shows the Fourier domain OCT image processing flow chart implemented in the processing software.

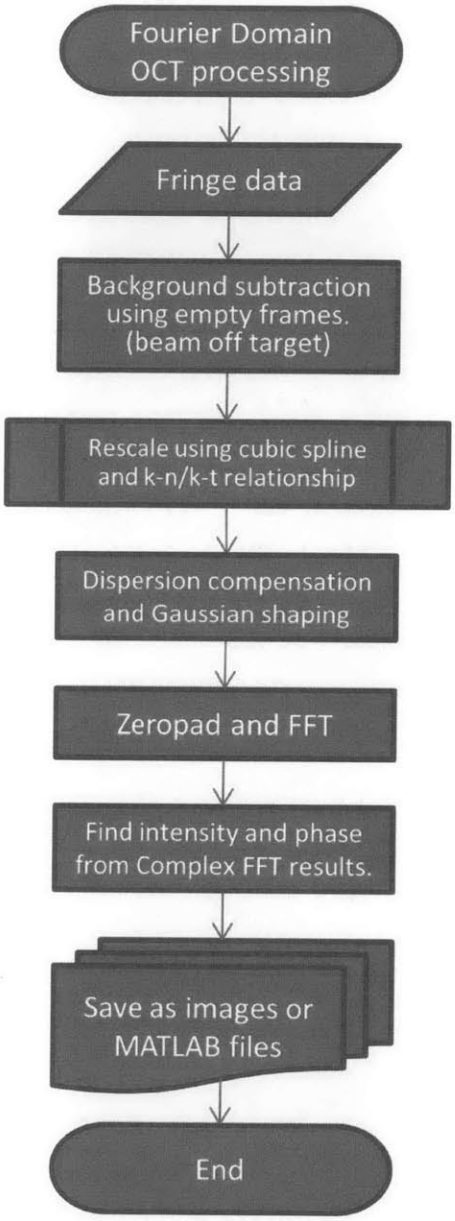

Figure 2.2 Fourier domain OCT image processing flow chart.

2.1.2 Graphical User Interface for Data Acquisition

Ophthalmic OCT acquisition software requires high frame rates for real time preview, which is essential to providing feedback during alignment. With the improved processing speed of OCT data, real-time preview of cross-sectional images in selected positions is possible. However, several other problems remain. For one, a real-time en face OCT fundus preview remains difficult since it requires processing a volumetric OCT dataset with large amount of data compared to a few cross-sectional images. Another problem is the software / hardware interface where the standard National Instrument LabVIEW functions do not fully support lower level function controls.

OCT fundus images require a large number of axial scans for relatively low pixel density preview. For example, a 100 × 100 OCT en face preview requires processing 10,000 axial scans. To perform real-time OCT fundus previews, Parseval's theorem is applied to avoid using Fourier transform:

$$\sum_{\omega=0}^{N-1}\left|I[\omega]\right|^2 = N\sum_{z=0}^{N-1}\left|I[z]\right|^2 \tag{2.15}$$

A squared or absolute sum of the individual pixel values provides sufficient contrast for an OCT fundus preview.

To access low level function controls for the National Instruments frame grabber, a C++ dll was created using the NI-IMAQ C++ library. This allows full control over memory buffers and prevents significant time delay between accessing different memory buffers during acquisition. Separate buffers of different sizes were assigned to the cross-sectional preview frames, OCT fundus preview, and acquired datasets. The acquired datasets are saved directly in the C++ dll without being accessed in LabVIEW.

Figure 2.3 shows the LabVIEW graphical user interface for the ultrahigh speed, ultrahigh resolution spectral / Fourier domain OCT system. Two cross-sectional previews scanning the central temporal-nasal and inferior-superior cross sections are updated in real time. An OCT fundus preview is available with a switch to turn it on. A single spectrometer readout is also extracted for real-time monitoring of system status. The fixation target position can be controlled for imaging different locations in the retina such as macular and optic nerve head regions. Pre-programmed scan patterns as well as custom scan patterns can be chosen from the scan pattern library where scan pattern geometry, density, and range are all adjustable.

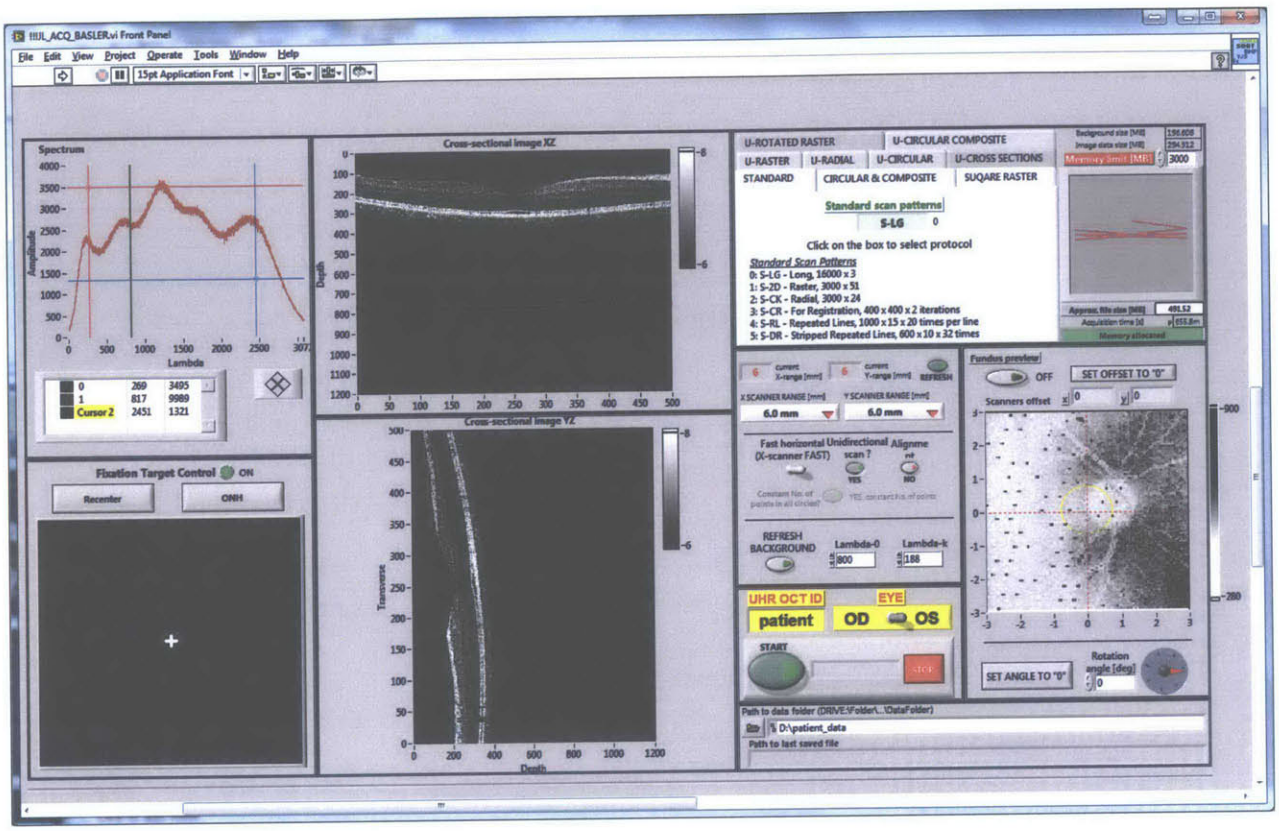

Figure 2.3 GUI for clinical ultrahigh speed, ultrahigh resolution spectral / Fourier domain OCT system. Real-time cross sectional previews, OCT fundus preview, and spectrometer read-out indicate system status and guide patient interface sample arm alignment. Other controls include pre-programmed scan pattern libraries, custom scan pattern inputs, and a fixation target control.

2.3 Small Animal Ultrahigh Speed, Ultrahigh Resolution Spectral / Fourier Domain OCT System

Since the murine retina is structurally similar to the human retina, rat and mouse models provide powerful tools for characterization of ocular disease pathogenesis and response to treatment. Hence, non-invasive imaging technologies for measuring rat and mouse retinal structure and physiology at the micron scale are useful tools for biomedical research on ocular disease. Spectral / Fourier domain OCT enables ultrahigh speed and ultrahigh resolution three-dimensional imaging[7-9], offering a promising technique for rat and mouse retinal imaging[10].

An ultrahigh resolution spectral / Fourier domain OCT prototype instrument was developed for small animal imaging[11] using new, high speed CMOS imaging technology[5]. High speed CMOS technology can achieve imaging speeds over 70,000 axial scans per second. Figure 2.4 shows the schematic of the spectral / Fourier domain OCT system for small animal imaging. To achieve ultrahigh-resolutions, a multiplexed two-superluminescent-diode light source (Superlum) with 145 nm bandwidth

and 890 nm center wavelength was used. A microscope delivery system was designed for focusing and scanning the OCT beam in the animal eye. The power at the rat eye was 1.3 mW. The maximum measured sensitivity was ~94 dB. Three-dimensional OCT (3D-OCT) datasets of the rat retina were acquired using this system. OCT fundus images were created from 3D-OCT data. Doppler OCT analysis [3, 12, 13] of blood flow in the rat retina was performed. The maximum measurable velocity before phase wrapping was 12 mm/s. These studies were in compliance with the guidelines of the ARVO Statement for the Use of Animals in Ophthalmic and Vision Research, and performed under a protocol approved by the MIT Committee on Animal Care.

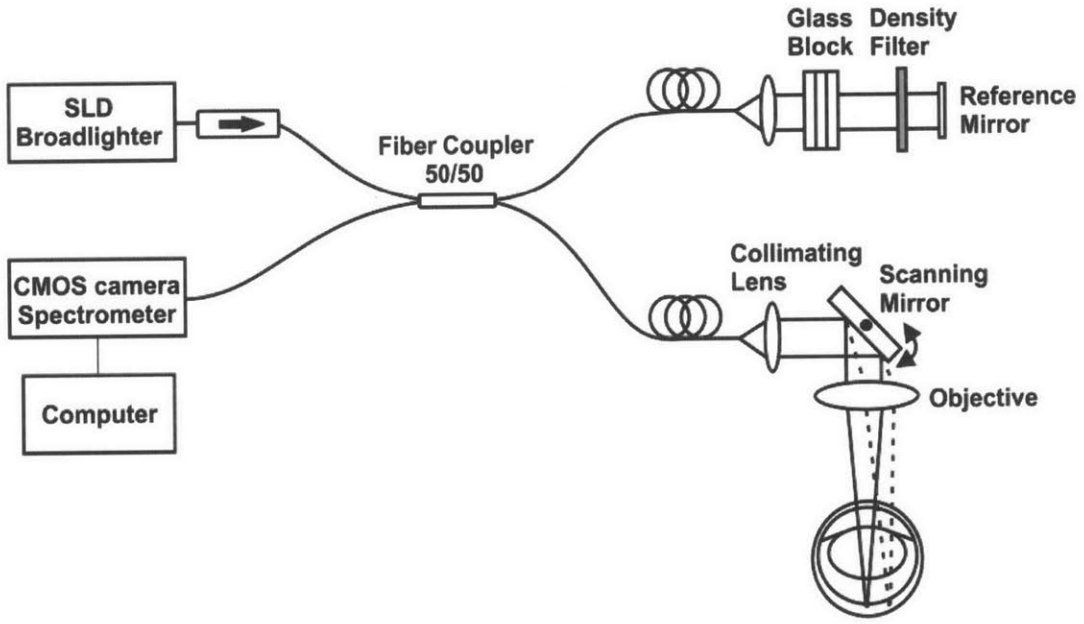

Figure 2.4 Schematic of ultrahigh speed ultrahigh resolution OCT system with a pre-objective scanning microscope design for small animal retina imaging. Spectral / Fourier domain detection is performed with a spectrometer and high speed CMOS camera.

Spectral / Fourier domain OCT imaging of the rat retina was performed at 70,000 axial scans per second with ~3 μm resolution. A standard 3D-OCT dataset containing 180 images, each consisting of 512 axial scans, was acquired in ~1.4 seconds. As shown in Figure 2.5, minimal motion artifacts are visible and the OCT fundus images offer precise registration of individual OCT images to retinal fundus features. Projection OCT fundus images[14] in Figure 2.6 show en face features of the retina distinctively in the nerve fiber layer, retinal capillary networks, and choroidal vasculature. In Figure 2.7, Doppler OCT images and quantitative measurements show pulsatility in blood velocity in a repeatedly scanned retinal vessel cross section.

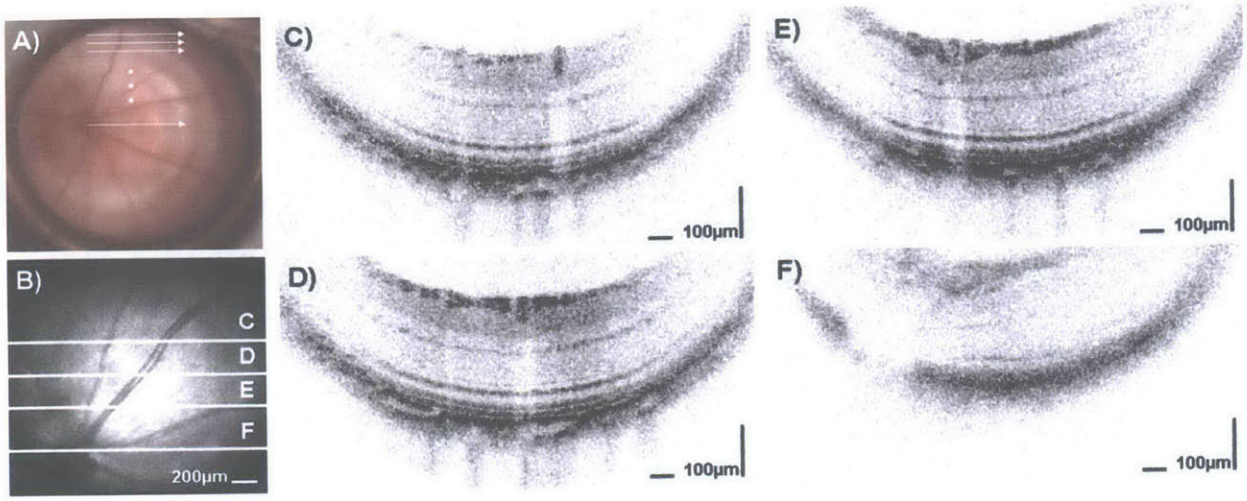

Figure 2.5 A) Raster scan pattern shown on rat fundus photo. 3D-OCT data consisting of 512 axial scans per frame × 180 frames covering 2 mm × 2 mm area was acquired in ~1.4 seconds. B) Standard OCT fundus images are created by summing the signal in the axial direction, yielding an image similar to a fundus photograph. C-F) High definition OCT images with 2048 axial scans, each acquired in 29 µs, can be registered to the OCT fundus image.[11]

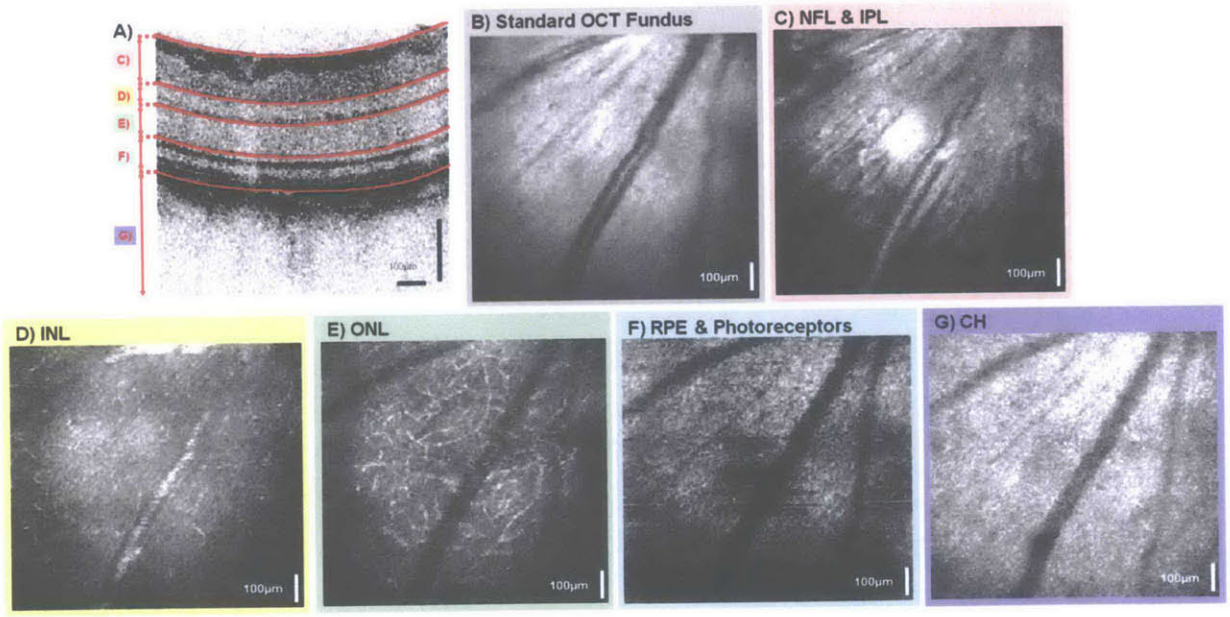

Figure 2.6. OCT en face visualizations created by summing layers sectioned at different depths in the axial direction, providing images of selected layers of the retina. This dataset consists of 300 axial scans per frame × 300 frames covering 1 mm × 1 mm area was acquired in ~1.3 seconds.[11]

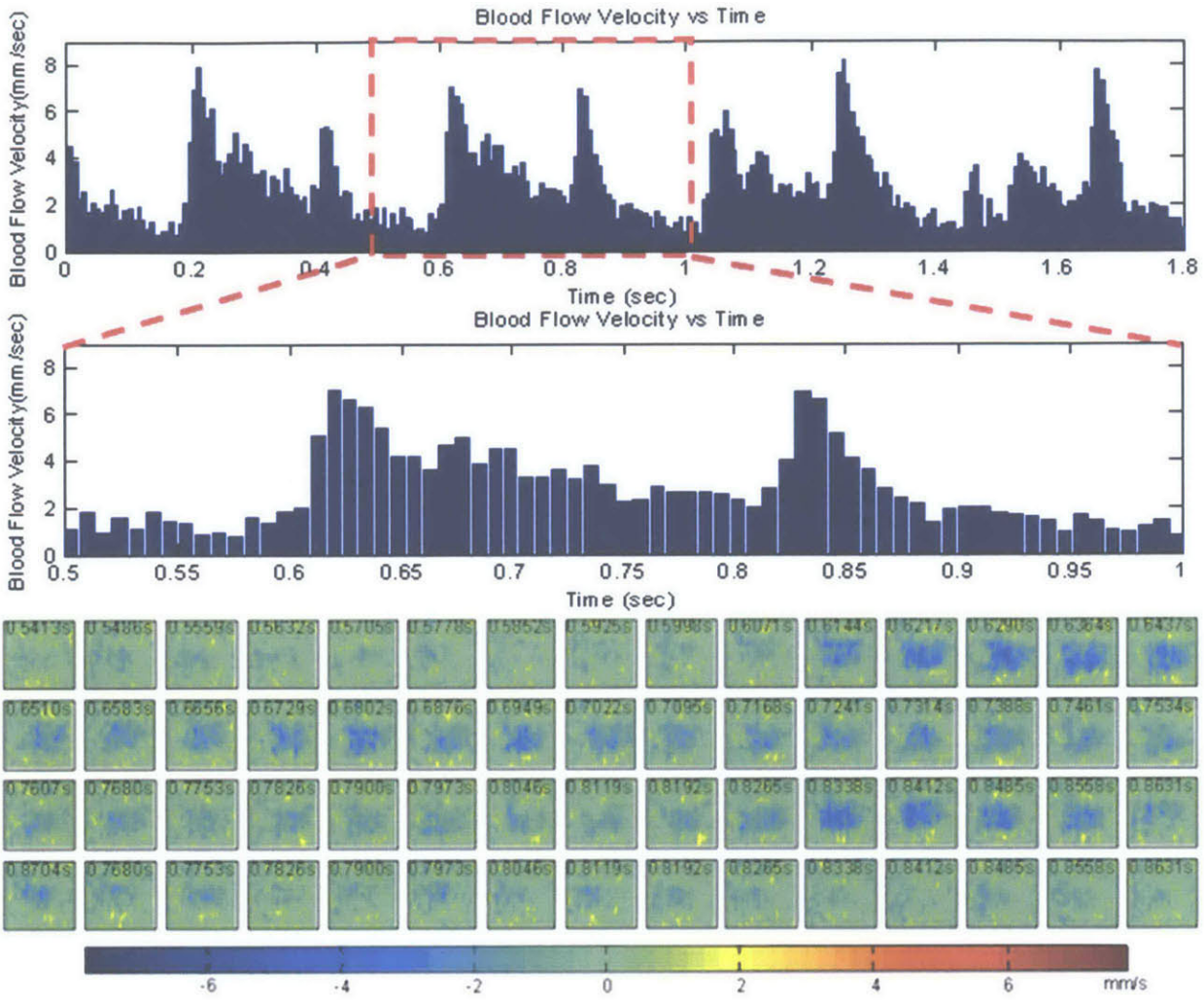

Figure 2.7 Quantitative Doppler OCT measurement in the axial direction showing pulsatile blood flow. Pulsatile blood flow showing a heart rate of ~300 beats per minute. (Top) Doppler OCT images over a 65 μm × 100 μm region of interest and blood flow measurements showing pulsatility during two cardiac cycles. (Middle and bottom) Repeated Doppler OCT scans with 512 axial scans over a 250 μm cross section were continuously acquired for ~1.8 seconds.[11]

In summary, 3D-OCT datasets obtained in the rodent eye using the ultrahigh speed, ultrahigh resolution spectral / Fourier domain OCT system showed reduced motion artifacts, enabling improved en face OCT imaging. Doppler OCT provides non-invasive in vivo quantitative measurements of retinal blood velocity and may benefit studies of diseases such as glaucoma and diabetic retinopathy. Ultrahigh speed, ultrahigh resolution spectral / Fourier domain OCT promises to enable novel protocols for measuring small animal retinal structure and retinal blood flow. Furthermore, non-invasive OCT imaging technology is a promising tool for monitoring disease progression in rat and mouse models to characterize ocular disease pathogenesis and response to treatment.

2.4 References

1. Wojtkowski M, Leitgeb R, Kowalczyk A, Bajraszewski T, Fercher AF. In vivo human retinal imaging by Fourier domain optical coherence tomography. J Biomed Opt. 2002;7(3):457-63.

2. Wojtkowski M, Srinivasan VJ, Ko TH, Fujimoto JG, Kowalczyk A, Duker JS. Ultrahigh-resolution, high-speed, Fourier domain optical coherence tomography and methods for dispersion compensation. Optics Express. 2004;12(11):2404-22. PubMed PMID: ISI:000221888500009.

3. Leitgeb RA, Schmetterer L, Drexler W, Fercher AF, Zawadzki RJ, Bajraszewski T. Real-time assessment of retinal blood flow with ultrafast acquisition by color Doppler Fourier domain optical coherence tomography. Optics Express. 2003;11(23):3116-21. PubMed PMID: ISI:000186641100015.

4. Leitgeb RA, Schmetterer L, Hitzenberger CK, Fercher AF, Berisha F, Wojtkowski M, Bajraszewski T. Real-time measurement of in vitro flow by Fourier-domain color Doppler optical coherence tomography. Opt Lett. 2004;29(2):171-3. doi: Doi 10.1364/Ol.29.000171. PubMed PMID: ISI:000187880100011.

5. Potsaid B, Gorczynska I, Srinivasan VJ, Chen YL, Jiang J, Cable A, Fujimoto JG. Ultrahigh speed Spectral/Fourier domain OCT ophthalmic imaging at 70,000 to 312,500 axial scans per second. Optics Express. 2008;16(19):15149-69. PubMed PMID: WOS:000259271900089.

6. Dooley SR, Stewart RW, Durrani TS. Fast on-line B-spline interpolation. Electron Lett. 1999;35(14):1130-1. doi: Doi 10.1049/El:19990825. PubMed PMID: ISI:000082031900008.

7. Cense B, Nassif N, Chen TC, Pierce MC, Yun S, Park BH, Bouma B, Tearney G, de Boer JF. Ultrahigh-resolution high-speed retinal imaging using spectral-domain optical coherence tomography. Optics Express. 2004;12:2435-47.

8. Leitgeb RA, Drexler W, Unterhuber A, Hermann B, Bajraszewski T, Le T, Stingl A, Fercher AF. Ultrahigh resolution Fourier domain optical coherence tomography. Optics Express. 2004;12(10):2156-65. PubMed PMID: ISI:000221423800015.

9. Wojtkowski M, Srinivasan V, Fujimoto JG, Ko T, Schuman JS, Kowalczyk A, Duker JS. Three-dimensional retinal imaging with high-speed ultrahigh-resolution optical coherence tomography. Ophthalmology. 2005;112(10):1734-46. PubMed PMID: 16140383.

10. Srinivasan VJ, Ko TH, Wojtkowski M, Carvalho M, Clermont A, Bursell SE, Song QH, Lem J, Duker JS, Schuman JS, Fujimoto JG. Noninvasive volumetric Imaging and morphometry of the rodent retina with high-speed, ultrahigh-resolution optical coherence tomography. Investigative Ophthalmology & Visual Science. 2006;47(12):5522-8. PubMed PMID: ISI:000242404900053.

11. Liu JJ, Potsaid B, Chen YL, Gorczynska I, Srinivasan VJ, Duker JS, Fujimoto JG. Ultrahigh Speed Imaging of the Rat Retina Using Ultrahigh Resolution Spectral/Fourier Domain OCT. Proc Spie. 2010;7550. doi: Artn 755017 Doi 10.1117/12.842540. PubMed PMID: ISI:000283928200028.

12. White BR, Pierce MC, Nassif N, Cense B, Park BH, Tearney GJ, Bouma BE, Chen TC, de Boer JF. In vivo dynamic human retinal blood flow imaging using ultra-high-speed spectral domain optical Doppler tomography. Optics Express. 2003;11(25):3490-7. PubMed PMID: ISI:000187324900021.

13. Makita S, Hong Y, Yamanari M, Yatagai T, Yasuno Y. Optical coherence angiography. Optics Express. 2006;14(17):7821-40. doi: Doi 10.1364/Oe.14.007821. PubMed PMID: ISI:000240164100039.

14. Gorczynska I, Srinivasan VJ, Vuong LN, Chen RW, Liu JJ, Reichel E, Wojtkowski M, Schuman JS, Duker JS, Fujimoto JG, Manassakorn A, Ishikawa H, Kim JS, Wollstein G, Bilonick RA, Kagemann L, Gabriele ML, Sung KR, Mumcuoglu T, Duker JS, Fujimoto JG, Schuman JS. Projection OCT fundus imaging for visualizing outer retinal pathology in non-exudative age related macular degeneration Comparison of optic disc margin identified by color disc photography and high-speed ultrahigh-resolution optical coherence tomography. The British journal of ophthalmology. 2008;28(1):28. PubMed PMID: 18662918.

CHAPTER 3

Registration Motion Correction for Spectral / Fourier Domain OCT

3.1 Registration Motion-Correction Algorithm

Martin F. Kraus, from Prof. Joachim Hornegger's group at the Friedrich-Alexander-Universität Erlangen-Nürnberg, developed a novel motion-correction algorithm for three-dimensional (3D-OCT) OCT datasets in a collaborative effort with our group at MIT.[1] Multiple 3D-OCT volumes with orthogonal fast scan axis are taken as the input. The input volumes with different temporal sampling patterns have motion artifacts that are complementary while the spatial dimension which is the fast scanning direction remains relatively intact. Motion correction is performed on a per A-scan basis where a global objective function is optimized to find the displacement fields for each input volume. Non-linear multi-resolution techniques are used to optimize the objective function. After the optimization, the input volumes are transformed to the motion-corrected common space and merged to create a single higher quality motion-corrected volume.

Figure 3.1 is an illustrated example of the motion-correction algorithm applied to two orthogonally scanned 3D-OCT volumes. In the registration motion correction model, two input volumes, $I_x(x,y,z)$ and $I_y(x,y,z)$, where I_x denotes the volume with fast scanning in the x direction and I_y the volume with fast scanning in the y direction, are to be motion corrected and registered. Both input volumes have the same dimensions in x, y, and z, denoted w, h and d respectively. In addition, the model assumes that the intensities of the volumes can be interpolated and are defined in between voxel grid positions. In the model, two displacement fields $\mathbf{d}_X(i,j) = \{\delta x_x(x_i,y_j), \delta y_x(x_i,y_j), \delta z_x(x_i,y_j)\}$ and $\mathbf{d}_Y(i,j) = \{\delta x_Y(x_i,y_j), \delta y_Y(x_i,y_j), \delta z_Y(x_i,y_j)\}$ are to be estimated that associate a 3D displacement vector with each A-scan grid position (x_i, y_j) of each input volume where $1 \le i \le w$ and $1 \le j \le h$ denote the index in the grid in each dimension. The displacement fields are estimated by minimizing a non-linear objective function parameterized on the displacement fields. The objective function consists of two parts, a similarity term and a regularizer. The similarity term is based on computing a per voxel residual as

$$R_{i,j,k} = I_X(x_i + \delta x_X(x_i,y_j), y_j + \delta y_X(x_i,y_j), z_k + \delta z_X(x_i,y_j)) - I_Y(x_i + \delta x_Y(x_i,y_j), y_j + \delta y_Y(x_i,y_j), z_k + \delta z_Y(x_i,y_j)) \quad (3.1)$$

where i and j are defined as before and $1 \leq k \leq d$ marks an index into the volume grid in axial dimension. The baseline similarity measure is computed by evaluating the residual at every grid point and applying a square loss function $L_2^2(x) = x^2$ and summation

$$S_{base} = \sum_{i=1}^{w} \sum_{j=1}^{h} \sum_{k=1}^{d} L_2^2(R_{i,j,k}). \tag{3.2}$$

The regularization term is used to penalize the change in displacement between consecutive A-scans in time and can be expressed as

$$\text{Reg}_{base} = \sum_{t} L_2^2\left(\frac{d\mathbf{d}_X(t)}{dt}\right) + \sum_{t} L_2^2\left(\frac{d\mathbf{d}_Y(t)}{dt}\right) \tag{3.3}$$

where the displacements are treated as functions in time, which corresponds to when the associated A-scan was recorded in the input volume. The two terms are combined in a weighted way using a factor α such that

$$F = S_{base} + \alpha R_{base} \tag{3.4}$$

which is minimized using a multi resolution approach.

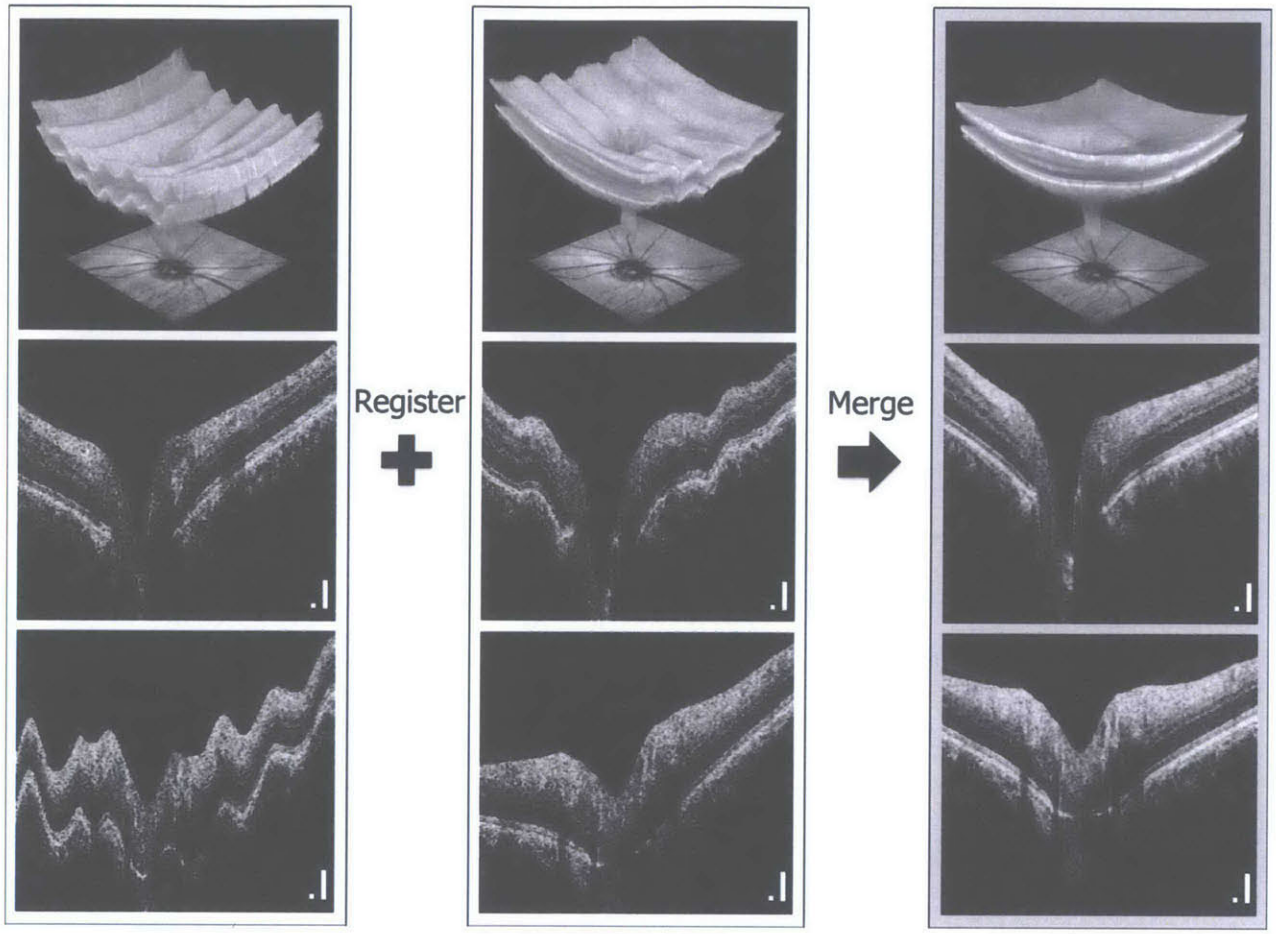

Figure 3.1 3D-OCT motion correction via registration. Two orthogonally scanned 3D-OCT volumes can be registered and merged into a single motion-corrected dataset with improved signal. The central cross section in each volume is displayed with the motion corrected in the single merged dataset. First row: three-dimensional OCT data with motion artifacts in the slow scanning dimension. Second row: temporal-nasal cross-sectional image with no visible motion artifacts in the fast scanning cross section (left) and motion artifacts in the slow scanning cross section (center). Motion artifacts are corrected and signal is improved in cross section from the registered and merged dataset (right). Third row: superior-inferior cross-sectional images with motion artifacts in the slow scanning cross section (left) and without visible motion in the fast scanning cross section (center). After motion correction, no remaining motion artifacts are visible in the cross section from the registered and merged dataset with improved signal. Scale bar: 100 μm.

3.2 Background

Glaucoma is a progressive neuropathy characterized by ganglion cell death, optic nerve damage, and visual field defects. It is the second leading cause of blindness worldwide.[2] Primary open-angle

glaucoma, the most common form of the disease, results in an insidious loss of vision due to ganglion cell atrophy and loss of retinal nerve fibers. Intraocular pressure (IOP) is the major treatable causal risk factor for the development of glaucomatous damage; lowering IOP serves to impede the progression of retinal degenerative changes.[3-5] However, high inter-individual variability and diurnal variation in IOP have limited the use of this parameter for the detection of disease. Moreover, IOP values do not indicate whether or not damage has occurred, nor to what extent. The diagnosis of glaucoma is a clinical one, and is based on assessment of the structure and function of the optic nerve. The tissue structure has traditionally been judged based on appearance, and function is measured using perimetry. Assessment of the ocular appearance is highly dependent on observer skills, and there is high inter- and intra-observer variation.[6, 7] Visual field testing requires the subjective input of the tested individual and thus is prone to high short and long term fluctuation. In addition, it has been shown that loss of 30-50% of the optic nerve tissue may precede the development of clinically detectable visual field defects and identifiable cupping of the optic disc.[8, 9] Thus, there exists a need for the development of objective techniques to quantify the retinal nerve fiber layer (RNFL) and optic nerve head (ONH).

3.2.1 OCT Retinal Nerve Fiber Layer Thickness Measurements

OCT is unique in its ability to assess the ONH and RNFL. Precise measurement of RNFL thickness is important in evaluating patients with glaucoma, in distinguishing between patients with papilledema and crowded optic nerves, and in evaluating other neurodegenerative diseases. The scanning protocol used in the commercial StratusOCT system to assess RNFL thickness was developed by our group in 1995 and has become a clinical standard.[10, 11] In the first pilot study, circumpapillary OCT scans of 2.25 mm or 3.37 mm diameter were acquired centered around the optic disc. Since nerve fibers emanating from the optic disc will cross the OCT scan contours, this protocol measures changes in RNFL density. RNFL thickness was reported by overall mean, quadrant average (superior, inferior, temporal, nasal), hemifield average (superior, inferior, temporal, nasal), average over clock hour, or each individual axial scan.[12] In a subsequent reproducibility study, circular scans of 2.9, 3.4, and 4.5 mm diameters around the optic nerve head were performed.[11] In the third generation commercial time-domain OCT, the StratusOCT implemented a fast 256 A-scan standard-density and a slow 512 A-scan high-density circular scan both with three consecutive circles. The StratusOCT performed 400 A-scans per second where the standard-density scan circles were acquired simultaneously in 1.92 seconds and the high-density scan circles were attained in three sequential 1.28 second acquisitions.

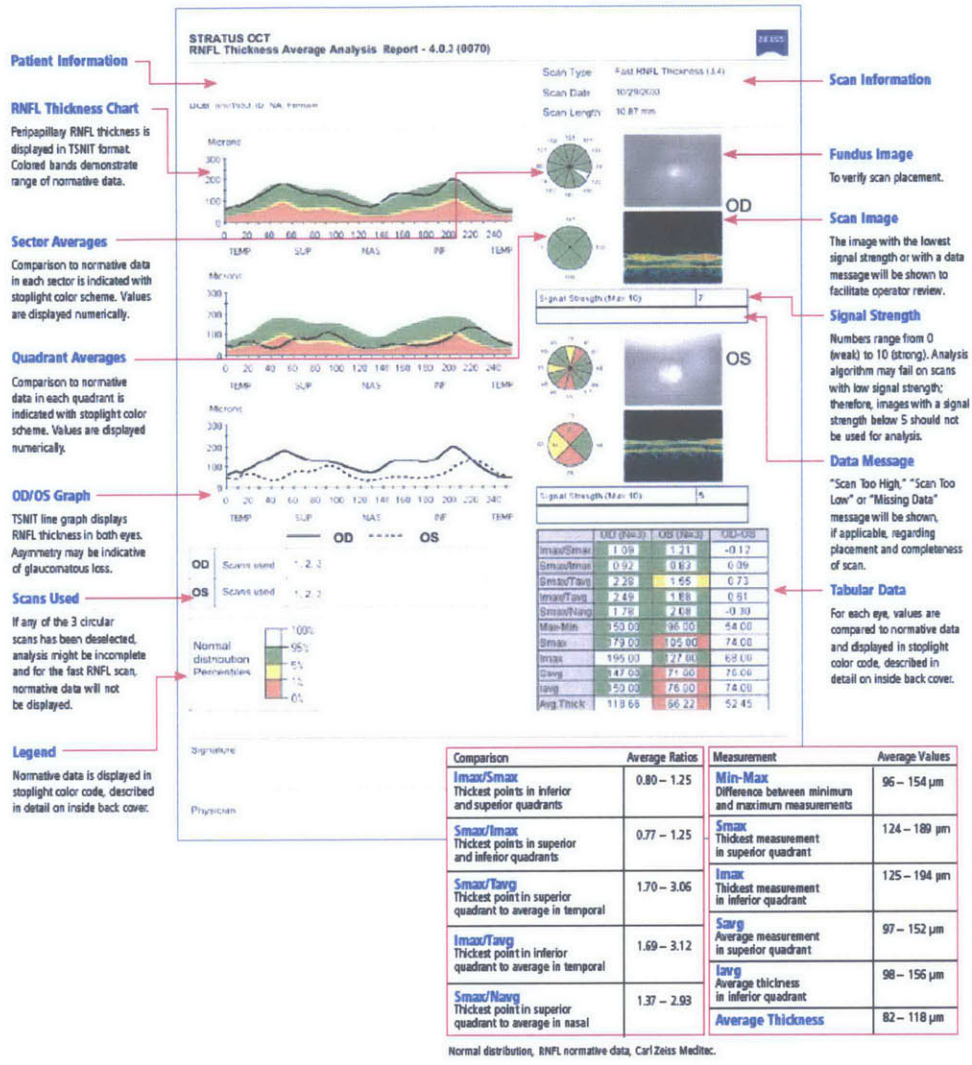

Figure 3.2 OCT RNFL measurements using the time-domain StratusOCT circumpapillary scan around the optic nerve head.[13]

Motion artifacts are one of the biggest problems in obtaining reliable RNFL thickness measurements using OCT. During OCT scanning, the eye continues to move after the operator centers the scan on the optic nerve head. Several studies have demonstrated the improved reproducibility of RNFL thickness measurements from virtual SD-OCT scans compared to TD-OCT.[14-16] However, motion artifacts remain a major source of RNFL thickness measurement variability in SD-OCT scans. In particular, although SD-OCT provides 60 – 100× improved scanning speed compared to TD-OCT, the 3D-OCT datasets still require acquisition times over one second.

3.2.2 Retinal Nerve Fiber Layer Thickness in Normal and Glaucomatous Eyes

Numerous studies have evaluated OCT for distinguishing normal and glaucomatous eyes. The first studies to suggest and demonstrate the utility of OCT for differentiating normal and glaucomatous eyes were performed by our group.[10, 17-20] OCT RNFL measurements were found to be significantly thinner in glaucomatous eyes compared to normal eyes or to ocular hypertensive eyes.[11, 12, 21-24] OCT RNFL measurements had a higher diagnostic accuracy than standard red-free photographic evaluation.[25] OCT RNFL assessment was as good as subjective expert evaluation of optic disc photos.[26, 27] OCT inferior quadrant thickness had a 0.91 area under the receiver operating characteristic (ROC) curve for distinguishing normal and early glaucomatous eyes.[28] In addition to RNFL measures, OCT provides quantitative assessment of the macula and ONH. Measurements obtained for both regions differ significantly between normal and glaucomatous eyes and are useful for glaucoma detection.[29-33] Studies investigated OCT macular mapping and ONH analysis in differentiating between groups and found a significant correlation between macular thickness and global VF indexes.[33] Other studies also showed a significant reduction in macular thickness in glaucoma compared to normal eyes.[34, 35] The area under the ROC curve for discriminating between normal and advanced glaucoma was 0.80.[33] However, a larger area under the ROC curve was found in the same study for circumpapillary RNFL measurements. There was also a significant difference in retinal macular volume between normal and early glaucoma eyes.[32] Cupping of the optic nerve is the parameter traditionally used by clinicians in assessing glaucoma. OCT ONH analysis also provides useful parameters for differentiating between groups with an area under the ROC curve of 0.79.[31] Other studies have shown that peripapillary RNFL thickness had greater diagnostic power than macular thickness and RNFL thickness is still the best surrogate marker in glaucoma assessment.[36-38] Another study showed that RNFL and ONH measurements had better discriminating performance than macular thickness and the combination of ONH and RNFL parameters improved the diagnostic accuracy for glaucoma detection.[39] A further study suggests that the combination of thickness measurements from the 3 innermost retinal layers in the macula, the ganglion cell complex, provides comparable diagnostic power to RNFL thickness measurements.[40]

The recent development of spectral / Fourier Domain OCT (SD-OCT) allows substantially higher sensitivity and faster scanning than time-domain OCT.[41-45] 3D-OCT volumetric datasets can be acquired and RNFL thickness obtained by segmenting the RNFL boundaries in the 3D data.[46-48] This method can be used to identify overall thinning or wedge-shaped focal defects qualitatively and quantitatively. Alternatively, a virtual circular OCT scan image sampled from the 3D-OCT dataset can be used to provide measurements similar to the standard circumpapillary scan implemented in the time-domain OCT systems.[46, 49] Recent studies have shown that RNFL thickness measurement reproducibility from virtual

SD-OCT circular scans is statistically significantly improved over measurements from time-domain OCT circumpapillary scans.[14-16] OCT measurements have been shown to be reproducible and capable of discriminating between health and disease. Each OCT scanning region, RNFL, ONH and macula, was found to provide valuable data for detecting glaucomatous damage and change over time. The combination of information from these three regions can serve as "internal validation" of the finding or as an alternative scanning region in the presence of ocular pathology. With improvements in resolution and speed available through new OCT technology, even more accurate and reproducible quantitative measurements of ocular structure should be possible.

The goal of the study described in this chapter is to compare the reproducibility of SD-OCT RNFL thickness measurements with and without using a registration motion-correction algorithm. In addition, the study aimed to examine whether there was a difference in the reproducibility of RNFL thickness measurements in normal and glaucomatous eyes.

3.3 Methods

In A total of 68 normal and glaucomatous eyes were recruited and imaged between May 2011 and March 2012 at the University of Pittsburgh Medical Center Eye Center (UPMC), Pittsburgh, Pennsylvania, and New England Eye Center (NEEC), Boston, Massachusetts. This study was conducted in collaboration with clinical research teams headed by Dr. Jay Duker, Chairman of Ophthalmology and Director of the New England Eye Center and Dr. Joel Schuman, Chairman of Ophthalmology and Director of UPMC Eye Center and Louis J. Fox Center for Vision Restoration. The study was approved by the institutional review board committees of the Massachusetts Institute of Technology, University of Pittsburgh Medical Center, and Tufts Medical Center. Written informed consent was obtained from all subjects before OCT imaging was performed. Research adhered to the tenets of the Declaration of Helsinki. Raster scan patterns consisting of 200 × 200 axial scans over a 6 mm × 6 mm region over ONH were acquired using commercial Optovue RTVue-100 devices (Optovue Inc., Fremont, CA) with modified software for orthogonal scan patterns and RNFL thickness measurements. Normal and glaucomatous eyes were determined on the basis of standard ophthalmic examination and history. Healthy eyes were characterized as having normal appearance of the ONH and RNFL, full visual fields without any previous history of retinal diseases or glaucoma. Glaucomatous eyes were classified based on clinical examination findings characteristics for glaucoma including optic nerve head rim thinning or local notch, cup asymmetry, disc hemorrhage or RNFL defect accompanied with typical glaucomatous visual field loss. One randomly selected eye was imaged for each subject.

In the first group of subjects, 18 normal (age 48 ± 18 years, range 22 – 74 years) and 30 glaucoma subjects (age 64 ± 10 years, range 33 – 83 years) were scanned at UPMC by an experienced professional photographer. Each subject underwent three repetitions of a series of scans. Three scan protocols which were performed in each series: One 200 × 200 raster scan, a second 200 × 200 raster scan, and a third 200 × 200 orthogonal raster scan. The second raster scan and the third orthogonal raster scan were registered to form a motion-corrected scan using a registration motion-correction algorithm. Each scan protocol was performed until no motion artifacts were visible in the OCT fundus image (no eye motion larger than one vessel diameter or major distortions of the ONH). Failed attempts were acquired and saved. In the second group of subjects, 20 normal subjects (age 34 ± 13 years, range 21 – 64 years) were scanned at NEEC by a medical student research fellow. Three repetitions of the same three scan protocols were performed without considering motion artifacts during acquisition. All scans were performed over a 6 × 6 mm region centered on the ONH. All scans were performed through undilated pupils. All subjects were asked to sit back between scan protocols and the device was re-adjusted.

In the analysis, the "first available" scans are defined as the first available scan without blinking, vignetting, and acquired within the imaging range. The "first available" scans may have eye motion larger than one vessel diameter or major distortions of the ONH visible in the OCT fundus image. To be more specific, the "first available" scan mimics the scenario where the operator omits checking for motion in the OCT fundus image. The "minimal motion" scans are defined as the final scan acquired for each protocol where the operator does not find motion larger than one vessel diameter or major distortions of the ONH visible in the OCT fundus image. The "first-available registered" datasets are the registered and merged "first available" scans acquired in the second and the third orthogonally scanned scan protocols. The "minimal-motion registered" datasets are the registered and merged "minimal motion" scans acquired in the second and third orthogonally scanned scan protocols. All RNFL segmentation and virtual 3.45 mm diameter circle scans for RNFL thickness measurements were performed using RTVue software (Figure 3.3). In addition, RNFL analysis of the "first available" and "minimal motion" scans was performed with standard RTVue motion correction, while RNFL analysis of the "first-available registered" and "minimal-motion registered" datasets were performed with the registration motion-correction algorithm.

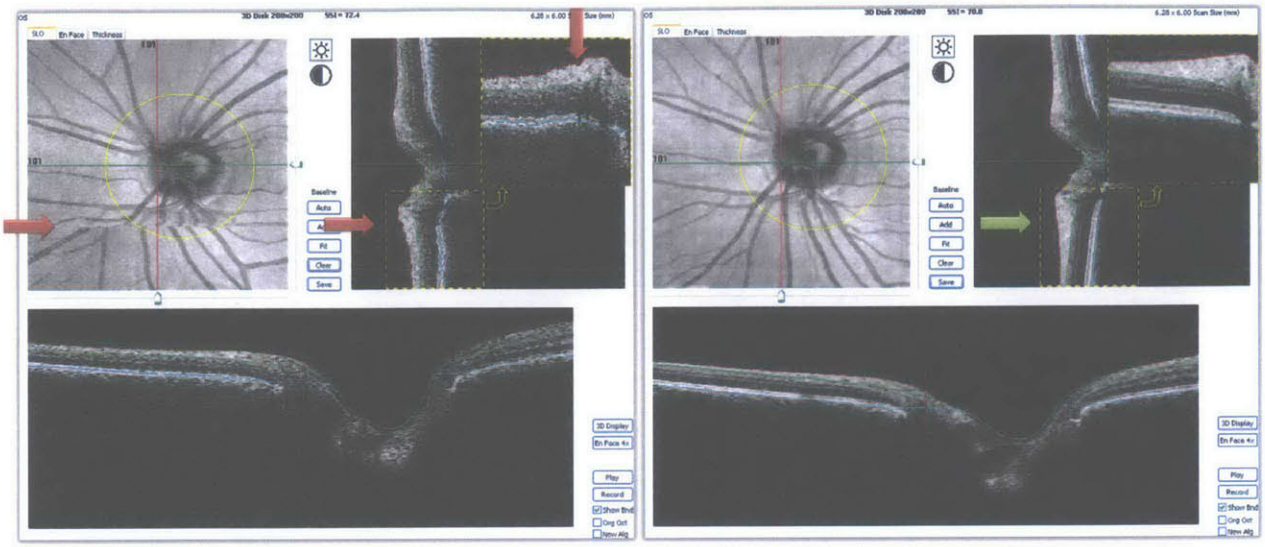

Figure 3.3 RTVue segmentation software. Virtual 3.45 mm diameter circle scans (yellow circles) resampled from a standard raster scan (left) and registered motion-corrected dataset (right) centered on the optic nerve head. Motion artifacts (red arrows) visible in the standard raster scan where the same region in the registered motion-corrected dataset (green arrow) appears free of motion artifacts. Notice the improvement in signal quality and segmentation line continuity when comparing the standard raster scan and registered motion-corrected dataset (orange dashed boxes).

For the first group of subjects, all scans including failed attempts before the final "minimal motion" scan were saved. RNFL thickness measurements using the "first available" scan from the first protocol acquisition, the final "minimal motion" scan from the first protocol acquisition, the "first-available registered" dataset from the second and third protocol acquisition, and the "minimal-motion registered" dataset from the second and third protocol acquisition were compared. For the second group of subjects, only the "first available" scan without blinking, vignetting, and acquired within the imaging range is available for all three scans because motion artifacts in the OCT fundus image were completely ignored during acquisition. More specifically, the scenario of a minimally experienced operator acquiring scans without paying any attention to motion artifacts during acquisition was investigated. RNFL thickness measurements using the "first available" scan from the first protocol acquisition were compared to the "first-available registered" dataset from the second and third protocol acquisition. Statistical analysis was performed using SAS (Statistical Analysis System Institute Inc., Cary, NC) and Excel (Microsoft Corporation, Redmond, WA). Variance components and intraclass correlation coefficients (ICCs) were computed.

3.4 Results

In the first group of subjects, 18 normal and 27 glaucoma subjects were examined. Three glaucoma subjects had to be excluded: two due to failed segmentation caused by low signal (RTVue signal strength index SSI < 35) or mirror artifacts[50], and one due to failed centering of the virtual 3.45 mm diameter circular scan after segmentation. Mean RNFL thickness (± standard deviation) for measurements are summarized in tables 3.1 and 3.2 by diagnostic group and scan dataset ("first available", "minimal motion", "first-available registered", and "minimal-motion registered"). Using all scan datasets, all of the RNFL thickness measurements show statistically significant differences in comparing normal and glaucomatous eyes.

Reproducibility is compared using the variance component ratio and 95% confidence intervals in table 3.3 and table 3.4. When a variance component ratio is equal to one, reproducibilities are identical. There are no differences in reproducibilities when comparing "minimal-motion registered vs minimal motion", "first-available registered vs first available", and "first-available registered vs minimal motion" for normal eyes. In eyes with glaucoma, there are no differences in global RNFL mean. Because the "first-available registered vs first available" 95% confidence intervals do not include one in the temporal, nasal, and inferior quadrants, this indicates that the reproducibilities are statistically significantly different at the 5% level of confidence. Similarly, the "minimal-motion registered vs minimal motion" 2, 4, 5 and 10 clock hours, "first-available registered vs first available" 2-10 clock hours, as well as "first-available registered vs minimal motion" 2, 4, 9, and 10 clock hours show improvement in RNFL thickness measurement variability with statistically significantly smaller reproducibility.

ICCs for each parameter and each scan dataset are shown in table 3.5. Corresponding square root of the variance component for all scans are shown in table 3.6. Square root of the scan variance component over the parameter mean for each method for the measurements are shown in table 3.7. Figure 3.4 shows that the reproducibilities in normal eye RNFL thickness measurements are identical regardless of method. Figure 3.5 shows the reproducibility improvement in several quadrants and clock hours in the registered motion-corrected datasets. The narrow confidence intervals suggest the number of subjects was sufficient to make observations about the differences between reproducibilities.

Table 3.1 Retinal nerve fiber layer thickness: relation to diagnosis. (Standard raster scans)

	First Available			Minimal Motion		
	Normal	Glaucoma		Normal	Glaucoma	
	54 measurements	81 measurements		54 measurements	81 measurements	
	18 subjects	27 subjects		18 subjects	27 subjects	
Parameter	Mean (Standard Deviation)		P Value	Mean (Standard Deviation)		P Value
Global Mean	93.3 (7.6)	70.6 (13.8)	<0.0001	93.3 (7.7)	70.7 (14.1)	<0.0001
Quadrants						
Temporal	70.1 (10.6)	54.7 (13.2)	<0.0001	70.0 (11.0)	54.5 (13.2)	<0.0001
Superior	108.7 (16.5)	81.5 (22.1)	<0.0001	108.6 (16.3)	82.0 (23.1)	<0.0001
Nasal	71.7 (9.8)	60.3 (12.5)	<0.0001	72.1 (9.6)	60.0 (12.7)	<0.0001
Inferior	122.7 (13.9)	86.0 (21.7)	<0.0001	122.6 (14.2)	86.3 (20.9)	<0.0001
Clock Hour						
1	99.4 (18.1)	77.8 (24.7)	<0.0001	99.2 (17.7)	78.3 (25.1)	<0.0001
2	87.4 (14.8)	66.0 (16.3)	<0.0001	87.6 (14.3)	65.8 (16.5)	<0.0001
3	58.3 (8.6)	53.8 (11.0)	0.0123	58.5 (8.7)	53.5 (11.2)	0.0068
4	68.9 (10.0)	61.0 (15.1)	0.001	69.5 (10.0)	60.4 (15.0)	0.0001
5	110.1 (21.7)	81.1 (20.6)	<0.0001	110.9 (22.6)	80.5 (20.4)	<0.0001
6	139.4 (24.8)	97.6 (29.4)	<0.0001	139.2 (25.3)	98.0 (28.4)	<0.0001
7	119.3 (22.5)	79.8 (26.7)	<0.0001	118.3 (22.5)	80.8 (26.3)	<0.0001
8	67.0 (19.1)	51.4 (13.1)	<0.0001	66.7 (20.4)	51.4 (13.4)	<0.0001
9	58.6 (7.2)	49.1 (12.3)	<0.0001	58.6 (6.9)	49.1 (12.5)	<0.0001
10	84.1 (11.5)	63.5 (18.7)	<0.0001	84.2 (11.8)	62.8 (18.3)	<0.0001
11	121.9 (17.1)	82.2 (25.7)	<0.0001	122.0 (17.5)	82.0 (25.4)	<0.0001
12	104.8 (23.8)	84.5 (25.8)	<0.0001	104.7 (23.7)	85.8 (27.7)	<0.0001

Table 3.2 Retinal nerve fiber layer thickness: relation to diagnosis. (Registered motion-corrected datasets)

	First-available Registered			Minimal-motion Registered		
	Normal	Glaucoma		Normal	Glaucoma	
	54 measurements 18 subjects	81 measurements 27 subjects		54 measurements 18 subjects	81 measurements 27 subjects	
Parameter	Mean (Standard Deviation)		P Value	Mean (Standard Deviation)		P Value
Global Mean	96.1 (8.3)	72.4 (15.5)	<0.0001	96.3 (8.1)	72.2 (15.4)	<0.0001
Quadrants						
Temporal	72.4 (12.2)	55.6 (13.8)	<0.0001	72.7 (12.3)	55.7 (14.1)	<0.0001
Superior	111.1 (17.9)	83.7 (26.0)	<0.0001	111.1 (17.9)	83.5 (25.5)	<0.0001
Nasal	73.8 (10.1)	61.0 (13.9)	<0.0001	73.7 (10.2)	60.6 (13.8)	<0.0001
Inferior	127.2 (15.2)	89.4 (23.0)	<0.0001	128.0 (14.9)	89.0 (23.1)	<0.0001
Clock Hour						
1	99.6 (17.8)	78.7 (28.5)	<0.0001	99.6 (17.4)	78.8 (28.3)	<0.0001
2	89.6 (15.2)	67.8 (18.4)	<0.0001	89.6 (15.3)	67.5 (18.4)	<0.0001
3	60.1 (9.6)	53.4 (11.8)	0.0007	59.9 (9.8)	53.1 (11.8)	0.0006
4	71.1 (10.6)	61.3 (16.0)	0.0001	71.1 (10.6)	61.0 (15.6)	<0.0001
5	113.4 (24.7)	83.6 (21.9)	<0.0001	114.7 (26.1)	83.4 (22.4)	<0.0001
6	144.0 (26.9)	100.9 (31.4)	<0.0001	145.1 (26.8)	100.6 (31.7)	<0.0001
7	125.0 (24.0)	84.2 (28.6)	<0.0001	124.9 (23.5)	83.6 (28.2)	<0.0001
8	69.3 (21.5)	52.6 (14.8)	<0.0001	69.4 (21.6)	52.6 (15.7)	<0.0001
9	59.8 (7.6)	49.2 (12.1)	<0.0001	59.9 (7.5)	49.4 (12.4)	<0.0001
10	87.5 (14.0)	64.8 (19.4)	<0.0001	88.1 (14.2)	64.7 (19.4)	<0.0001
11	128.0 (20.5)	85.6 (27.9)	<0.0001	128.1 (21.0)	85.5 (27.0)	<0.0001
12	105.7 (26.2)	86.8 (31.1)	0.0004	105.5 (25.9)	86.2 (31.0)	0.0002

Table 3.3 Reproducibility (variance components) ratios with 95% confidence intervals among the tested scan datasets. (Normal eyes)

	Minimal-motion Registered vs Minimal Motion			First-available Registered vs First Available			First-available Registered vs Minimal Motion		
Parameter	Lower	Estimated	Upper	Lower	Estimated	Upper	Lower	Estimated	Upper
Global Mean	0.554	1.454	3.815	0.424	1.113	2.920	0.636	1.670	4.382
Quadrants									
Temporal	0.502	1.317	3.455	0.173	0.454	1.190	0.379	0.993	2.606
Superior	0.348	0.914	2.398	0.413	1.082	2.840	0.458	1.202	3.155
Nasal	0.758	1.990	5.221	0.298	0.781	2.049	0.752	1.973	5.177
Inferior	0.347	0.912	2.392	0.368	0.965	2.531	0.496	1.301	3.413
Clock Hour									
1	0.252	0.661	1.734	0.325	0.853	2.238	0.334	0.876	2.299
2	0.298	0.783	2.054	0.201	0.528	1.385	0.324	0.849	2.229
3	0.368	0.966	2.534	0.213	0.560	1.469	0.333	0.874	2.294
4	0.489	1.284	3.369	0.391	1.027	2.693	0.575	1.510	3.961
5	0.441	1.157	3.035	0.251	0.660	1.731	0.383	1.006	2.639
6	0.262	0.687	1.803	0.441	1.156	3.033	0.434	1.140	2.991
7	0.487	1.278	3.354	0.274	0.718	1.884	0.432	1.135	2.977
8	0.687	1.804	4.732	0.191	0.502	1.317	0.340	0.892	2.340
9	0.185	0.484	1.270	0.187	0.492	1.290	0.230	0.604	1.584
10	0.225	0.589	1.546	0.167	0.438	1.148	0.289	0.759	1.991
11	0.290	0.762	1.999	0.297	0.778	2.043	0.312	0.820	2.151
12	0.358	0.939	2.464	0.479	1.257	3.297	0.529	1.388	3.641

Table 3.4 Reproducibility (variance components) ratios with 95% confidence intervals among the tested scan datasets. (Glaucomatous eyes)

	Minimal-motion Registered vs Minimal Motion			First-available Registered vs First Available			First-available Registered vs Minimal Motion		
Parameter	Lower	Estimated	Upper	Lower	Estimated	Upper	Lower	Estimated	Upper
Global Mean	0.342	0.743	1.615	0.357	0.775	1.685	0.378	0.821	1.784
Quadrants									
Temporal	0.229	0.497	1.081	0.079	0.171	0.372	0.131	0.285	0.619
Superior	0.428	0.930	2.022	0.469	1.019	2.213	0.545	1.184	2.573
Nasal	0.253	0.550	1.196	0.090	0.195	0.424	0.276	0.600	1.304
Inferior	0.258	0.561	1.220	0.200	0.435	0.945	0.296	0.643	1.396
Clock Hour									
1	0.337	0.733	1.592	0.289	0.627	1.363	0.549	1.192	2.590
2	0.138	0.299	0.649	0.119	0.258	0.561	0.133	0.288	0.626
3	0.230	0.500	1.087	0.060	0.130	0.283	0.255	0.555	1.205
4	0.161	0.350	0.760	0.099	0.214	0.466	0.199	0.433	0.940
5	0.168	0.366	0.794	0.142	0.309	0.671	0.215	0.467	1.015
6	0.270	0.586	1.274	0.147	0.320	0.695	0.244	0.530	1.153
7	0.341	0.741	1.610	0.180	0.390	0.848	0.427	0.928	2.017
8	0.725	1.575	3.423	0.168	0.366	0.795	0.538	1.169	2.541
9	0.327	0.711	1.544	0.067	0.146	0.317	0.169	0.366	0.796
10	0.060	0.131	0.285	0.176	0.382	0.831	0.087	0.189	0.411
11	0.363	0.790	1.716	0.453	0.985	2.141	0.293	0.636	1.382
12	0.399	0.867	1.885	0.434	0.943	2.049	0.457	0.993	2.158

Table 3.5 Intraclass correlation coefficients. (ICCs)

	ICC							
	Normal				Glaucoma			
Parameter	First Available	Minimal Motion	First-available Registered	Minimal-motion Registered	First Available	Minimal Motion	First-available Registered	Minimal-motion Registered
Global Mean	0.977	0.986	0.980	0.981	0.991	0.992	0.995	0.995
Quadrants								
Temporal	0.981	0.992	0.994	0.992	0.975	0.985	0.996	0.994
Superior	0.965	0.969	0.966	0.970	0.978	0.982	0.983	0.987
Nasal	0.978	0.991	0.984	0.985	0.938	0.981	0.990	0.991
Inferior	0.973	0.980	0.975	0.982	0.988	0.991	0.995	0.996
Clock Hour								
1	0.962	0.962	0.958	0.966	0.957	0.978	0.980	0.988
2	0.963	0.975	0.980	0.982	0.954	0.959	0.991	0.991
3	0.968	0.979	0.986	0.985	0.889	0.976	0.987	0.989
4	0.963	0.975	0.971	0.975	0.902	0.952	0.982	0.984
5	0.989	0.992	0.993	0.994	0.980	0.987	0.994	0.996
6	0.981	0.982	0.978	0.987	0.980	0.987	0.994	0.994
7	0.977	0.986	0.986	0.983	0.979	0.991	0.993	0.994
8	0.983	0.992	0.992	0.987	0.953	0.986	0.987	0.984
9	0.942	0.948	0.974	0.979	0.951	0.982	0.993	0.987
10	0.959	0.978	0.988	0.992	0.982	0.963	0.994	0.996
11	0.951	0.958	0.974	0.973	0.986	0.978	0.988	0.984
12	0.963	0.968	0.964	0.973	0.965	0.971	0.978	0.980

Table 3.6 Square root of scan variance component (which is approximately the average standard deviation).

	Square root of scan variance component ("SD", μm)							
	Normal				Glaucoma			
Parameter	First Available	Minimal Motion	First-available Registered	Minimal-motion Registered	First Available	Minimal Motion	First-available Registered	Minimal-motion Registered
Global Mean	1.38	1.12	1.45	1.35	1.57	1.53	1.39	1.32
Quadrants								
Temporal	1.81	1.22	1.22	1.40	2.59	2.01	1.07	1.42
Superior	3.66	3.47	3.80	3.32	4.11	3.81	4.15	3.68
Nasal	1.79	1.13	1.59	1.59	3.89	2.21	1.72	1.64
Inferior	2.94	2.53	2.88	2.41	3.00	2.47	1.98	1.85
Clock Hour								
1	4.33	4.28	4.00	3.48	6.30	4.57	4.99	3.91
2	3.50	2.76	2.54	2.44	4.31	4.08	2.19	2.23
3	1.94	1.55	1.45	1.53	4.49	2.18	1.62	1.54
4	2.16	1.78	2.19	2.02	5.71	4.01	2.64	2.37
5	2.93	2.37	2.38	2.55	3.57	2.90	1.98	1.76
6	4.32	4.35	4.65	3.61	5.15	4.00	2.91	3.06
7	4.28	3.41	3.63	3.85	4.78	3.10	2.98	2.66
8	3.04	2.28	2.15	3.06	3.52	1.97	2.13	2.47
9	2.19	1.97	1.53	1.37	3.21	2.02	1.23	1.71
10	2.83	2.15	1.87	1.65	3.03	4.31	1.87	1.56
11	4.60	4.49	4.06	3.92	3.77	4.69	3.74	4.17
12	5.32	5.06	5.96	4.90	5.95	5.80	5.78	5.40

Table 3.7 Square root of the scan variance component over the parameter mean.

	Square root of scan variance component/parameter mean							
	Normal				Glaucoma			
Parameter	First Available	Minimal Motion	First-available Registered	Minimal-motion Registered	First Available	Minimal Motion	First-available Registered	Minimal-motion Registered
Global Mean	1.5%	1.2%	1.5%	1.4%	2.2%	2.2%	1.9%	1.8%
Quadrants								
Temporal	2.6%	1.7%	1.7%	1.9%	4.7%	3.7%	1.9%	2.5%
Superior	3.4%	3.2%	3.4%	3.0%	5.0%	4.6%	5.0%	4.4%
Nasal	2.5%	1.6%	2.1%	2.2%	6.4%	3.7%	2.8%	2.7%
Inferior	2.4%	2.1%	2.3%	1.9%	3.5%	2.9%	2.2%	2.1%
Clock Hour								
1	4.4%	4.3%	4.0%	3.5%	8.1%	5.8%	6.3%	5.0%
2	4.0%	3.1%	2.8%	2.7%	6.5%	6.2%	3.2%	3.3%
3	3.3%	2.7%	2.4%	2.5%	8.4%	4.1%	3.0%	2.9%
4	3.1%	2.6%	3.1%	2.8%	9.4%	6.7%	4.3%	3.9%
5	2.7%	2.1%	2.1%	2.2%	4.4%	3.6%	2.4%	2.1%
6	3.1%	3.1%	3.2%	2.5%	5.3%	4.1%	2.9%	3.0%
7	3.6%	2.9%	2.9%	3.1%	6.0%	3.8%	3.5%	3.2%
8	4.5%	3.4%	3.1%	4.4%	6.8%	3.8%	4.0%	4.7%
9	3.7%	3.4%	2.6%	2.3%	6.5%	4.1%	2.5%	3.5%
10	3.4%	2.6%	2.1%	1.9%	4.8%	6.9%	2.9%	2.4%
11	3.8%	3.7%	3.2%	3.1%	4.6%	5.7%	4.4%	4.9%
12	5.1%	4.8%	5.6%	4.6%	7.0%	6.8%	6.7%	6.3%

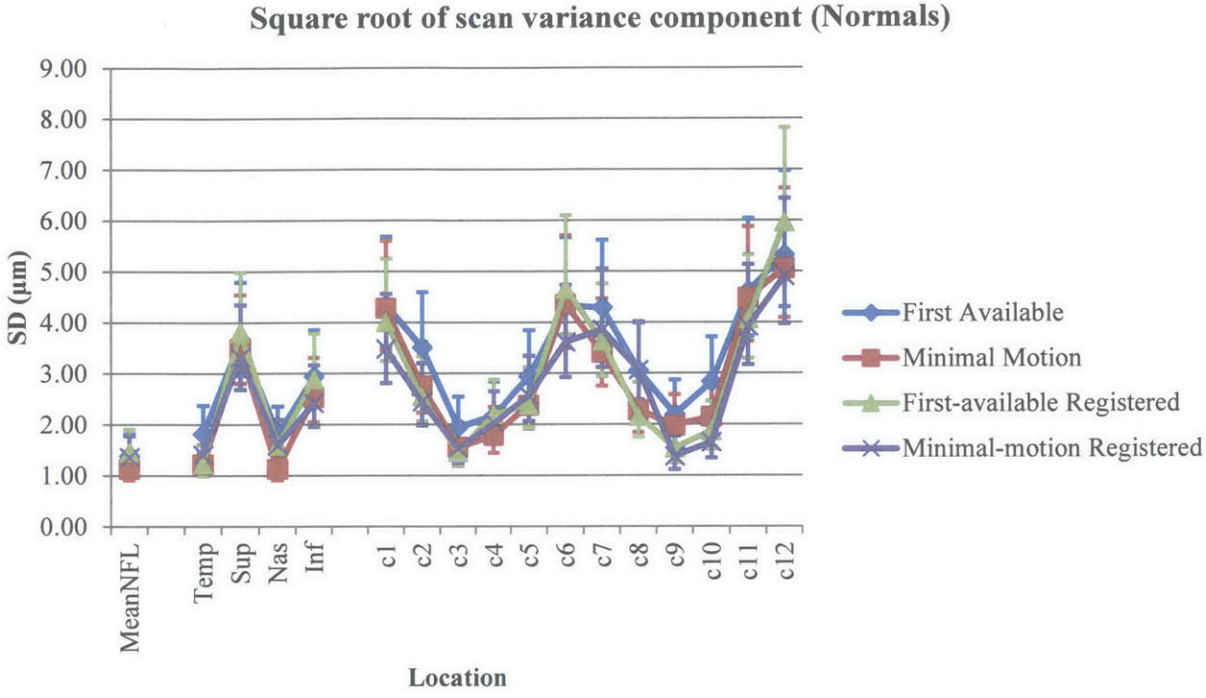

Figure 3.4 Square root of scan variance component ("SD") plot from table 3.6 with 95% confidence intervals. (Normal eyes)

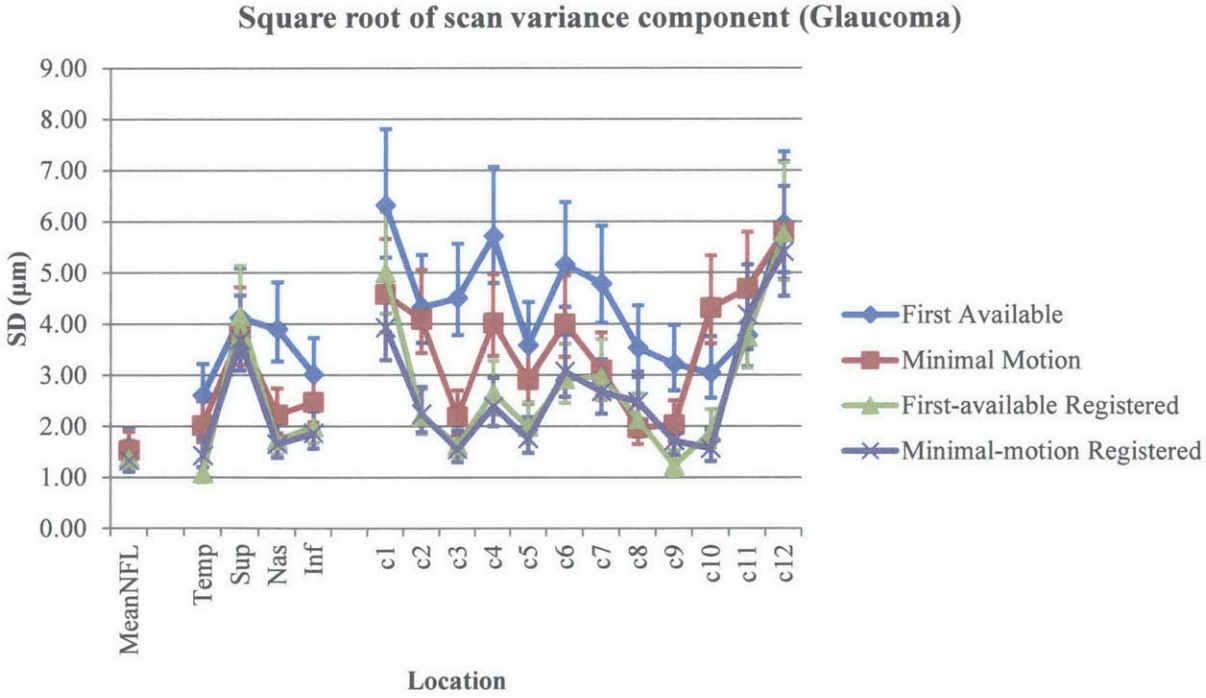

Figure 3.5 Square root of scan variance component ("SD") plot from table 3.6 with 95% confidence intervals. (Glaucomatous eyes)

In the second group of subjects, 19 normal subjects were examined. One subject was excluded due to bad fixation where the ONH was not properly centered. Mean RNFL thickness (± standard deviation) for measurements are summarized in table 3.8. Reproducibility is compared using the variance component ratio and 95% confidence intervals in table 3.9. Statistically significantly smaller reproducibility is observed in the temporal and nasal quadrants, as well as 1, 4, 5, 6, 7, 8, 9, 10, 11 clock hours when comparing "first-available registered vs first available" acquired without considering motion. ICCs along with the corresponding square root of the variance component and square root of variance components over parameter means are shown in table 3.10. Figure 3.6 shows the improved reproducibilities of regional measurements in registered motion-corrected datasets when the operator ignores motion artifacts during acquisition. The narrow confidence intervals again suggest the number of subjects was sufficient to make observations about the differences between reproducibilities.

Table 3.8 Retinal nerve fiber layer thickness. (Motion ignored during acquisition)

	First Available	First-available Registered
	57 measurements 19 subjects	57 measurements 19 subjects
Parameter	Mean (Standard Deviation)	Mean (Standard Deviation)
Global Mean	91.7 (10.9)	94.4 (11.4)
Quadrants		
Temporal	72.5 (11.0)	72.2 (12.7)
Superior	110.2 (18.2)	113.4 (19.2)
Nasal	68.5 (15.5)	72.2 (15.2)
Inferior	115.8 (14.4)	119.8 (14.5)
Clock Hour		
1	98.5 (19.7)	103.1 (19.9)
2	83.2 (22.6)	89.5 (21.7)
3	57.7 (12.6)	59.9 (11.7)
4	64.2 (15.3)	66.9 (15.9)
5	98.4 (21.0)	103.3 (21.3)
6	125.6 (21.2)	129.7 (21.8)
7	123.9 (17.2)	127.1 (21.0)
8	69.9 (13.7)	70.2 (14.1)
9	60.0 (9.5)	59.0 (10.2)
10	87.2 (15.6)	86.8 (19.8)
11	125.8 (20.8)	128.5 (25.5)
12	106.2 (23.7)	108.6 (25.1)

Table 3.9 Reproducibility (variance components) ratios with 95% confidence intervals. (Motion ignored during acquisition)

	First-available Registered vs First Available		
Parameter	Lower	Estimated	Upper
Global Mean	0.596	0.234	1.520
Quadrants			
Temporal	0.096	0.038	0.246
Superior	0.422	0.166	1.078
Nasal	0.290	0.114	0.739
Inferior	0.560	0.219	1.429
Clock Hour			
1	0.224	0.088	0.572
2	0.510	0.200	1.300
3	0.517	0.203	1.320
4	0.114	0.045	0.292
5	0.062	0.024	0.158
6	0.266	0.104	0.678
7	0.351	0.138	0.896
8	0.088	0.034	0.224
9	0.140	0.055	0.358
10	0.187	0.073	0.476
11	0.190	0.074	0.485
12	0.581	0.228	1.483

Table 3.10 Intraclass correlation coefficients (ICCs), square root of scan variance component ("SD") and the square root of scan variance component over the parameter mean. (Motion ignored during acquisition)

	ICC		SD (μm)		SD/Mean	
Parameter	First Available	First-available Registered	First Available	First-available Registered	First Available	First-available Registered
Global Mean	0.991	0.995	1.25	0.97	1.4%	1.0%
Quadrants						
Temporal	0.953	0.997	2.97	0.92	4.1%	1.3%
Superior	0.989	0.995	2.36	1.53	2.1%	1.4%
Nasal	0.974	0.992	3.12	1.68	4.6%	2.3%
Inferior	0.981	0.989	2.38	1.78	2.1%	1.5%
Clock Hour						
1	0.975	0.994	3.81	1.80	3.9%	1.7%
2	0.985	0.992	3.47	2.47	4.2%	2.8%
3	0.967	0.980	2.90	2.09	5.0%	3.5%
4	0.931	0.993	4.96	1.68	7.7%	2.5%
5	0.914	0.995	7.51	1.87	7.6%	1.8%
6	0.980	0.995	3.58	1.84	2.8%	1.4%
7	0.864	0.969	7.74	4.59	6.2%	3.6%
8	0.938	0.995	4.27	1.26	6.1%	1.8%
9	0.946	0.993	2.77	1.04	4.6%	1.8%
10	0.958	0.995	3.98	1.72	4.6%	2.0%
11	0.967	0.996	4.81	2.10	3.8%	1.6%
12	0.986	0.993	3.38	2.58	3.2%	2.4%

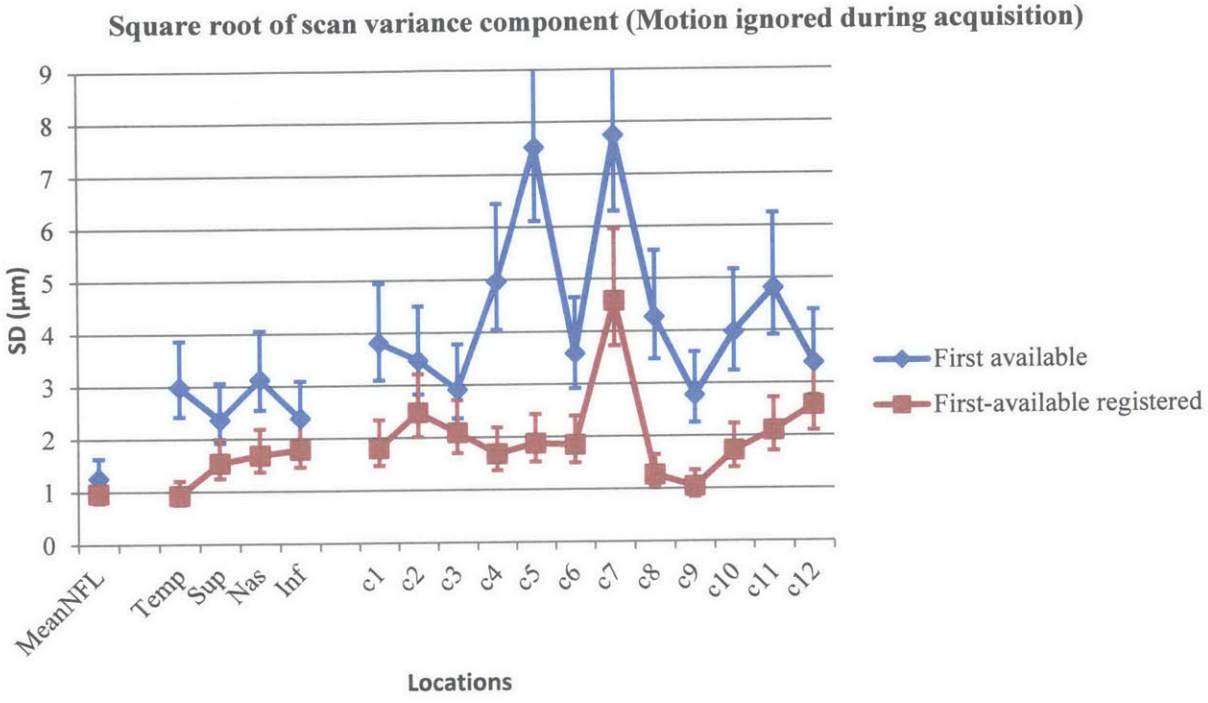

Figure 3.6 Square root of scan variance component ("SD") plot from table 3.10 with 95% confidence intervals. (Motion ignored during acquisition)

3.5 Discussion

For a new method to be accepted for use in clinical practice, an important first step is to evaluate its reproducibility to assess its diagnosis accuracy and describe the smallest changes detectable for monitoring disease progression. Prior studies have investigated RNFL thickness reproducibility using TD-OCT[51-56] and SD-OCT[57-64] technology. Improved reproducibility using SD-OCT has been reported.[15, 65] Recent development of eye tracking functionality in commercial SD-OCT has also been reported to provide improved reproducibility in both normal and glaucomatous eyes.[66] This study was designed with the major objective of evaluating the difference in RNFL thickness measurement reproducibility using standard raster scans and registered motion-corrected datasets in normal and glaucoma eyes acquired by an experienced operator. In addition, we wanted to determine whether the registration motion-correction algorithm can improve reproducibility when a less experienced operator ignores motion completely during OCT scan acquisition.

Previous studies have shown that RNFL thickness measurements in glaucomatous eyes being slightly more variable than in normal eyes.[52, 58, 67] Although the results from normal eyes in the first group of subjects show that comparing "minimal motion" and "minimal-motion registered", "first available" and "first-available registered", and "minimal motion" and "first-available registered" in normal eyes do not yield different reproducibility in RNFL thickness measurements around the 3.45mm diameter circle centered on the optic nerve head, the results from glaucoma subjects which have thinner RNFL show that the RNFL thickness measurement reproducibility in several quadrants and clock hours were statistically significantly improved. The "first available" scans are scans without blinking, vignetting, acquired within the imaging range, but may or may not have motion. Therefore, comparing the "first available" and "first-available registered" is comparable to the scenario that the experienced operator does not check for motion artifacts in the OCT fundus image showing eye motion larger than one vessel diameter or major distortions of the ONH. Furthermore, comparing "minimal motion" with both "minimal-motion registered" and "first-available registered" in glaucoma eyes, RNFL thickness reproducibility is mostly comparable and never worse while shown to be statistically improved in a several quadrants and clock hours. In sum, this suggests that the registration motion-correction algorithm is able to obtain RNFL thickness measurements in normal and glaucoma eyes with comparable reproducibility to standard raster scans with "minimal motion", while sometimes improving reproducibility in glaucoma eyes compared to the standard "minimal motion" scans. This finding is similar to the improvement using eye tracking which helps reduce the gap in reproducibility between normal and glaucomatous eyes previously reported by Langenegger et al.[66]

Results from the second group of subjects scanned by a relatively inexperienced operator suggest the possibility of neglecting motion during scan acquisition entirely when using the registration motion-correction algorithm. For the second group of subjects, the operator did not ask the subjects to hold position during scanning rather only asking them to look towards the fixation target in the OCT device. This resulted in high variability in RNFL thickness measurements. Both the temporal and nasal quadrants as well as most clock hours except 2, 3, and 12 were statistically significantly improved with the registration motion-correction algorithm. It is worth pointing out that the operation manuals of SD-OCT devices do not describe any motion criteria for scan acquisition. Also, the SD-OCT software only alerts the operator of blinks and low signal quality and does not alert the operator of motion artifacts. Although in literature most studies have protocols where scans with motion artifacts are discarded,(cite) operators may not always check for motion artifacts or successfully obtain scans with minimal motion during scan acquisition in clinical practice.

Reproducibilities reported in different studies should be compared with caution because of the different eyes, study protocols, imaging devices, scan patterns, ONH centration, and segmentation algorithms. Leung et al.[15] reported coefficients of variations (SD/mean) between 1.79% – 6.38% in global mean, quadrants, and clock hours of RNFL thickness measurements from 3D-OCT datasets acquired using Cirrus (Carl Zeiss Meditec, Dublin, CA) SD-OCT in 31 normal eyes where each eye was imaged in two separate visits in one month. Kim et al.[65] reported SD/mean values between 1.1% – 7.7% in global mean, quadrants, and clock hours of RNFL thickness measurements in 27 healthy eyes but with custom ONH centration and segmentation software analyzing three 3D-OCT scans acquired in a single session using Cirrus SD-OCT. Mwanza et al.[61] reported coefficient of variation values between 2.7% – 10.8% in global mean, quadrants, and clock hours of RNFL thickness measurements in 55 glaucomatous eyes from five 3D-OCT scans obtained on five different days within two months using the Cirrus SD-OCT. All three of these studies discarded scans with motion artifacts and only analyzed "minimal motion" datasets. The present study reports SD/mean values between 1.2% – 4.8% in global mean, quadrants, and clock hours of RNFL thickness measurements in normal eyes and 2.2% – 6.9% in glaucomatous eyes in "minimal motion" datasets. In registration motion-corrected datasets, the SD/mean values are between 1.0% – 5.6% in normal eyes and between 1.8% – 6.7% in glaucomatous eyes. Similar to the study using eye tracking with Spectralis (Heidelberg Engineering, Heidelberg, Germany) SD-OCT for RNFL thickness measurements[66], the lowest SD/mean value of 1.0% in normal eyes in our study using registration motion correction is one of the best reproducibilities ever reported for RNFL thickness measurements.

Several factors including signal quality, scan centration, and segmentation algorithm influence RNFL thickness measurements derived from OCT scans.[49, 68, 69] In this study, a two-dimensional frame-by-frame segmentation algorithm was used in the RTVue software. Higher signal quality after registration motion-correction can improve segmentation as illustrated in Figure 3.3. Nevertheless, registration motion-corrected datasets enables advanced 3D segmentation algorithms that may yield better performance. Centering of the virtual 3.45 mm diameter circle scan on the optic nerve head may also be improved with motion-corrected 3D datasets which closer represent true topography.[65] Although the registered datasets were acquired through two separate acquisitions in this study, higher speed OCT systems can acquire the orthogonally scanned raster scans continuously within a single acquisition.[70-72] With the higher scan speeds which inherently reduce motion artifacts along with registration motion correction and possibly eye tracking, reproducibility of RNFL thickness measurements can be further improved.

In conclusion, the reproducibility of RNFL thickness measurements using registration motion-corrected datasets was excellent in both normal and glaucomatous eyes. The registration motion-correction algorithm was able to improve RNFL thickness measurement reproducibility in most quadrants and clock hours in glaucoma eyes when comparing the "first available" scans, mimicking the scenario where the operator does not check for motion artifacts. In addition, when motion criteria were ignored during acquisition by a less experienced operator, the registration motion-correction algorithm was able to improve RNFL thickness measurement reproducibility in most quadrants and clock hours. Given the ability to correct for motion artifacts after OCT scan acquisition, the registration motion-correction algorithm improves RNFL thickness measurement reproducibility in glaucoma eyes. The registration motion-correction algorithm can enable relaxed motion criteria during acquisition which potentially leads to less operator dependency and development of widespread screening applications from multiple delivery points using handheld SD-OCT devices. The results in the present study show that the registration motion-correction algorithm is promising for measuring RNFL thickness in clinical practice and can improve the ability to detect small changes over time with high special accuracy.

3.6 References

1. Kraus MF, Potsaid B, Mayer MA, Bock R, Baumann B, Liu JJ, Hornegger J, Fujimoto JG. Motion correction in optical coherence tomography volumes on a per A-scan basis using orthogonal scan patterns. Biomedical optics express. 2012;3(6):1182-99. PubMed PMID: ISI:000304965700005.

2. Podgor MJ, Leske MC, Ederer F. Incidence estimates for lens changes, macular changes, open-angle glaucoma and diabetic retinopathy. Am J Epidemiol. 1983;118(2):206-12. PubMed PMID: 6881126.

3. Leske MC, Heijl A, Hussein M, Bengtsson B, Hyman L, Komaroff E. Factors for glaucoma progression and the effect of treatment: the early manifest glaucoma trial. Arch Ophthalmol. 2003;121(1):48-56. PubMed PMID: 12523884.

4. Goldberg I. Relationship between intraocular pressure and preservation of visual field in glaucoma. Surv Ophthalmol. 2003;48 Suppl 1:S3-7. PubMed PMID: 12852428.

5. The Advanced Glaucoma Intervention Study (AGIS): 7. The relationship between control of intraocular pressure and visual field deterioration.The AGIS Investigators. Am J Ophthalmol. 2000;130(4):429-40. PubMed PMID: 11024415.

6. Lichter PR. Variability of expert observers in evaluating the optic disc. Trans Am Ophthalmol Soc. 1976;74:532-72. PubMed PMID: 867638.

7. Gaasterland DE, Blackwell B, Dally LG, Caprioli J, Katz LJ, Ederer F. The Advanced Glaucoma Intervention Study (AGIS): 10. Variability among academic glaucoma subspecialists in assessing optic disc notching. Trans Am Ophthalmol Soc. 2001;99:177-84; discussion 84-5. PubMed PMID: 11797305.

8. Quigley HA, Addicks EM, Green WR. Optic nerve damage in human glaucoma. III. Quantitative correlation of nerve fiber loss and visual field defect in glaucoma, ischemic neuropathy, papilledema, and toxic neuropathy. Arch Ophthalmol. 1982;100(1):135-46. PubMed PMID: 7055464.

9. Sommer A, Katz J, Quigley HA, Miller NR, Robin AL, Richter RC, Witt KA. Clinically detectable nerve fiber atrophy precedes the onset of glaucomatous field loss. Arch Ophthalmol. 1991;109(1):77-83. PubMed PMID: 1987954.

10. Schuman JS, Hee MR, Arya AV, Pedut-Kloizman T, Puliafito CA, Fujimoto JG, Swanson EA. Optical coherence tomography: a new tool for glaucoma diagnosis. Current opinion in ophthalmology. 1995;6(2):89-95. PubMed PMID: PMID: 10150863; Medline: 95399928 Provider: OCLC.

11. Schuman JS, PedutKloizman T, Hertzmark E, Hee MR, Wilkins JR, Coker JG, Puliafito CA, Fujimoto JG, Swanson EA. Reproducibility of nerve fiber layer thickness measurements using optical coherence tomography. Ophthalmology. 1996;103(11):1889-98. PubMed PMID: ISI:A1996VU09700040.

12. Schuman JS, Hee MR, Puliafito CA, Wong C, Pedut-Kloizman T, Lin CP, Hertzmark E, Izatt JA, Swanson EA, Fujimoto JG. Quantification of nerve fiber layer thickness in normal and glaucomatous eyes using optical coherence tomography. Arch Ophthalmol. 1995;113(5):586-96. PubMed PMID: PMID: 7748128; Medline: 95267006 Provider: OCLC.

13. Carl Zeiss Meditec I. Stratus OCT™ with Software Version 5.0 Real Answers in Real Time. USA2008. p. 1-12.

14. Kim JS, Ishikawa H, Sung KR, Xu J, Wollstein G, Bilonick RA, Gabriele ML, Kagemann L, Duker JS, Fujimoto JG, Schuman JS. Retinal nerve fibre layer thickness measurement reproducibility improved with spectral domain optical coherence tomography. Brit J Ophthalmol. 2009;93(8):1057-63. doi: DOI 10.1136/bjo.2009.157875. PubMed PMID: ISI:000268302000015.

15. Leung CK, Cheung CY, Weinreb RN, Qiu Q, Liu S, Li H, Xu G, Fan N, Huang L, Pang CP, Lam DS. Retinal Nerve Fiber Layer Imaging with Spectral-Domain Optical Coherence Tomography A Variability and Diagnostic Performance Study. Ophthalmology. 2009. PubMed PMID: 19464061.

16. Sung KR, Kim DY, Park SB, Kook MS. Comparison of Retinal Nerve Fiber Layer Thickness Measured by Cirrus HD and Stratus Optical Coherence Tomography. Ophthalmology. 2009. PubMed PMID: 19427696.

17. Schuman JS, Hee MR, Puliafito CA, Wong C, Pedutkloizman T, Lin CP, Hertzmark E, Izatt JA, Swanson EA, Fujimoto JG. Quantification of Nerve-Fiber Layer Thickness in Normal and Glaucomatous Eyes Using Optical Coherence Tomography - a Pilot-Study. Investigative Ophthalmology & Visual Science. 1995;36(4):S389-S. PubMed PMID: ISI:A1995QM91501820.

18. Wollstein G, Schuman JS, Price LL, Aydin A, Stark PC, Hertzmark E, Lai E, Ishikawa H, Mattox C, Fujimoto JG, Paunescu LA. Optical coherence tomography longitudinal evaluation of retinal nerve fiber layer thickness in glaucoma. Arch Ophthalmol. 2005;123(4):464-70. PubMed PMID: 15824218.

19. Pieroth L, Schuman JS, Hertzmark E, Hee MR, Wilkins JR, Coker J, Mattox C, Pedut-Kloizman R, Puliafito CA, Fujimoto JG, Swanson E. Evaluation of focal defects of the nerve fiber layer using optical coherence tomography. Ophthalmology. 1999;106(3):570-9. PubMed PMID: PMID: 10080216; Medline: 99178301 Provider: OCLC.

20. Williams ZY, Schuman JS, Gamell L, Nemi A, Hertzmark E, Fujimoto JG, Mattox C, Simpson J, Wollstein G. Optical coherence tomography measurement of nerve fiber layer thickness and the likelihood of a visual field defect. Am J Ophthalmol. 2002;134(4):538-46. PubMed PMID: PMID: 12383810; Medline: 22272536 Provider: OCLC.

21. Mok KH, Lee VW, So KF. Retinal nerve fiber loss pattern in high-tension glaucoma by optical coherence tomography. J Glaucoma. 2003;12(3):255-9. PubMed PMID: PMID: 12782845; Medline: 22666916 Provider: OCLC.

22. Bowd C, Weinreb RN, Williams JM, Zangwill LM. The retinal nerve fiber layer thickness in ocular hypertensive, normal, and glaucomatous eyes with optical coherence tomography. Arch Ophthalmol. 2000;118(1):22-6. PubMed PMID: PMID: 10636409; Medline: 20100364 Provider: OCLC.

23. Mistlberger A, Liebmann JM, Greenfield DS, Pons ME, Hoh ST, Ishikawa H, Ritch R. Heidelberg retina tomography and optical coherence tomography in normal, ocular-hypertensive, and glaucomatous eyes. Ophthalmology. 1999;106(10):2027-32. PubMed PMID: PMID: 10519603; Medline: 99447092 Provider: OCLC.

24. Nouri-Mahdavi K, Hoffman D, Tannenbaum DP, Law SK, Caprioli J. Identifying early glaucoma with optical coherence tomography. Am J Ophthalmol. 2004;137(2):228-35. PubMed PMID: 14962410.

25. Soliman MA, Van Den Berg TJ, Ismaeil AA, De Jong LA, De Smet MD. Retinal nerve fiber layer analysis: relationship between optical coherence tomography and red-free photography. Am J Ophthalmol. 2002;133(2):187-95. PubMed PMID: PMID: 11812421; Medline: 21670751 Provider: OCLC.

26. Zangwill LM, Williams J, Berry CC, Knauer S, Weinreb RN. A comparison of optical coherence tomography and retinal nerve fiber layer photography for detection of nerve fiber layer damage in glaucoma. Ophthalmology. 2000;107(7):1309-15. PubMed PMID: PMID: 10889104; Medline: 20349640 Provider: OCLC.

27. Greaney MJ, Hoffman DC, Garway-Heath DF, Nakla M, Coleman AL, Caprioli J. Comparison of optic nerve imaging methods to distinguish normal eyes from those with glaucoma. Investigative ophthalmology & visual science. 2002;43(1):140-5. PubMed PMID: PMID: 11773024; Medline: 21634755 Provider: OCLC.

28. Bowd C, Zangwill LM, Berry CC, Blumenthal EZ, Vasile C, Sanchez-Galeana C, Bosworth CF, Sample PA, Weinreb RN. Detecting early glaucoma by assessment of retinal nerve fiber layer thickness and visual function. Investigative ophthalmology & visual science. 2001;42(9):1993-2003. PubMed PMID: PMID: 11481263; Medline: 21374008 Provider: OCLC.

29. Wollstein G, Schuman JS, Price LL, Aydin A, Beaton SA, Stark PC, Fujimoto JG, Ishikawa H. Optical coherence tomography (OCT) macular and peripapillary retinal nerve fiber layer measurements and automated visual fields. Am J Ophthalmol. 2004;138(2):218-25. PubMed PMID: ISI:000223186100007.

30. Ishikawa H, Stein DM, Wollstein G, Beaton S, Fujimoto JG, Schuman JS. Macular segmentation with optical coherence tomography. Invest Ophthalmol Vis Sci. 2005;46(6):2012-7. PubMed PMID: 15914617.

31. Schuman JS, Wollstein G, Farra T, Hertzmark E, Aydin A, Fujimoto JG, Paunescu LA. Comparison of optic nerve head measurements obtained by optical coherence tomography and confocal scanning laser ophthalmoscopy. Am J Ophthalmol. 2003;135(4):504-12. PubMed PMID: PMID: 12654368; Medline: 22540543 Provider: OCLC.

32. Lederer DE, Schuman JS, Hertzmark E, Heltzer J, Velazques LJ, Fujimoto JG, Mattox C. Analysis of macular volume in normal and glaucomatous eyes using optical coherence tomography. Am J Ophthalmol. 2003;135(6):838-43. PubMed PMID: PMID: 12788124; Medline: 22670390 Provider: OCLC.

33. Guedes V, Schuman JS, Hertzmark E, Wollstein G, Correnti A, Mancini R, Lederer D, Voskanian S, Velazquez L, Pakter HM, Pedut-Kloizman T, Fujimoto JG, Mattox C. Optical coherence tomography measurement of macular and nerve fiber layer thickness in normal and glaucomatous human eyes. Ophthalmology. 2003;110(1):177-89. PubMed PMID: PMID: 12511364; Medline: 22399980 Provider: OCLC.

34. Greenfield DS, Bagga H, Knighton RW. Macular thickness changes in glaucomatous optic neuropathy detected using optical coherence tomography. Arch Ophthalmol. 2003;121(1):41-6. PubMed PMID: PMID: 12523883; Medline: 22411759 Provider: OCLC.

35. Bagga H, Greenfield DS. Quantitative assessment of structural damage in eyes with localized visual field abnormalities. Am J Ophthalmol. 2004;137(5):797-805. PubMed PMID: 15126142.

36. Leung CK, Chan WM, Yung WH, Ng AC, Woo J, Tsang MK, Tse RK. Comparison of macular and peripapillary measurements for the detection of glaucoma: an optical coherence tomography study. Ophthalmology. 2005;112(3):391-400. PubMed PMID: 15745764.

37. Ojima T, Tanabe T, Hangai M, Yu S, Morishita S, Yoshimura N. Measurement of retinal nerve fiber layer thickness and macular volume for glaucoma detection using optical coherence tomography. Jpn J Ophthalmol. 2007;51(3):197-203. PubMed PMID: ISI:000247179100006.

38. Wollstein G, Ishikawa H, Wang J, Beaton SA, Schuman JS. Comparison of three optical coherence tomography scanning areas for detection of glaucomatous damage. Am J Ophthalmol. 2005;139(1):39-43. PubMed PMID: 15652826.

39. Medeiros FA, Zangwill LM, Bowd C, Vessani RM, Susanna R, Jr., Weinreb RN. Evaluation of retinal nerve fiber layer, optic nerve head, and macular thickness measurements for glaucoma detection using optical coherence tomography. Am J Ophthalmol. 2005;139(1):44-55. PubMed PMID: 15652827.

40. Tan O, Li G, Lu ATH, Varma R, Huang D, Grp LALES. Mapping of macular substructures with optical coherence tomography for glaucoma diagnosis. Ophthalmology. 2008;115(6):949-56. doi: DOI 10.1016/j.ophtha.2007.08.011. PubMed PMID: ISI:000256282800005.

41. Wojtkowski M, Leitgeb R, Kowalczyk A, Bajraszewski T, Fercher AF. In vivo human retinal imaging by Fourier domain optical coherence tomography. J Biomed Opt. 2002;7(3):457-63.

42. Wojtkowski M, Bajraszewski T, Targowski P, Kowalczyk A. Real-time in vivo imaging by high-speed spectral optical coherence tomography. Opt Lett. 2003;28(19):1745-7.

43. Leitgeb R, Hitzenberger CK, Fercher AF. Performance of Fourier domain vs. time domain optical coherence tomography. Optics Express. 2003;11(8):889-94.

44. de Boer JF, Cense B, Park BH, Pierce MC, Tearney GJ, Bouma BE. Improved signal-to-noise ratio in spectral-domain compared with time-domain optical coherence tomography. Opt Lett. 2003;28(21):2067-9. PubMed PMID: 14587817.

45. Choma MA, Sarunic MV, Yang CH, Izatt JA. Sensitivity advantage of swept source and Fourier domain optical coherence tomography. Optics Express. 2003;11(18):2183-9. PubMed PMID: ISI:000185185000012.

46. Wojtkowski M, Srinivasan V, Fujimoto JG, Ko T, Schuman JS, Kowalczyk A, Duker JS. Three-dimensional retinal imaging with high-speed ultrahigh-resolution optical coherence tomography. Ophthalmology. 2005;112(10):1734-46. PubMed PMID: 16140383.

47. Mujat M, Chan R, Cense B, Park B, Joo C, Akkin T, Chen T, de Boer J. Retinal nerve fiber layer thickness map determined from optical coherence tomography images. Opt Express. 2005;13(23):9480-91.

48. Gabriele ML, Ishikawa H, Wollstein G, Bilonick RA, Kagemann L, Wojtkowski M, Srinivasan VJ, Fujimoto JG, Duker JS, Schuman JS. Peripapillary nerve fiber layer thickness profile determined with high speed, ultrahigh resolution optical coherence tomography high-density scanning. Investigative Ophthalmology & Visual Science. 2007;48(7):3154-60. PubMed PMID: ISI:000247855600028.

49. Gabriele ML, Ishikawa H, Wollstein G, Bilonick RA, Townsend KA, Kagemann L, Wojtkowski M, Srinivasan VJ, Fujimoto JG, Duker JS, Schuman JS. Optical coherence tomography scan circle location and mean retinal nerve fiber layer measurement variability. Invest Ophthalmol Vis Sci. 2008;49(6):2315-21. PubMed PMID: 18515577.

50. Ho J, Castro DP, Castro LC, Chen Y, Liu J, Mattox C, Krishnan C, Fujimoto JG, Schuman JS, Duker JS. Clinical assessment of mirror artifacts in spectral-domain optical coherence tomography. Invest Ophthalmol Vis Sci. 2010;51(7):3714-20. Epub 2010/02/26. doi: 10.1167/iovs.09-4057 [pii]. PubMed PMID: 20181840; PubMed Central PMCID: PMC2904018.

51. Blumenthal EZ, Williams JM, Weinreb RN, Girkin CA, Berry CC, Zangwill LM. Reproducibility of nerve fiber layer thickness measurements by use of optical coherence tomography. Ophthalmology. 2000;107(12):2278-82. Epub 2000/11/30. doi: S0161642000003419 [pii]. PubMed PMID: 11097610.

52. Budenz DL, Chang RT, Huang X, Knighton RW, Tielsch JM. Reproducibility of retinal nerve fiber thickness measurements using the stratus OCT in normal and glaucomatous eyes. Invest Ophthalmol Vis Sci. 2005;46(7):2440-3. Epub 2005/06/28. doi: 46/7/2440 [pii] 10.1167/iovs.04-1174. PubMed PMID: 15980233.

53. Carpineto P, Ciancaglini M, Zuppardi E, Falconio G, Doronzo E, Mastropasqua L. Reliability of nerve fiber layer thickness measurements using optical coherence tomography in normal and glaucomatous eyes. Ophthalmology. 2003;110(1):190-5. Epub 2003/01/04. doi: S0161-6420(02)01296-4 [pii]. PubMed PMID: 12511365.

54. Jones AL, Sheen NJ, North RV, Morgan JE. The Humphrey optical coherence tomography scanner: quantitative analysis and reproducibility study of the normal human retinal nerve fibre layer. Br J Ophthalmol. 2001;85(6):673-7. Epub 2001/05/24. PubMed PMID: 11371486; PubMed Central PMCID: PMC1723988.

55. Paunescu LA, Schuman JS, Price LL, Stark PC, Beaton S, Ishikawa H, Wollstein G, Fujimoto JG. Reproducibility of nerve fiber thickness, macular thickness, and optic nerve head measurements using StratusOCT. Invest Ophthalmol Vis Sci. 2004;45(6):1716-24. Epub 2004/05/27. PubMed PMID: 15161831; PubMed Central PMCID: PMC1993821.

56. Schuman JS, Pedut-Kloizman T, Hertzmark E, Hee MR, Wilkins JR, Coker JG, Puliafito CA, Fujimoto JG, Swanson EA. Reproducibility of nerve fiber layer thickness measurements using optical coherence tomography. Ophthalmology. 1996;103(11):1889-98. Epub 1996/11/01. PubMed PMID: 8942887; PubMed Central PMCID: PMC1939724.

57. Menke MN, Knecht P, Sturm V, Dabov S, Funk J. Reproducibility of nerve fiber layer thickness measurements using 3D fourier-domain OCT. Invest Ophthalmol Vis Sci. 2008;49(12):5386-91. Epub 2008/08/05. doi: 10.1167/iovs.07-1435 [pii]. PubMed PMID: 18676630.

58. Gonzalez-Garcia AO, Vizzeri G, Bowd C, Medeiros FA, Zangwill LM, Weinreb RN. Reproducibility of RTVue retinal nerve fiber layer thickness and optic disc measurements and agreement with Stratus optical coherence tomography measurements. Am J Ophthalmol. 2009;147(6):1067-74, 74 e1. Epub 2009/03/10. doi: 10.1016/j.ajo.2008.12.032 S0002-9394(08)00972-0 [pii]. PubMed PMID: 19268891; PubMed Central PMCID: PMC3465966.

59. Vizzeri G, Weinreb RN, Gonzalez-Garcia AO, Bowd C, Medeiros FA, Sample PA, Zangwill LM. Agreement between spectral-domain and time-domain OCT for measuring RNFL thickness. Br J Ophthalmol. 2009;93(6):775-81. Epub 2009/03/24. doi: 10.1136/bjo.2008.150698 bjo.2008.150698 [pii]. PubMed PMID: 19304586; PubMed Central PMCID: PMC3465953.

60. Garas A, Vargha P, Hollo G. Reproducibility of retinal nerve fiber layer and macular thickness measurement with the RTVue-100 optical coherence tomograph. Ophthalmology. 2010;117(4):738-46. Epub 2010/01/19. doi: 10.1016/j.ophtha.2009.08.039 S0161-6420(09)00977-4 [pii]. PubMed PMID: 20079538.

61. Mwanza JC, Chang RT, Budenz DL, Durbin MK, Gendy MG, Shi W, Feuer WJ. Reproducibility of peripapillary retinal nerve fiber layer thickness and optic nerve head parameters measured with cirrus HD-OCT in glaucomatous eyes. Invest Ophthalmol Vis Sci. 2010;51(11):5724-30. Epub 2010/06/25. doi: 10.1167/iovs.10-5222 [pii]. PubMed PMID: 20574014; PubMed Central PMCID: PMC3061508.

62. Lee SH, Kim SH, Kim TW, Park KH, Kim DM. Reproducibility of retinal nerve fiber thickness measurements using the test-retest function of spectral OCT/SLO in normal and glaucomatous eyes. J Glaucoma. 2010;19(9):637-42. Epub 2010/02/23. doi: 10.1097/IJG.0b013e3181ca7cbe. PubMed PMID: 20173650.

63. Wu H, de Boer JF, Chen TC. Reproducibility of retinal nerve fiber layer thickness measurements using spectral domain optical coherence tomography. J Glaucoma. 2011;20(8):470-6. Epub 2010/09/21. doi: 10.1097/IJG.0b013e3181f3eb64. PubMed PMID: 20852437; PubMed Central PMCID: PMC3500562.

64. Roh KH, Jeoung JW, Park KH, Yoo BW, Kim DM. Long-term reproducibility of cirrus HD optical coherence tomography deviation map in clinically stable glaucomatous eyes. Ophthalmology. 2013;120(5):969-77. Epub 2013/02/13. doi: 10.1016/j.ophtha.2012.11.008 S0161-6420(12)01074-3 [pii]. PubMed PMID: 23399380.

65. Kim JS, Ishikawa H, Sung KR, Xu J, Wollstein G, Bilonick RA, Gabriele ML, Kagemann L, Duker JS, Fujimoto JG, Schuman JS. Retinal nerve fibre layer thickness measurement reproducibility improved with spectral domain optical coherence tomography. Br J Ophthalmol. 2009;93(8):1057-63. Epub 2009/05/12. doi: bjo.2009.157875 [pii] 10.1136/bjo.2009.157875. PubMed PMID: 19429591; PubMed Central PMCID: PMC2861342.

66. Langenegger SJ, Funk J, Toteberg-Harms M. Reproducibility of retinal nerve fiber layer thickness measurements using the eye tracker and the retest function of Spectralis SD-OCT in glaucomatous and healthy control eyes. Invest Ophthalmol Vis Sci. 2011;52(6):3338-44. Epub 2011/02/19. doi: 10.1167/iovs.10-6611 [pii]. PubMed PMID: 21330656.

67. Budenz DL, Fredette MJ, Feuer WJ, Anderson DR. Reproducibility of peripapillary retinal nerve fiber thickness measurements with stratus OCT in glaucomatous eyes. Ophthalmology. 2008;115(4):661-6 e4. Epub 2007/08/21. doi: S0161-6420(07)00589-1 [pii] 10.1016/j.ophtha.2007.05.035. PubMed PMID: 17706287.

68. Sung KR, Wollstein G, Schuman JS, Bilonick RA, Ishikawa H, Townsend KA, Kagemann L, Gabriele ML. Scan quality effect on glaucoma discrimination by glaucoma imaging devices. Br J Ophthalmol. 2009;93(12):1580-4. Epub 2009/08/21. doi: 10.1136/bjo.2008.152223 [pii]. PubMed PMID: 19692363; PubMed Central PMCID: PMC2917916.

69. Kim JH, Kim NR, Kim H, Lee ES, Seong GJ, Kim CY. Effect of signal strength on reproducibility of circumpapillary retinal nerve fiber layer thickness measurement and its classification by spectral-domain optical coherence tomography. Jpn J Ophthalmol. 2011;55(3):220-7. Epub 2011/05/12. doi: 10.1007/s10384-011-0023-5. PubMed PMID: 21559911.

70. Potsaid B, Gorczynska I, Srinivasan VJ, Chen YL, Jiang J, Cable A, Fujimoto JG. Ultrahigh speed Spectral/Fourier domain OCT ophthalmic imaging at 70,000 to 312,500 axial scans per second. Optics Express. 2008;16(19):15149-69. PubMed PMID: WOS:000259271900089.

71. Potsaid B, Baumann B, Huang D, Barry S, Cable AE, Schuman JS, Duker JS, Fujimoto JG. Ultrahigh speed 1050nm swept source/Fourier domain OCT retinal and anterior segment imaging at 100,000 to 400,000 axial scans per second. Opt Express. 2010;18(19):20029-48. Epub 2010/10/14. doi: 10.1364/OE.18.020029 205532 [pii]. PubMed PMID: 20940894; PubMed Central PMCID: PMC3136869.

72. Grulkowski I, Liu JJ, Potsaid B, Jayaraman V, Lu CD, Jiang J, Cable AE, Duker JS, Fujimoto JG. Retinal, anterior segment and full eye imaging using ultrahigh speed swept source OCT with vertical-cavity surface emitting lasers. Biomed Opt Express. 2012;3(11):2733-51. PubMed PMID: ISI:000310644700005.

CHAPTER 4

Imaging Non-exudative (Dry) AMD using Ultrahigh Resolution Spectral / Fourier Domain OCT

4.1 Background

Age-related macular degeneration (AMD) is the leading cause of blindness in the elderly population in developed countries including the United States.[1-3] AMD is generally classified into two subgroups: non-exudative (dry) and exudative (wet) AMD. Non-exudative AMD comprises about 90% of all diagnosed patients and usually features drusen and other abnormalities of the retinal pigment epithelium (RPE). Moderately advanced dry A alone is estimated to affect more than 8 million Americans over 55 years of age.[4] Dry AMD can progress to late stages, such as geographic atrophy and wet AMD and results in serious vision loss. The majority of patients (about 88%) who experience severe visual loss develop the wet AMD[5], which features choroidal neovascularization (CNV) and scar formation[6]. Recently, vascular endothelial growth factor (VEGF) inhibiting therapies such as intravitreal injections of ranibizumab (Lucentis) and bevacizumab (Avastin) have shown remarkable clinical efficacy.[7-9] Two large, phase 3 trials evaluated ranibizumab treatment for wet AMD. Both showed stabilization or improvement of vision in the majority of wet AMD patients.[7, 8] OCT is useful for diagnosing and monitoring patients with wet AMD under treatment.[7, 10-14] A clinical study using time-domain OCT technology to decide treatment interval demonstrated comparable visual results with considerably fewer treatments than the 24 monthly injections performed in the phase 3 studies.[15, 16] A further study demonstrated that spectral / Fourier domain OCT (SD-OCT) devices have higher detection rates of CNV after ranibizumab treatment for wet AMD compared to time-domain OCT.[17] Although currently there are no effective treatments available for dry AMD, new approaches such as antioxidant[18], complement inhibitor[19], and immuno-modulatory[20] therapies are being examined. Recent studies demonstrate the ability of SD-OCT to identify and quantitate morphology in dry AMD.[21-24] Other studies show that en face OCT fundus images directly correlate with conventional fundus imaging methods.[25-27] These capabilities of SD-OCT will allow more sensitive measurements of response to therapy and could be useful to assess progression of dry AMD. Dry AMD is the target for the next generation of pharmaceuticals and therefore methods which can assess progression and treatment response are of great interest. Development of ultrahigh speed, ultrahigh resolution technology with greatly improved speed and resolution (Figure 4.1) promises to provide a powerful clinical imaging tool for the identification, classification, and treatment of both the wet and dry forms of AMD.

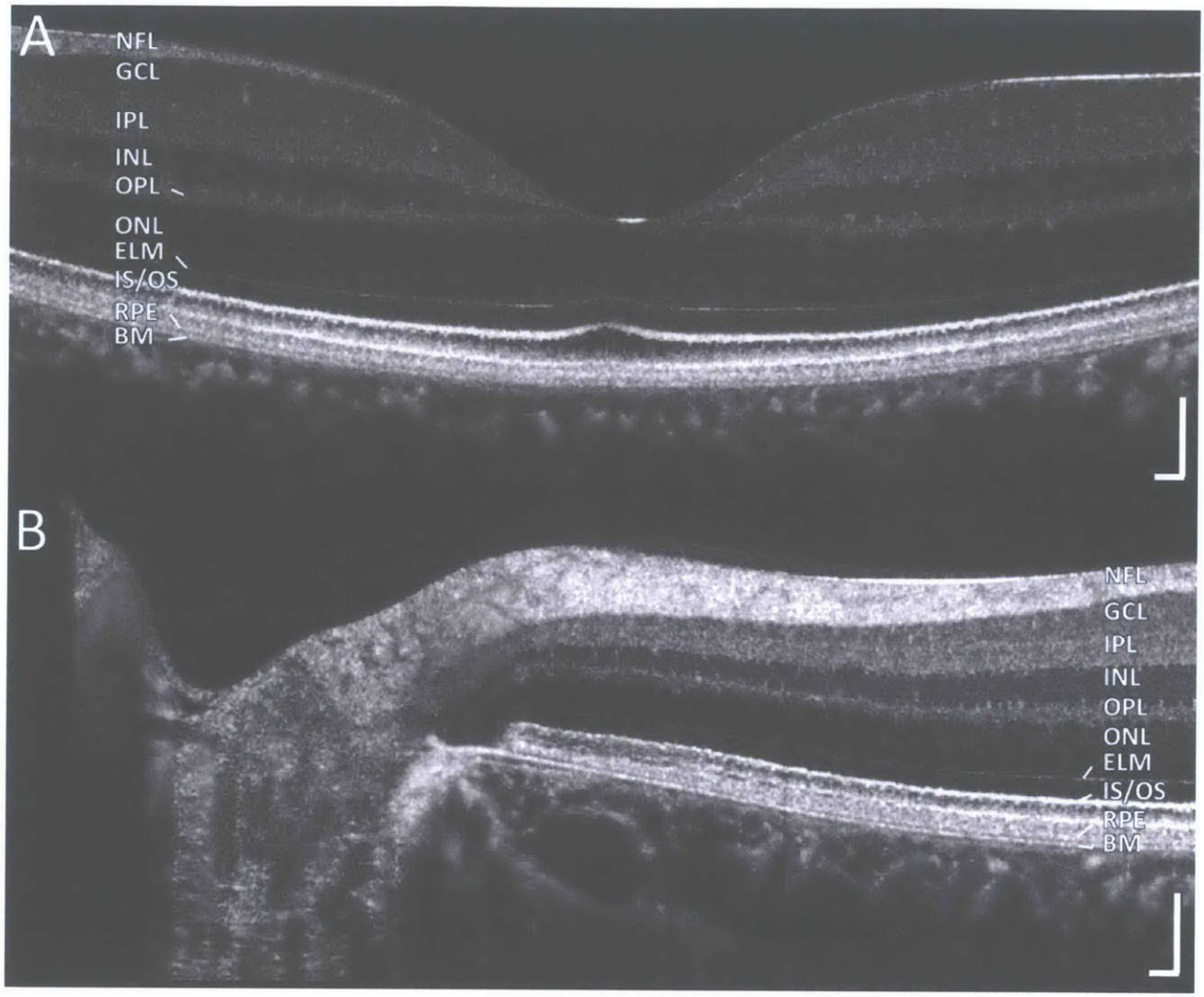

Figure 4.1 Ultrahigh speed, ultrahigh resolution imaging of a healthy eye using the clinical prototype system deployed at the New England Eye Center described in Chapter 2. These high-definition images are acquired by averaging 50 repeated frames of 1000 axial scans over the same 4 mm location over the foveal region (A) and near the optic nerve head (B). NFL – nerve fiber layer, GCL – ganglion cell layer, IPL – inner plexiform layer, INL – inner nuclear layer, OPL – outer plexiform layer, ONL – outer nuclear layer, ELM – external limiting membrane, IS/OS – junction of photoreceptor inner and outer segments, IS – photoreceptor inner segment, OS – photoreceptor outer segment, RPE – retinal pigment epithelium. Scale bar: 100μm.

4.2 Methods

Using the clinical ultrahigh speed, ultrahigh resolution spectral / Fourier domain OCT system described in Chapter 2, 47 eyes of 31 dry AMD patients were imaged at the New England Eye Center at Tufts Medical Center The prototype OCT system operates at 91,000 axial scans per second with ~3 μm axial resolution

using a multiplexed SLD light source centered at 840nm.[28] Multiple 400 × 400 axial scan volumes over a 6 mm × 6 mm region centered on the fovea was acquired with orthogonal fast scanning directions. The registration algorithm described in chapter 3 was performed to generate a motion-corrected merged volume.[29] Cross-sectional images were extracted from the merged volume by averaging three neighboring frames. Figure 4.2 is a comparison of cross-sectional images from a 200 × 200 axial scan volume acquired from a commercial SD-OCT system with images from a registered volume acquired using our clinical prototype. This study was approved by the institutional review boards at Tufts Medical Center and the Massachusetts Institute of Technology. The research adhered to the Declaration of Helsinki and the Health Insurance Portability and Accountability Act. Signed informed consent was obtained from all participants.

A subgroup of 10 patients without geographic atrophy was selected for analysis of the photoreceptor layer. Drusen apexes were found by scrolling through all cross-sectional images. Manual measurements of the distance between the ELM and the RPE and the IS/OS and the RPE were performed at the drusen apexes. The drusen size was also determined by measuring the width of the drusen on the cross-sectional image at the drusen apex. Areas with no drusen were also selected for measurement by scrolling through the cross-sectional images to compare photoreceptor height. All measurement positions within the motion-corrected volumetric OCT dataset were recorded. Drusen were grouped by size according to the AREDS categories: large drusen (>125 μm), medium drusen (<125 μm & >63 μm), and small drusen (<63 μm). Photoreceptor height measurements at drusen apexes were compared with areas with no drusen.

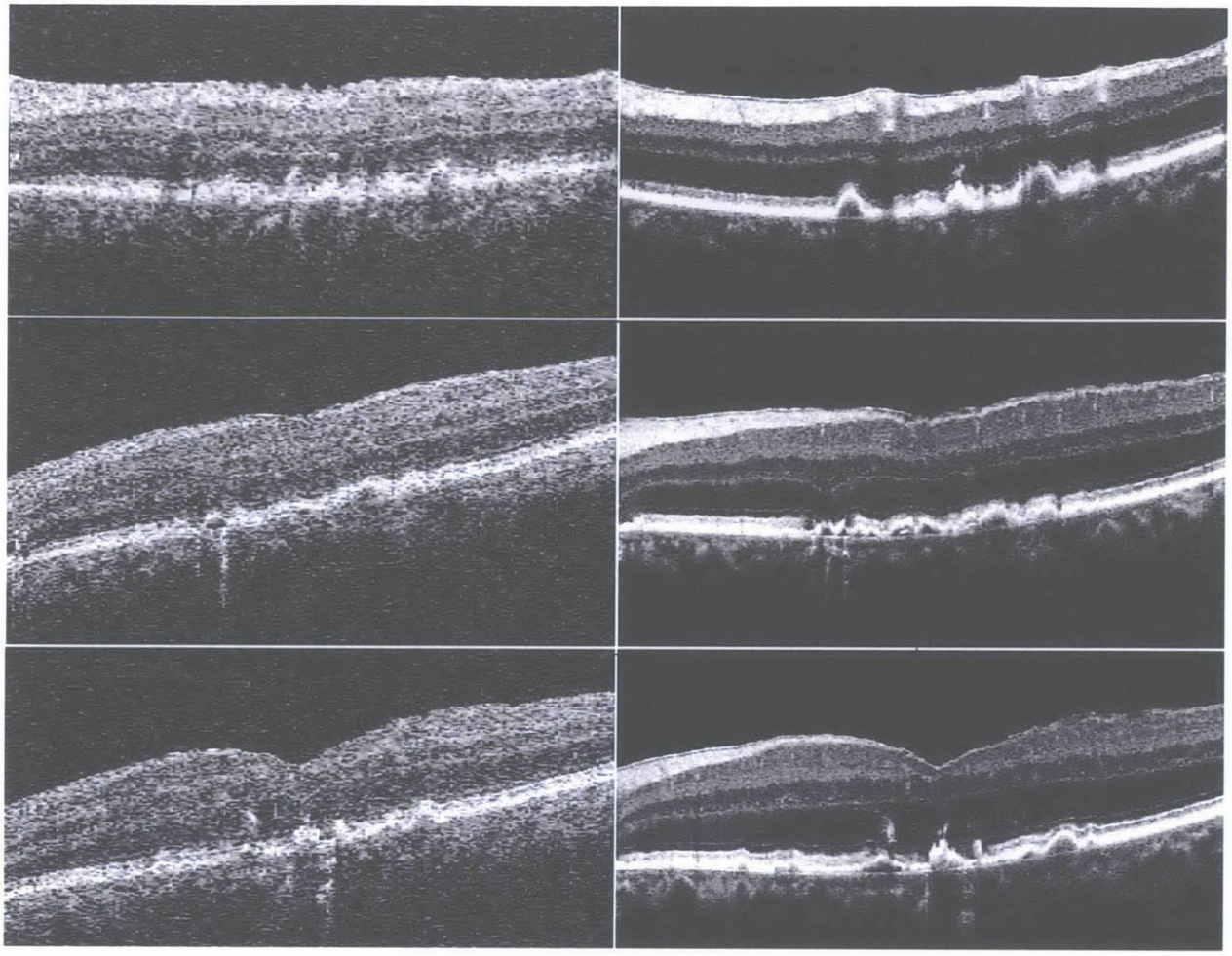

Figure 4.2 Visibility of micro-structural features from an non-exudative AMD eye using the ultrahigh speed, ultrahigh resolution OCT system with motion correction registration (right column) when comparing with the Cirrus macular cube 200 × 200 scan (left column).

4.3 Results

Features observed in the cross-sectional images extracted from the registered OCT volumes include basal linear deposits, reticular pseudodrusen, hyperreflective haze, drusen core reflectivity, and RPE pigment migration. Histology studies have suggested that basal linear deposits form drusen and the lipid wall above the Bruch's membrane and below the RPE layer. Figure 4.3 is a cross-sectional OCT image showing what may be the basal linear deposit or lipid wall in the same compartment as the drusen, in between the Bruch's membrane and the RPE. Another feature that can be observed in cross-sectional images extracted from the registered OCT volumes are reticular pseudodrusens as shown in Figure 4.4. Hyperreflective haze is another characteristic that can be observed in Figure 4.5. This feature is caused by the change in orientation of the Henle's fiber layer. Figure 4.6 depicts a variety of drusen core

reflectivity which is another feature of interest reported in previous studies. Figure 4.7 shows RPE pigment migration which have been reported in earlier studies by our group.

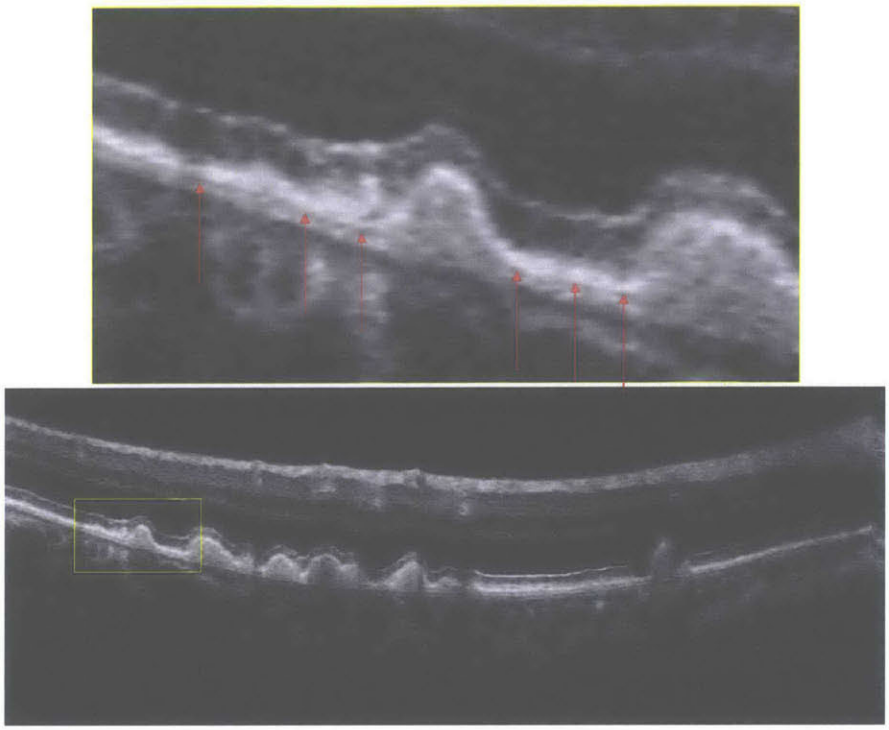

Figure 4.3 Basal linear deposits (red arrows) that may be the lipid wall, appearing to be in the same compartment as drusen. A zoom in view (top) of a cross-sectional OCT image (bottom) extracted from a registered OCT volume.

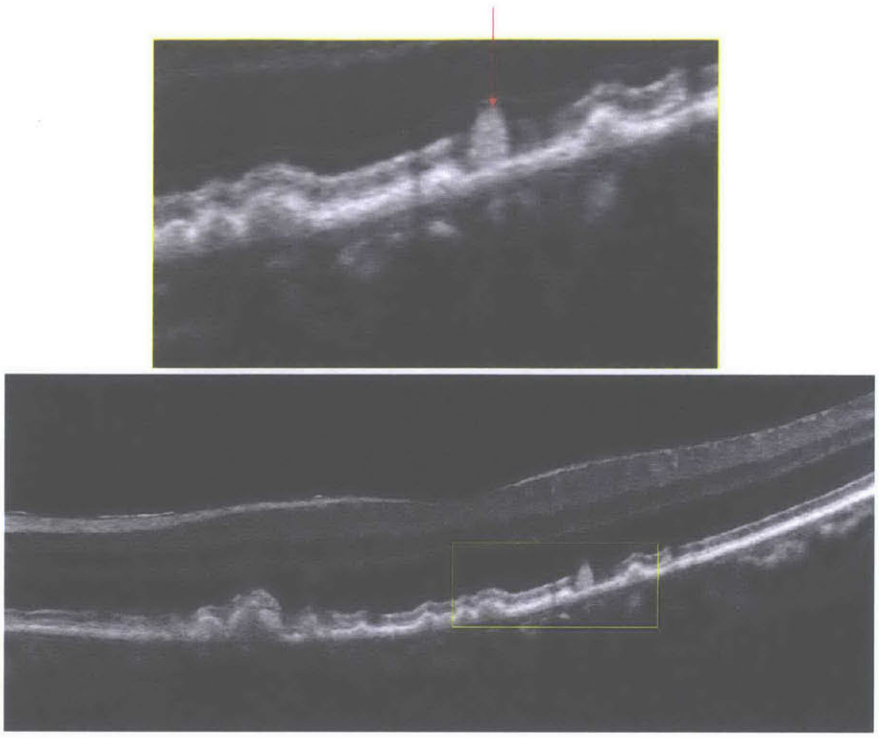

Figure 4.4 Reticular pseudodrusen (red arrow).

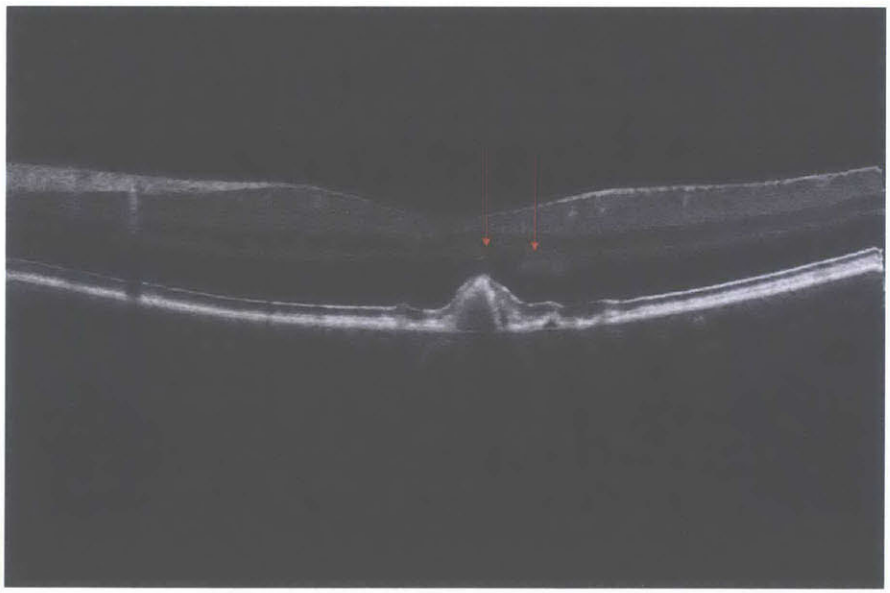

Figure 4.5 Hyperreflective haze (red arrows) .

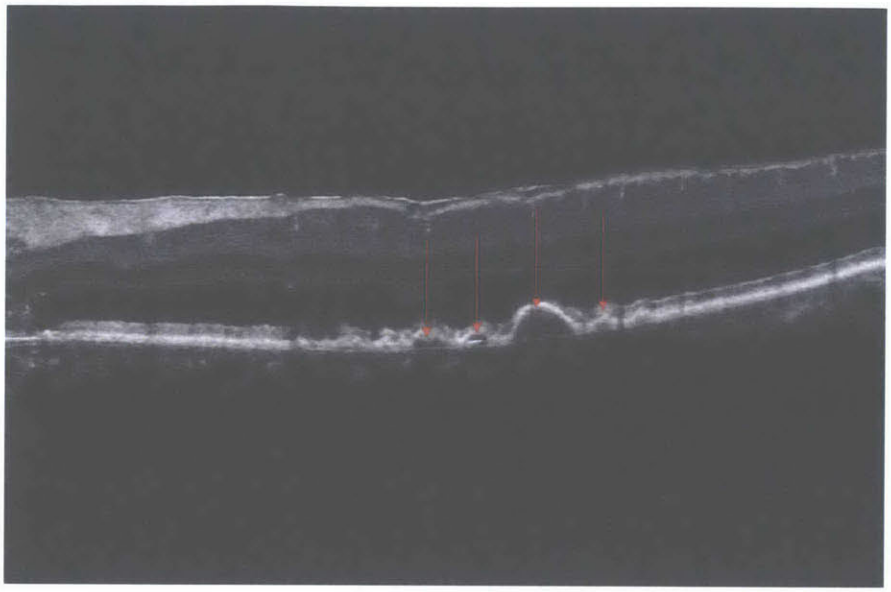

Figure 4.6 Drusen core reflectivity (red arrows).

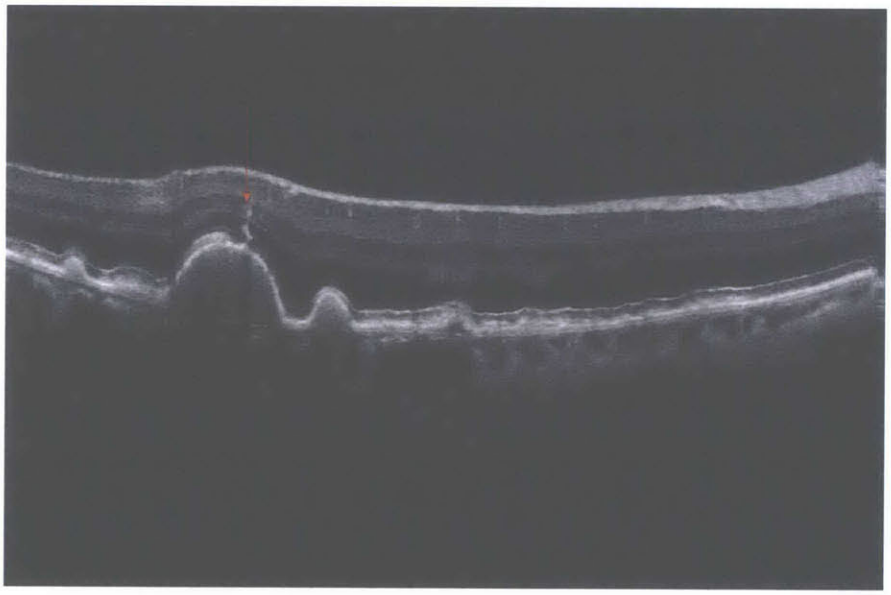

Figure 4.7 RPE pigment migration (red arrows).

Quantitative measurements of the distance between the ELM and the RPE and the IS/OS and the RPE performed at the drusen apexes are shown the Figure 4.8 and Figure 4.9. While the IS/OS-RPE thickness changes are not as obvious between intermediate drusen, small drusen, and regions with no drusen, the large drusen have a statistically significantly thinner IS/OS-RPE thickness. On the other hand, the ELM-RPE thickness seem to have a gradually decreasing trend. Although there is no significant difference between intermediate drusen and small drusen ($p = 0.115$), there is statistically significant

difference between large drusen and intermediate drusen ($p < 0.001$), intermediate drusen and no drusen ($p < 0.001$), and small drusen and no drusen ($p = 0.049$).

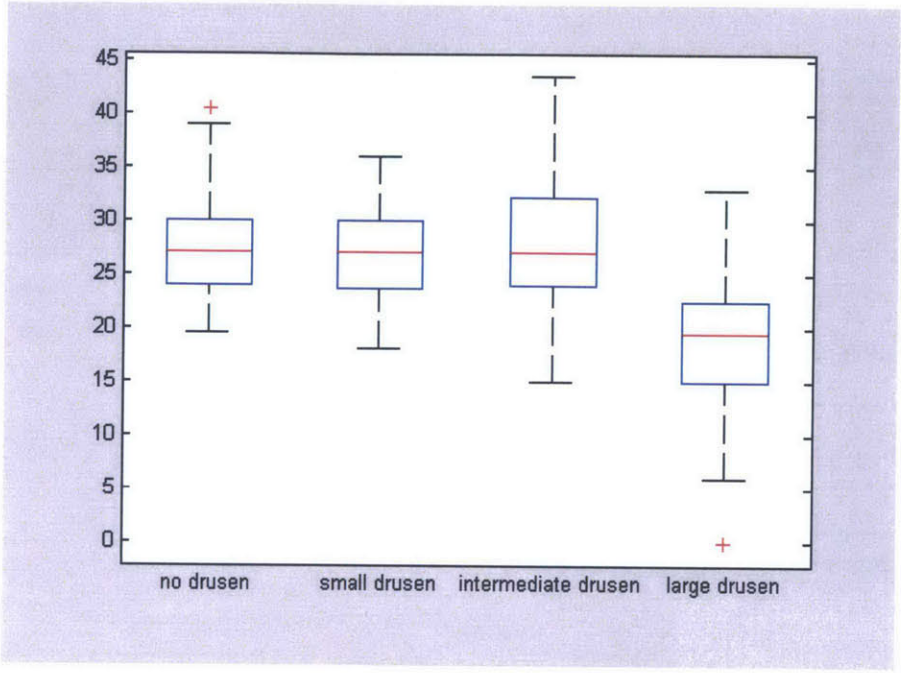

Figure 4.8 Box plot of IS/OS-RPE thickness measurements in μm.

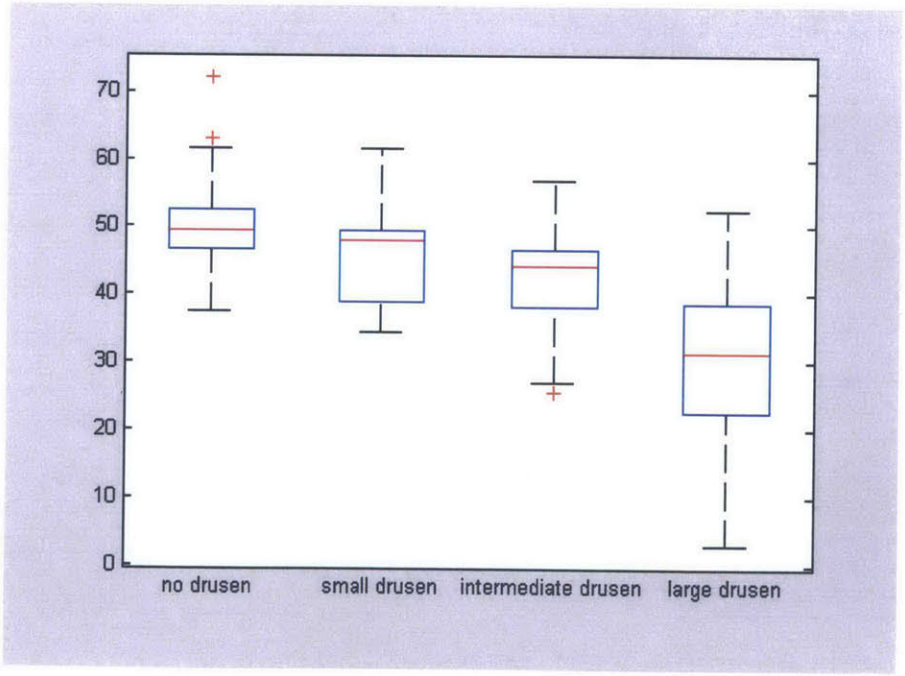

Figure 4.9 Box plot of ELM-RPE thickness measurements in μm.

4.4 Discussion

SDOCT technology[30-32] enabled in vivo imaging of multiple structural markers in eyes with drusen. One early study in 2008 classified drusen according to cross-sectional morphology.[22] Another study showed that drusen may contain material of varying reflectivities and sometimes have a hypo- or hyper-reflective "core".[33] A study on 143 eyes of 100 patients using the Zeiss Cirrus with a 200×200 A-scan volume investigated the natural history of drusen, showing that drusen are morphologically dynamic and demonstrating the possibility of developing quantitative OCT markers of dry AMD progression.[34] A recent study examined 750 large drusen (≥125 μm) in 63 intermediate AMD eyes observing significant reduction of the photoreceptor outer nuclear layer (ONL) thickness overlying 92% of the drusen and proportionally reduced photoreceptor inner and outer segment (IS+OS) thickness.[35]

In cases of focal hyper-pigmentation apparent on examination, our group found that hyper-reflective foci, likely indicating RPE pigment migration, are often visualized using SDOCT.[36] These hyper-reflective foci were later shown to be markers of development and/or progression of geographic atrophy (GA).[37] In the transition zone between healthy and atrophic retina in eyes with GA, the RPE height may appear increased or decreased in SDOCT images, suggesting RPE abnormalities.[38] Another study in eyes with GA demonstrated a variety of dynamic changes in these transition zones, including pigment migration and alterations in drusen height.[39] In some patients with rapidly progressing GA, a separation between the RPE and Bruch's membrane was evident at the transition zones.[40, 41] A recent study using en face OCT imaging with the Cirrus demonstrated quantitative measurement of GA area and enlargements rates.[42]

Focal photoreceptor thinning immediately overlying drusen and loss of photoreceptor outer segments was observed in subjects with dry AMD and drusen.[24] A longitudinal study of GA using the Heidelberg Spectralis showed loss of the photoreceptor IS/OS signal and outer nuclear layer thinning associated with GA enlargement.[39] A recent study using the Cirrus in eyes with GA showed en face OCT imaging of the IS/OS can predict GA growth.[43] Another recent study correlated SDOCT and multifocal electroretinography (mfERG) using Spectralis high definition images, showing that the normalized photoreceptor IS/OS signal decreased in early AMD and was significantly correlated with increased mfERG P1 implicit time (IT).[44] These studies demonstrate that OCT can quantitate markers of photoreceptor degeneration associated with AMD progression and suggest that functional changes also correlate with structural defects.

Reticular pseudodrusen are visualized in SDOCT as discrete collections of hyperreflective material located above the RPE as opposed to below the RPE in typical drusen.[45] Reticular pseudodrusen

are not risk factors for the development of late AMD, but there is high prevalence of late AMD among patients with pseudodrusen.[46, 47] Hyperreflective haze has been reported to be present above drusen.[24] This haze is believed to be the Henle's fiber layer which becomes hyperreflective due to changes in orientation relative to the OCT beam angle.[48, 49]

Histological studies have also shown that aging of Bruch's membrane causes accumulation of lipid-rich basal laminar deposits and basal linear deposits.[50, 51] Ultrahigh resolution OCT enables visualization of RPE and Bruch's membrane structure. The ability to detect changes in RPE and Bruch's membrane would be a powerful advance for tracking disease progression and response to therapy. However, controversy exists in the definition of inner retinal layer observed in OCT images and their correlation to histological features.[52] Ultrahigh speed, ultrahigh resolution spectral /Fourier domain OCT can provide high definition 3D-OCT datasets that may help improve the understanding of features observed in OCT an its correlation with histological observations.

4.5 References

1. Congdon N, O'Colmain B, Klaver CC, Klein R, Munoz B, Friedman DS, Kempen J, Taylor HR, Mitchell P. Causes and prevalence of visual impairment among adults in the United States. Arch Ophthalmol. 2004;122(4):477-85. PubMed PMID: 15078664.

2. Friedman DS, O'Colmain BJ, Munoz B, Tomany SC, McCarty C, de Jong PT, Nemesure B, Mitchell P, Kempen J. Prevalence of age-related macular degeneration in the United States. Arch Ophthalmol. 2004;122(4):564-72. PubMed PMID: 15078675.

3. Pascolini D, Mariotti SP, Pokharel GP, Pararajasegaram R, Etya'ale D, Negrel AD, Resnikoff S. 2002 global update of available data on visual impairment: a compilation of population-based prevalence studies. Ophthal Epidemiol. 2004;11(2):67-115. PubMed PMID: ISI:000221058800001.

4. Bressler NM, Bressler SB, Congdon NG, Ferris FL, 3rd, Friedman DS, Klein R, Lindblad AS, Milton RC, Seddon JM. Potential public health impact of Age-Related Eye Disease Study results: AREDS report no. 11. Arch Ophthalmol. 2003;121(11):1621-4. PubMed PMID: 14609922.

5. Ferris FL, 3rd, Fine SL, Hyman L. Age-related macular degeneration and blindness due to neovascular maculopathy. Arch Ophthalmol. 1984;102(11):1640-2. PubMed PMID: 6208888.

6. Bressler SB, Maguire MG, Bressler NM, Fine SL. Relationship of drusen and abnormalities of the retinal pigment epithelium to the prognosis of neovascular macular degeneration. The Macular Photocoagulation Study Group. Arch Ophthalmol. 1990;108(10):1442-7. PubMed PMID: 1699513.

7. Brown DM, Kaiser PK, Michels M, Soubrane G, Heier JS, Kim RY, Sy JP, Schneider S, Grp AS. Ranibizumab versus verteporfin for neovascular age-related macular degeneration. New England Journal of Medicine. 2006;355(14):1432-44. PubMed PMID: WOS:000240976200005.

8. Rosenfeld PJ, Brown DM, Heier JS, Boyer DS, Kaiser PK, Chung CY, Kim RY, Grp MS. Ranibizumab for neovascular age-related macular degeneration. New England Journal of Medicine. 2006;355(14):1419-31. PubMed PMID: WOS:000240976200004.

9. Avery RL, Pieramici DJ, Rabena MD, Castellarin AA, Nasir MA, Giust MJ. Intravitreal bevacizumab (Avastin) for neovascular age-related macular degeneration. Ophthalmology. 2006;113(3):363-72. PubMed PMID: ISI:000235694200002.

10. Kaiser PK, Do DV. Ranibizumab for the treatment of neovascular AMD. International Journal of Clinical Practice. 2007;61(3):501-9. doi: 10.1111/j.1742-1241.2007.01299.x. PubMed PMID: WOS:000244243500030.

11. Rogers AH, Martidis A, Greenberg PB, Puliafito CA. Optical coherence tomography findings following photodynamic therapy of choroidal neovascularization. Am J Ophthalmol. 2002;134(4):566-76. PubMed PMID: PMID: 12383814; Medline: 22272540 Provider: OCLC.

12. Rosenfeld PJ, Moshfeghi AA, Puliafito CA. Optical coherence tomography findings after an intravitreal injection of bevacizumab (Avastin (R)) for neovascular age-related macular degeneration. Ophthal Surg Las Im. 2005;36(4):331-5. PubMed PMID: WOS:000232140900012.

13. Joeres S, Kaplowitz K, Brubaker JW, Updike PG, Collins AT, Walsh AC, Romano PW, Sadda SR. Quantitative comparison of optical coherence tomography after pegaptanib or bevacizumab in neovascular age-related macular degeneration. Ophthalmology. 2008;115(2):347-54. doi: 10.1016/j.ophtha.2007.03.082. PubMed PMID: WOS:000252840500020.

14. Witkin AJ, Vuong LN, Srinivasan VJ, Gorczynska I, Reichel E, Baumal CR, Rogers AH, Schuman JS, Fujimoto JG, Duker JS. High-speed ultrahigh resolution optical coherence tomography before and after ranibizumab for age-related macular degeneration. Ophthalmology. 2009;116(5):956-63. PubMed PMID: 19410953.

15. Fung AE, Lalwani GA, Rosenfeld PJ, Dubovy SR, Michels S, Feuer WJ, Puliafito CA, Davis JL, Flynn HW, Esquiabro M. An optical coherence tomography-guided, variable dosing regimen with intravitreal ranibizumab (lucentis) for neovascular age-related macular degeneration. Am J Ophthalmol. 2007;143(4):566-83. PubMed PMID: ISI:000245537800003.

16. Lalwani GA, Rosenfeld PJ, Fung AE, Dubovy SR, Michels S, Feuer W, Davis JL, Flynn HW, Jr., Esquiabro M. A variable-dosing regimen with intravitreal ranibizumab for neovascular age-related macular degeneration: year 2 of the PrONTO Study. Am J Ophthalmol. 2009;148(1):43-58 e1. PubMed PMID: 19376495.

17. Sayanagi K, Sharma S, Yamamoto T, Kaiser PK. Comparison of spectral-domain versus time-domain optical coherence tomography in management of age-related macular degeneration with ranibizumab. Ophthalmology. 2009;116(5):947-55. PubMed PMID: 19232732.

18. A randomized, placebo-controlled, clinical trial of high-dose supplementation with vitamins C and E, beta carotene, and zinc for age-related macular degeneration and vision loss: AREDS report no. 8. Arch Ophthalmol. 2001;119(10):1417-36. PubMed PMID: 11594942.

19. Sahu A, Kay BK, Lambris JD. Inhibition of human complement by a C3-binding peptide isolated from a phage-displayed random peptide library. J Immunol. 1996;157(2):884-91. PubMed PMID: 8752942.

20. Landa G, Butovsky O, Shoshani J, Schwartz M, Pollack A. Weekly vaccination with Copaxone (glatiramer acetate) as a potential therapy for dry age-related macular degeneration. Curr Eye Res. 2008;33(11):1011-3. PubMed PMID: 19085384.

21. Chen YL, Vuong LN, Liu J, Ho J, Srinivasan VJ, Gorczynska I, Witkin AJ, Duker JS, Schuman J, Fujimoto JG. Three-dimensional ultrahigh resolution optical coherence tomography imaging of age-related macular degeneration. Optics Express. 2009;17(5):4046-60. PubMed PMID: WOS:000264090900108.

22. Khanifar AA, Koreishi AF, Izatt JA, Toth CA. Drusen Ultrastructure Imaging with Spectral Domain Optical Coherence Tomography in Age-related Macular Degeneration. Ophthalmology. 2008;115(11):1883-90. doi: 10.1016/j.ophtha.2008.04.041. PubMed PMID: WOS:000260448900005.

23. Lujan BJ, Rosenfeld PJ, Gregori G, Wang FH, Knighton RW, Feuer WJ, Puliafito CA. Spectral domain optical coherence tomographic imaging of geographic atrophy. Ophthal Surg Las Im. 2008;39(4):S8-S14. PubMed PMID: WOS:000258283000002.

24. Schuman SG, Koreishi AF, Farsiu S, Jung SH, Izatt JA, Toth CA. Photoreceptor layer thinning over drusen in eyes with age-related macular degeneration imaged in vivo with spectral-domain optical coherence tomography. Ophthalmology. 2009;116(3):488-96 e2. Epub 2009/01/27. doi: 10.1016/j.ophtha.2008.10.006 S0161-6420(08)01026-9 [pii]. PubMed PMID: 19167082; PubMed Central PMCID: PMC2695995.

25. Gorczynska I, Srinivasan VJ, Vuong LN, Chen RW, Liu JJ, Reichel E, Wojtkowski M, Schuman JS, Duker JS, Fujimoto JG, Manassakorn A, Ishikawa H, Kim JS, Wollstein G, Bilonick RA, Kagemann L, Gabriele ML, Sung KR, Mumcuoglu T, Duker JS, Fujimoto JG, Schuman JS. Projection OCT fundus imaging for visualizing outer retinal pathology in non-exudative age related macular degeneration Comparison of optic disc margin identified by color disc photography and high-speed ultrahigh-resolution optical coherence tomography. The British journal of ophthalmology. 2008;28(1):28. PubMed PMID: 18662918.

26. Lujan BJ, Wang FH, Gregori G, Rosenfeld PJ, Knighton RW, Puliafito CA, Danis RP, Hubbard LD, Chang RT, Budenz DL, Seider MI, Knight O. Calibration of fundus images using spectral domain optical coherence tomography. Ophthal Surg Las Im. 2008;39(4):S15-S20. PubMed PMID: WOS:000258283000003.

27. Stopa M, Bower BA, Davies E, Izatt JA, Toth CA. Correlation of pathologic features in spectral domain optical coherence tomography with conventional retinal studies. Retina-J Ret Vit Dis. 2008;28(2):298-308. PubMed PMID: WOS:000253460800014.

28. Potsaid B, Gorczynska I, Srinivasan VJ, Chen YL, Jiang J, Cable A, Fujimoto JG. Ultrahigh speed Spectral/Fourier domain OCT ophthalmic imaging at 70,000 to 312,500 axial scans per second. Optics Express. 2008;16(19):15149-69. PubMed PMID: WOS:000259271900089.

29. Kraus MF, Potsaid B, Mayer MA, Bock R, Baumann B, Liu JJ, Hornegger J, Fujimoto JG. Motion correction in optical coherence tomography volumes on a per A-scan basis using orthogonal scan patterns. Biomedical optics express. 2012;3(6):1182-99. PubMed PMID: ISI:000304965700005.

30. Wojtkowski M, Leitgeb R, Kowalczyk A, Bajraszewski T, Fercher AF. In vivo human retinal imaging by Fourier domain optical coherence tomography. J Biomed Opt. 2002;7(3):457-63.

31. de Boer JF, Cense B, Park BH, Pierce MC, Tearney GJ, Bouma BE. Improved signal-to-noise ratio in spectral-domain compared with time-domain optical coherence tomography. Opt Lett. 2003;28(21):2067-9. PubMed PMID: 14587817.

32. Leitgeb R, Hitzenberger CK, Fercher AF. Performance of Fourier domain vs. time domain optical coherence tomography. Optics Express. 2003;11(8):889-94.

33. Leuschen JN, Schuman SG, Winter KP, McCall MN, Wong WT, Chew EY, Hwang T, Srivastava S, Sarin N, Clemons T, Harrington M, Toth CA. Spectral-Domain Optical Coherence Tomography

Characteristics of Intermediate Age-related Macular Degeneration. Ophthalmology. 2013;120(1):140-50. doi: DOI 10.1016/j.ophtha.2012.07.004. PubMed PMID: ISI:000313011700021.

34. Yehoshua Z, Wang F, Rosenfeld PJ, Penha FM, Feuer WJ, Gregori G. Natural history of drusen morphology in age-related macular degeneration using spectral domain optical coherence tomography. Ophthalmology. 2011;118(12):2434-41. Epub 2011/07/05. doi: 10.1016/j.ophtha.2011.05.008

S0161-6420(11)00432-5 [pii]. PubMed PMID: 21724264; PubMed Central PMCID: PMC3189426.

35. Sadigh S, Cideciyan AV, Sumaroka A, Huang WC, Luo X, Swider M, Steinberg JD, Stambolian D, Jacobson SG. Abnormal thickening as well as thinning of the photoreceptor layer in intermediate age-related macular degeneration. Invest Ophthalmol Vis Sci. 2013;54(3):1603-12. Epub 2013/01/31. doi: 10.1167/iovs.12-11286 [pii]. PubMed PMID: 23361506.

36. Ho J, Witkin AJ, Liu J, Chen YL, Fujimoto JG, Schuman JS, Duker JS. Documentation of Intraretinal Retinal Pigment Epithelium Migration via High-Speed Ultrahigh-Resolution Optical Coherence Tomography. Ophthalmology. 2011;118(4):687-93. doi: DOI 10.1016/j.ophtha.2010.08.010. PubMed PMID: ISI:000289075200012.

37. Christenbury JG, Folgar FA, O'Connell RV, Chiu SJ, Farsiu S, Toth CA, Ancill A-rEDS. Progression of Intermediate Age-related Macular Degeneration with Proliferation and Inner Retinal Migration of Hyperreflective Foci. Ophthalmology. 2013;120(5):1038-45. doi: DOI 10.1016/j.ophtha.2012.10.018. PubMed PMID: ISI:000318683400023.

38. Fleckenstein M, Issa PC, Helb HM, Schmitz-Valckenberg S, Finger RP, Scholl HPN, Loeffler KU, Holz FG. High-resolution spectral domain-OCT imaging in geographic atrophy associated with age-related macular degeneration. Investigative Ophthalmology & Visual Science. 2008;49(9):4137-44. doi: 10.1167/iovs.08-1967. PubMed PMID: WOS:000258896500053.

39. Fleckenstein M, Schmitz-Valckenberg S, Adrion C, Kramer I, Eter N, Helb HM, Brinkmann CK, Issa PC, Mansmann U, Holz FG. Tracking Progression with Spectral-Domain Optical Coherence Tomography in Geographic Atrophy Caused by Age-Related Macular Degeneration. Investigative Ophthalmology & Visual Science. 2010;51(8):3846-52. doi: Doi 10.1167/Iovs.09-4533. PubMed PMID: ISI:000280194100005.

40. Fleckenstein M, Schmitz-Valckenberg S, Martens C, Kosanetzky S, Brinkmann CK, Hageman GS, Holz FG. Fundus Autofluorescence and Spectral-Domain Optical Coherence Tomography Characteristics in a Rapidly Progressing Form of Geographic Atrophy. Investigative Ophthalmology & Visual Science. 2011;52(6):3761-6. doi: Doi 10.1167/Iovs.10-7021. PubMed PMID: ISI:000293335400046.

41. Moussa K, Lee JY, Stinnett SS, Jaffe GJ. Spectral Domain Optical Coherence Tomography-Determined Morphologic Predictors of Age-Related Macular Degeneration-Associated Geographic Atrophy Progression. RETINA. 2013;Publish Ahead of Print:10.1097/IAE.0b013e31828d6052.

42. Yehoshua Z, Rosenfeld PJ, Gregori G, Feuer WJ, Falcao M, Lujan BJ, Puliafito C. Progression of geographic atrophy in age-related macular degeneration imaged with spectral domain optical coherence tomography. Ophthalmology. 2011;118(4):679-86. Epub 2010/11/03. doi: 10.1016/j.ophtha.2010.08.018

S0161-6420(10)00866-3 [pii]. PubMed PMID: 21035861; PubMed Central PMCID: PMC3070862.

43. Portella Nunes R, Gregori G, Stetson PF, Yehoshua Z, Moshfegui AA, Feuer WJ, Rosenfeld PJ. Progression of Geographic Atrophy Predicted by Outer Photoreceptor Disruption Identified by SD-OCT En Face Imaging. 2013 ARVO/ISIE Imaging Conference; 5/4/2013; Seattle, WA2013. p. 50.

44. Wu Z, Ayton LN, Guymer RH, Luu CD. Relationship between the second reflective band on optical coherence tomography and multifocal electroretinography in age-related macular degeneration. Invest Ophthalmol Vis Sci. 2013;54(4):2800-6. Epub 2013/03/28. doi: 10.1167/iovs.13-11613 [pii]. PubMed PMID: 23532524.

45. Zweifel SA, Spaide RF, Curcio CA, Malek G, Imamura Y. Reticular Pseudodrusen Are Subretinal Drusenoid Deposits. Ophthalmology. 2010;117(2):303-U139. doi: DOI 10.1016/j.ophtha.2009.07.014. PubMed PMID: ISI:000274530300017.

46. Arnold JJ, Quaranta M, Soubrane G, Sarks SH, Coscas G. Indocyanine green angiography of drusen. Am J Ophthalmol. 1997;124(3):344-56. Epub 1998/01/24. PubMed PMID: 9439360.

47. Cohen SY, Dubois L, Tadayoni R, Delahaye-Mazza C, Debibie C, Quentel G. Prevalence of reticular pseudodrusen in age-related macular degeneration with newly diagnosed choroidal neovascularisation. The British journal of ophthalmology. 2007;91(3):354-9. Epub 2006/09/16. doi: bjo.2006.101022 [pii] 10.1136/bjo.2006.101022. PubMed PMID: 16973663; PubMed Central PMCID: PMC1857688.

48. Lujan BJ, Roorda A, Knighton RW, Carroll J. Revealing Henle's Fiber Layer Using Spectral Domain Optical Coherence Tomography. Investigative Ophthalmology & Visual Science. 2011;52(3):1486-92. doi: Doi 10.1167/Iovs.10-5946. PubMed PMID: ISI:000288965300034.

49. Otani T, Yamaguchi Y, Kishi S. Improved Visualization of Henle Fiber Layer by Changing the Measurement Beam Angle on Optical Coherence Tomography. Retina-J Ret Vit Dis. 2011;31(3):497-501. doi: Doi 10.1097/Iae.0b013e3181ed8dae. PubMed PMID: ISI:000287472400010.

50. Curcio CA, Johnson M, Rudolf M, Huang JD. The oil spill in ageing Bruch membrane. Brit J Ophthalmol. 2011;95(12):1638-45. doi: DOI 10.1136/bjophthalmol-2011-300344. PubMed PMID: ISI:000297261700005.

51. Ryan SJ. Retina. 5th ed. Oxford: Saunders Elsevier; 2013.

52. Spaide RF, Curcio CA. Anatomical Correlates to the Bands Seen in the Outer Retina by Optical Coherence Tomography Literature Review and Model. Retina-J Ret Vit Dis. 2011;31(8):1609-19. PubMed PMID: ISI:000294456100021.

CHAPTER 5

Swept-Source / Fourier Domain Optical Coherence Tomography

5.1 Introduction

Fourier domain detection schemes have enabled a breakthrough in OCT imaging sensitivity and speed. Performance advantages of Fourier domain OCT were first recognized by several independent studies and has since attracted considerable attention.[1-4] Although nowadays standard clinical ophthalmic OCT instruments are typically built with spectrometers (spectral / Fourier domain OCT; SD-OCT), a new generation of OCT systems based on wavelength tunable light sources (swept laser sources) have been developed.[3, 5-7]

Swept-source / Fourier domain OCT (SS-OCT) uses high speed balanced point detectors instead of a line scan camera and spectrometer so that the detection losses are reduced compared with SD-OCT as a result of the higher detection efficiency of photodetectors. In addition, less signal roll-off with imaging depth is observed in SS-OCT instruments due to the coherence properties of tunable lasers and the ability to detect high frequency signals in state-of-the-art broad bandwidth acquisition systems. Moreover, ophthalmic SS-OCT systems image at wavelengths centered at 1 μm, longer than traditionally used wavelengths at 840 nm, allow for better penetration of light in scattering tissues. These features enable outstanding OCT performance, achieving high imaging speeds and deep tissue imaging depths, which consequently improve the functionality of SS-OCT instruments and broaden the spectrum of ophthalmic applications.

5.2 Small Animal Swept-Source / Fourier Domain OCT system

An ultrahigh speed swept-source / Fourier domain OCT instrument was built for small animal imaging (Figure 5.1A). A short external cavity, tunable light source (Axsun Technologies, Inc.) centered at 1044 nm which had a 3-dB bandwidth of 103 nm and a 10-dB bandwidth of 111 nm was used (Figure 5.1B). The axial scan rate of the OCT system was 100 kHz, set by the sweep rate of the laser. Light from the laser was split into a single pass reference arm and a pre-objective scanning sample arm where the galvanometric scanners are placed in the back focal plane of the objective lenses. Returning light from the reference and sample arms was combined in a second fiber coupler and the interferometric signal was detected using a low distortion 330 MHz dual balanced photodetector receiver (prototype; Thorlabs, Inc.). The signal from the photodetector was digitized by a high speed 8 bit analog-to-digital converter at 1 GSPS (ATS9870; Alazar Technologies, Inc.). Different scan lenses in the sample arm were

used to provide different transverse spot sizes and depths of focus. A long working distance infrared microscope objective (M Plan NIR 5X; Mitutoyo Corp.) was used for retinal imaging. The transverse spot size was ~12 μm full width at half maximum (FWHM) measured in air with a beam profiling camera and the incident power was 1.6 mW. For anterior eye and full eye length imaging as well as for posterior eye imaging, a 75 mm focal length achromatic lens was used. The transverse spot size was ~21 μm FWHM in air and the incident power was 2.5 mW. Unlike human eye imaging, a telecentric scanning interface was used for both anterior segment and retinal imaging of the rodent eye. A #1.5 coverslip and index matching gel (Goniosol) was used over the corneal during the retinal and posterior eye imaging procedures. An LED light stimulus was placed adjacent to the sample arm interface without blocking the OCT beam. The measured axial resolution of the system was 6 μm in tissue. The measured sensitivity of the system was 102 dB with a Nyquist limited depth range of 8.7 mm in tissue where the -6-dB roll-off depth was at 2.5 mm in tissue and the -20-dB roll-off depth was at 5.3 mm in tissue. The sensitivity roll-off was limited by the bandwidth of the balanced photodetector and finite light source coherence length (the roll-off from the coherence length itself introduces a -6-dB sensitivity drop at 6 mm in air).

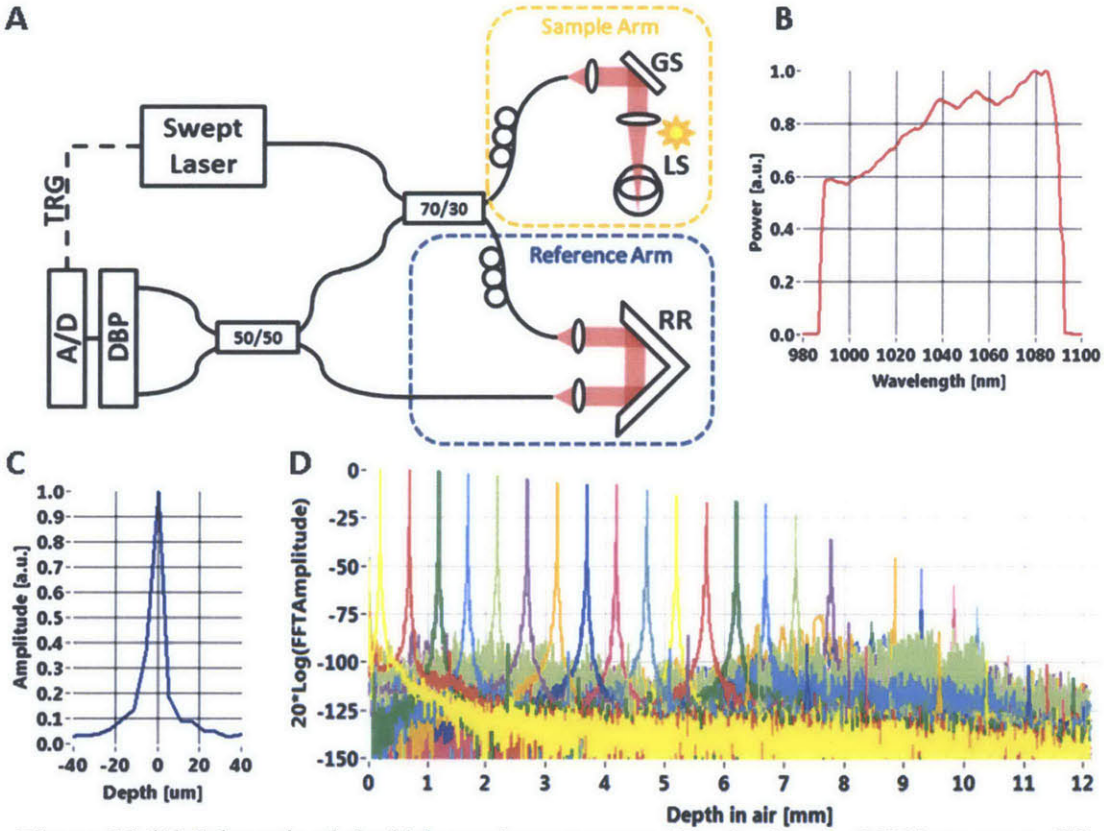

Figure 5.1 (A) Schematic of ultrahigh speed swept-source / Fourier domain OCT instrument. GS – galvanometric scanners, RR – retroreflector, LS – LED light stimulus, DBP – dual balanced photodetector, A/D – analog-to-digital converter, TRG – trigger signal. (B) Spectrum of the light source. (C) Point spread function showing axial resolution. (D) Sensitivity roll-off.[8]

Sprague-Dawley rats and C57BL/6 mice were used to demonstrate the imaging capability of the OCT system. Animals were anesthetized intraperitoneally with ketamine (40-80 mg/kg body weight) and xylazine (5-10 mg/kg body weight) for all structural imaging studies. During anterior eye and full eye length imaging, artificial tear drops were applied to prevent cornea dehydration. To perform retinal and posterior eye imaging, eyes were dilated with topically applied tropicamide (1%) drops, and a thin microscope coverslip was placed on the cornea with Hydroxypropyl methylcellulose (Goniosol, 2.5%) to remove corneal refraction and preserve corneal hydration. To perform functional imaging studies, imaging the pupillary reflex, animals were anesthetized intraperitoneally by a cocktail containing ketamine (40 mg/kg body weight), xylazine (3 mg/kg body weight), and acepromazine (1.5 mg/kg body weight). These studies were in compliance with the guidelines of the ARVO Statement for the Use of Animals in Ophthalmic and Vision Research, and performed under a protocol approved by the MIT Committee on Animal Care. After anesthetization, the animal was placed in a comfortable mounting tube fixed on a height and tilt adjustable stage pivoted about the animal's eye.

OCT cross-sectional previews along with a real-time OCT en face fundus image were used for alignment. For retinal imaging, six raster scans with orthogonal fast scan axis orientation (horizontal and vertical) each consisting of 700 × 700 axial scans requiring an acquisition time of ~5 seconds for each raster (~30 seconds total) were acquired. The six volumetric datasets were then registered using motion correction software and merged. For anterior eye and full eye length imaging, two raster scans with orthogonal fast scan axes (horizontal and vertical) consisting of 500 × 500 axial scans requiring an acquisition time of <3 seconds each were acquired, motion corrected and merged. For posterior eye and Doppler imaging, six orthogonal 500 × 500 axial scan raster scans were acquired, motion corrected, and merged, where each scan was acquired in <3 seconds. For high speed dynamic volumetric OCT imaging, repeated raster scans with 100 × 100 axial scans were taken in sequence to achieve ~10 volumes per second. The high speed repeated volumes were not motion corrected.

Doppler OCT is a functional extension of OCT which provides velocity and flow information. In Fourier domain OCT, the complex OCT spectral data is processed and the phase information is used for velocity and flow calculations in Doppler OCT.[9-13] A simple phase subtraction of neighboring oversampled OCT axial scans generates quantitative Doppler OCT measurements which was used to visualize the vasculature in eyes

$$v_z(z)=\frac{\lambda_0}{4\pi n} f\left[\varphi_{i+1}(z)-\varphi_i(z)\right] \tag{5.1}$$

where λ_0 is the center wavelength of the light, n is the refractive index, f is the sweep rate, and $\varphi_i(z)$ is the phase profile of the i-th axial scan after Fourier transformation. The maximum detectable velocity before

phase wrapping, determined by the imaging speed, is ±20 mm/s in tissue. In theory, the minimum detectable axial velocity is determined by the phase stability of the light source, and was measured to be 1.8 mrad. In practice, the minimum measurable axial velocity in tissue is limited by the phase decorrelation associated with trigger jitter and scanning the beam.[13] After applying a phase compensation algorithm where bulk motion was calculated and removed using a histogram-based method[11], the standard deviation of phase differences between successive sweeps over a mirror was measured to be 0.11 rad, corresponding to a minimum measurable axial velocity of 0.7 mm/s in tissue.

Although the imaging was performed with the animals under anesthesia, motion artifacts persist from breathing and heartbeat. Motion during the acquisition of volumetric OCT data distorts the data and is a source of error in quantitative measurements. A registration motion-correction algorithm was recently developed for orthogonally scanned volumetric OCT data.[14] Motion correction is performed by estimating dense displacement fields, which describe the motion of each A-scan, for each input volume and using the time structure of the acquisition process as a constraint. After optimizing a global objective function, the displacement fields are estimated for each volume to correct for motion, and then a single volume is constructed by merging each motion-corrected volume. Motion-corrected volumes do not show visible motion artifacts and a merged registered volume has improved signal quality. The motion corrected, merged volumetric data more accurately represents structure and morphology than individual volumes which can have motion artifacts.

For the pupil response experiments, a white light LED stimulus with ~800 cd/cm^2 luminance was used. The LED light source was placed adjacent to the OCT beam without blocking the OCT scan. Two stimulus protocols were used: a continuous >5 second stimulus and a short ~1 second flash stimulus. The stimulus was activated during OCT data acquisition of repeated raster scans.

5.2.1 Three-Dimensional Retinal Imaging in Unpigmented Rat Eye and Pigmented Mouse Eye

Three-dimensional (3D) volumetric OCT imaging of the unpigmented Sprague-Dawley rat retina and pigmented C57BL/6 mouse retina is demonstrated in Figures 5.2 and 5.3, respectively. The animals were anesthetized so that measurement time is not limited by blinking or motion, as is the case for human ophthalmic imaging. A coverslip was placed on the cornea to remove the refractive power of the air-corneal interface, focusing and scanning the OCT beam directly on the retina through the weaker refraction from the lens. Six orthogonally scanned 700 × 700 axial scan datasets were registered and merged.

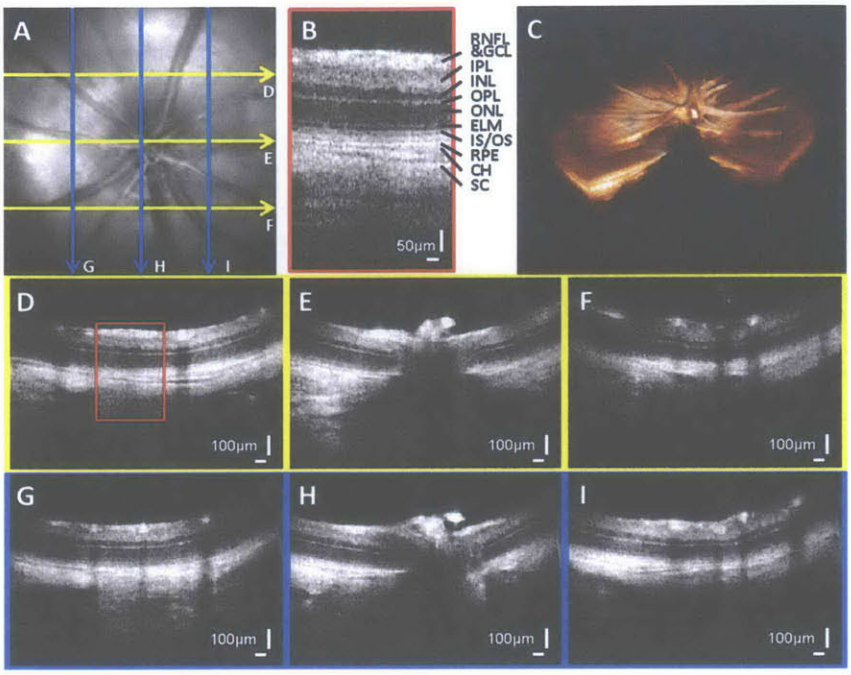

Figure 5.2 Imaging of the unpigmented Sprague-Dawley rat retina. Registered and merged OCT dataset generated from 6 orthogonally scanned OCT datasets. (700 × 700 axial scans over a 2.4 mm × 2.4 mm region) (A) OCT fundus view. (B) Retinal layers visualized in the cropped, enlarged OCT image. (C) 3D rendering. (D, E, F) OCT images in the X direction. (G, H, I) OCT images in the Y direction.[8]

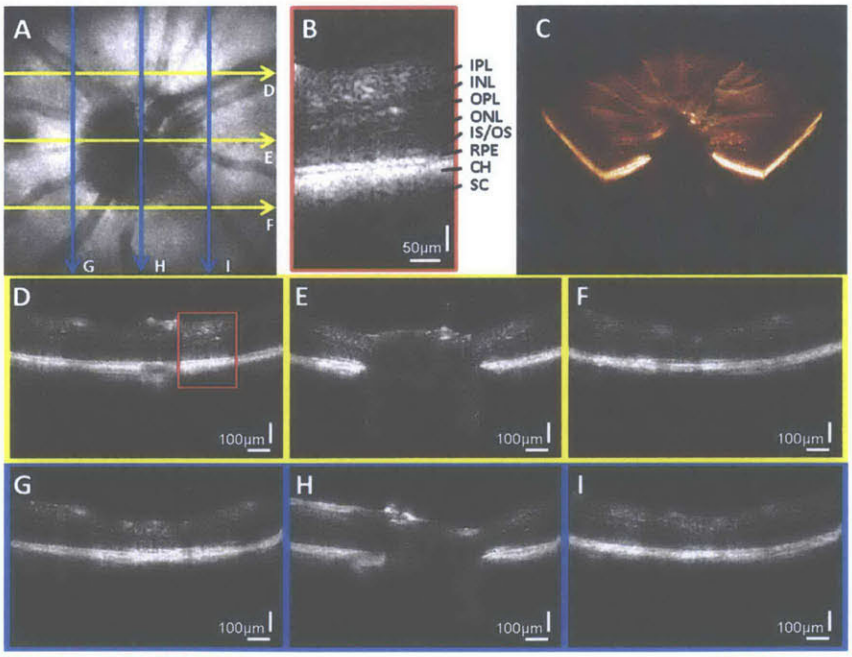

Figure 5.3 Imaging of the pigmented C57BL/6 mouse retina. Registered and merged dataset generated from 6 orthogonally scanned OCT datasets. (700 × 700 axial scans over a 1.2 mm × 1.2 mm region) (A) OCT fundus view. (B) Retinal layers shown in the cropped, enlarged OCT image (C) 3D rendering. (D, E. F) OCT images in the X direction. (G, H, I) OCT images in the Y direction.[8]

Scans were performed over a 1.2×1.2 mm^2 area over the mouse eye and a 2.4×2.4 mm^2 area over the rat eye. Each dataset is acquired in ~5 seconds. An OCT fundus view is generated by axially summing the merged OCT dataset (Figure 5.2A and Figure 5.3A). Cross-sectional images from the merged dataset enable visualization of major retinal layers including the inner plexiform layer (IPL), inner nuclear layer (INL), outer plexiform layer (OPL), outer nuclear layer (ONL), photoreceptor inner segment and outer segment (IS/OS) junction, retinal pigment epithelium (RPE), choroid (CH), and sclera (SC) in both the Sprague-Dawley rat and C57BL/6 mouse eyes (Figure 5.2B and Figure 5.3B).

In addition, the retinal nerve fiber layer (RNFL), ganglion cell layer (GCL), and external limiting membrane (ELM) are visible in the Sprague-Dawley rat (Figure 5.2B). The smaller size of the mouse retina limited the visibility of smaller features. Isotropic transverse sampling of the retina allows for volumetric rendering that shows the structural details of the retina in 3D (Figure 5.2C and Figure 5.3C). Since the 3D OCT volumetric dataset is motion corrected, we can extract cross-sectional images in any position and direction without motion artifacts (Figure 5.2D-I and Figure 5.3D-I). Notice that neither the cross-sectional images visualized in the horizontal and vertical direction nor the 3D volumetric rendering exhibit motion artifacts.

5.2.2 Anterior Eye and Full Eye Length Imaging in Rat and Mouse Eyes

The long imaging range of swept-source / Fourier domain OCT also enabled 3D anterior eye and full eye length OCT imaging in the rat and mouse eyes using sample arm optics with a larger transverse spot size and longer depth of field. Anterior eye and full eye length imaging provides 3D information on the anterior chamber and crystalline lens structure as well as biometric information on the full eye length. The animal eye is placed directly in front of the scan lens under anesthesia and after dilation. Two orthogonally scanned 500×500 axial scan datasets were registered and merged.

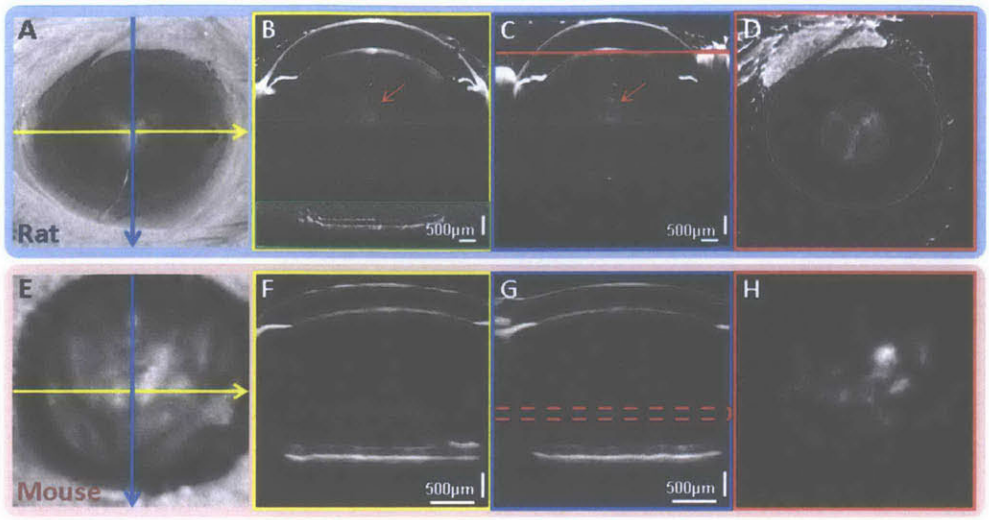

Figure 5.4 Anterior eye and full eye length OCT imaging in the Sprague-Dawley rat and C57BL/6 mouse eye. (A, E) En face view of the volumetric dataset registered and merged from two orthogonally scanned 500 × 500 axial scan volumes. The rat eye was scanned over a 7 mm × 7 mm area. The mouse eye was scanned over a 2.6 mm × 2.6 mm area. (B, C, F, G) Cross-sectional images in the horizontal and vertical direction generated from averaging neighboring 5 frames. The red arrows point to the rat lens nucleus. The green box is a region in the image where the contrast was adjusted to better visualize signal from the rat retina. (D) Extracted en face cross section at the red line position showing the Y-shaped suture pattern in the rat lens anterior. (H) Summed en face view over the rat lens posterior as indicated in the red dotted box, which shows the pattern of opacities in the mouse lens.[8]

The scans were performed over a 2.6 × 2.6 mm^2 area of the mouse eye and a 7 × 7 mm^2 area of the rat eye. Figure 5.4A is an OCT en face view of a Sprague-Dawley rat eye. The Y-shaped shadow in the center of the eye is the lens suture pattern on the anterior crystalline lens which can be visualized when an en face cross section at appropriate depth is extracted from the volume (Figure 5.4D). Cross-sectional images in Figures 5.4B and 5.4C reveal detailed structures of the cornea, iris, and lens, as well as visible signal from the vitreous and retina. A thin liquid film from the eye drops is visible on the cornea of the rat eye. In addition to lens sutures, the nucleus is visible in the cross sectional images.

Figure 5.4E is an OCT en face view of a C57BL/6 mouse eye. This particular mouse eye exhibits lens opacities which can be visualized by summing en face pixels near the posterior lens surface, as shown in Figure 5.4H. Cross-sectional images in Figures 5.4F and 5.4G reveal detailed structures of the cornea, iris, lens, vitreous and retina. The 3D dataset illustrates the larger lens volume compared to vitreous volume in the rat and mouse eyes. The irises and pupils are dilated. Ocular biometry

measurements of the eyes can be performed after refraction correcting the OCT images in the axial direction.

5.2.3 Three-Dimensional Posterior Eye Imaging in Unpigmented Rat Eye

In order to better image the posterior eye of the unpigmented Sprague-Dawley rat, the focus was advanced towards the posterior eye and a coverslip was placed on the eye to minimize corneal refraction. Although the larger transverse spot size decreases the transverse resolution compared to the retinal imaging mode described in section 5.2.1, the longer focal depth and long imaging range enables visualization of the posterior lens, vitreous and retina. Figure 5.5 is a posterior eye dataset generated from registering and merging six orthogonally scanned volumes of 500 × 500 A-scans each. The scans were performed over a 2.6 × 2.6 mm^2 area of the rat eye. The dataset shows the posterior lens surface, where the Y-shaped lens sutures can be visualized in an inverted orientation as seen on the en face image in Figure 5.5B. The hyaloid vessel as well as floaters can be seen in the vitreous. Retinal layers can be clearly visualized in cross-sectional images (Figures 5.5C-D). The deep penetration of 1050 nm wavelength light allows visualization of tissue structure in the choroid and sclera. The fundus image shows that major retinal blood vessels radiate from the center of the optic disk.

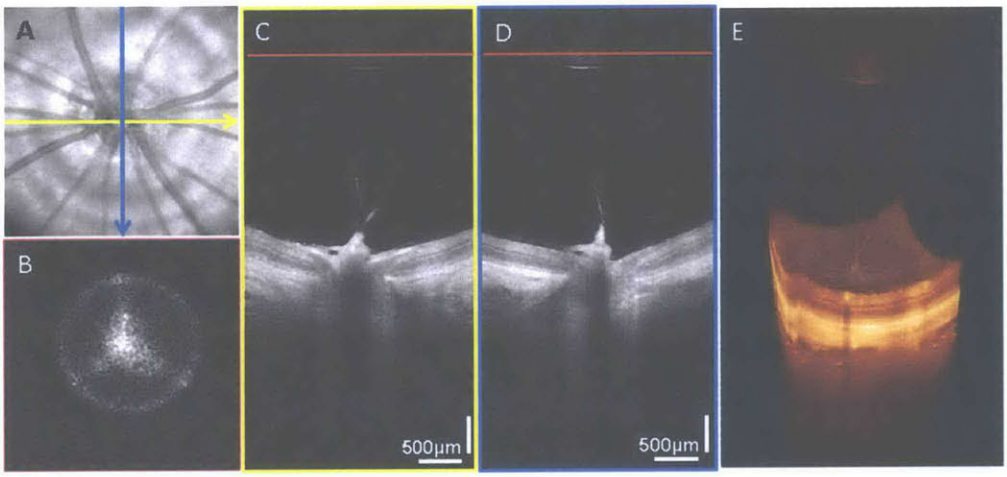

Figure 5.5 Posterior eye imaging of the unpigmented Sprague-Dawley rat including retina, vitreous, and posterior lens. (A) OCT en face view of the registered and merged dataset from six orthogonally scanned 500 × 500 axial scan volumes. Imaging of the rat posterior eye was performed over a 2.6 mm × 2.6 mm area. (B) En face cross section showing inverted Y-shaped posterior lens sutures. (C, D) Cross sections from the registered dataset showing the retina, hyaloid vessel and posterior part of the crystalline lens. The red line indicates the depth position of the en face cross section. (E) 3D rendering of the dataset.[8]

5.2.4 Three-Dimensional Doppler Imaging in Unpigmented Rat Eye

Doppler OCT imaging of the Sprague-Dawley rat was performed using the phase difference of neighboring axial scans in the six orthogonally scanned 500 x 500 axial scan datasets acquired in the posterior eye imaging mode described in section 5.2.3. The larger spot size decreases the number of samples required to obtain Doppler OCT information over the same scan area compared to the retinal imaging mode in section 5.2.1. The Doppler OCT datasets were merged using motion correction information (displacement fields) from the registered intensity images (Figure 5.6). Intensity and Doppler OCT cross-sections present complementary information on the structure and function of the retina. When the Doppler image is overlaid on its structural counterpart (Figures 5.6B-D), the combined images may provide insight into the relationship between structural and functional changes of the retina in pathology and disease progression. A 3D rendering of the vasculature in the retina and choroid is shown in Figure 5.6E. Two types of vessels can be distinguished in the retina by looking at the direction of blood flow. When blood moves towards the OCT beam, the Doppler shift is positive, as indicated with the red (warm) color. The retinal arteries are oriented in this direction and are hence visualized in red. On the other hand, blood returning from retinal tissue produces negative Doppler shifts. Consequently, retinal veins are visualized in a blue (cold) color. In the rat retina, arterial and venous vascular systems can overlap one another. Since Doppler OCT can only measure flow velocities in the axial direction, the vessels appear to be discontinuous or disconnected when they are perpendicular to the OCT beam. In addition to retinal vessels and the central retinal artery, some choroidal vessels, as well as long posterior ciliary arteries are also visible owing to the deep penetration of 1050 nm wavelength light.

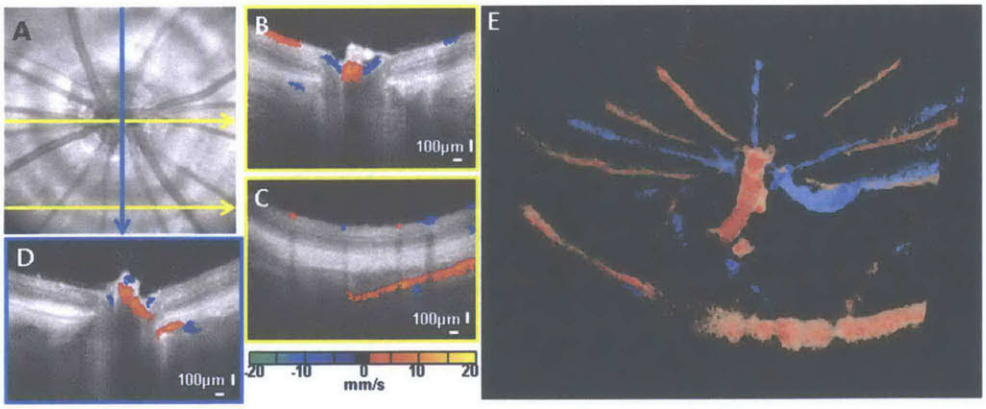

Figure 5.6 Doppler OCT imaging in a unpigmented Sprague-Dawley rat retina. Doppler OCT analysis was performed using posterior eye OCT data (6 orthogonally scanned 500 × 500 axial scan OCT datasets over a 2.6 mm × 2.6 mm region). The 6 Doppler OCT volumes were merged using the displacement fields from registered structural OCT data. (A) OCT fundus image. (B, C, D) OCT color Doppler images with blood flow information overlaid on structural images. (E) 3D Doppler OCT angiography.[8]

5.2.5 Four-Dimensional Imaging of Pupillary Response in Rat and Mouse eyes

High speed OCT imaging enables time resolved volumetric four-dimensional (4D) imaging of the dynamic responses of the eye to stimulus. A Sprague-Dawley rat and a C57BL/6 mouse were sedated lightly to preserve pupillary responses. Figures 5.7 and 5.8 are demonstrations of 4D imaging of the papillary response in the rat and mouse eye. OCT volumes of 100 × 100 axial scans were acquired at ~10 volumes per second for 5 seconds. Scans were performed over a 7 × 7 mm^2 area of the rat eye and a 3.5 × 3.5 mm^2 area of the mouse eye. All volumes were scanned with a horizontal fast scan axis and motion correction was not performed. A continuous stimulus and a short ~1 second flash stimulus were applied to both the rat and mouse eyes. 3D dynamics can be visualized and quantitative measurements of the pupil area can be obtained. Despite the high volume rate of the acquisition, motion is visible in the datasets predominantly due to breathing and heartbeat. As more light enters the eye, the iris responds by rapid contraction, which leads to the decrease in pupil diameter. When the stimulus is turned off, the iris muscles slowly relax. The pupil area from each acquired volume was measured.

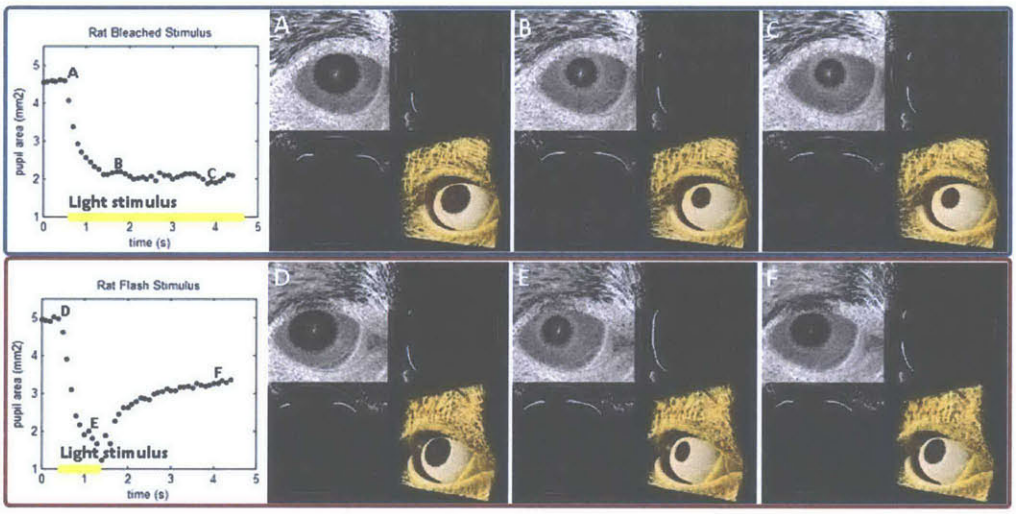

Figure 5.7 Dynamic response of the Sprague-Dawley rat eye to long and short duration light stimulus. Volumetric imaging was performed at ~10 volumes per second. Each volume consists of 100 × 100 axial scans over a 7 mm × 7 mm area. Changes of the pupil area before, during, and after light stimulus are shown in plot. (A, B, C) (D, E, F) Selected time points illustrate the structural changes in the eye over time. An OCT en face view, central orthogonal cross-sections, as well as a 3D rendering are shown for each time point.[8]

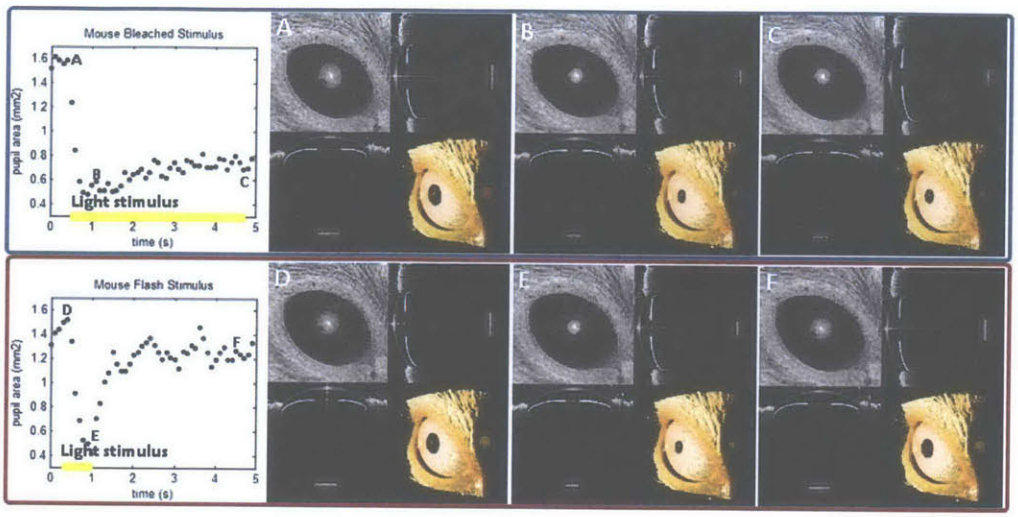

Figure 5.8 Dynamic response of the C57BL/6 mouse eye to long and short duration light stimulus. Volumetric imaging was performed at ~10 volumes per second. Each volume consists of 100 × 100 axial scans over a 3.5 mm × 3.5 mm area. Changes of the pupil area before, during, and after light stimulus are shown in plot. (A, B, C) (D, E, F) Selected time points illustrate the structural changes in the eye over time. An OCT en face view, central orthogonal cross-sections, as well as a 3D rendering are shown for each time point.[8]

5.2.6 Discussion

Structural and Doppler angiographic imaging of the rodent eye was demonstrated using a novel ultrahigh speed swept-source / Fourier domain OCT instrument. The instrument was architected based on a recently developed SS-OCT system for high speed imaging in human eyes at long wavelengths.[15] The long imaging range and high imaging speed of SS-OCT, along with the deep penetration into tissue of 1050 nm wavelength light enables 3D volumetric imaging of the retina and posterior eye, as well as the anterior eye and full eye length in rodent eyes. A registration algorithm was applied to remove motion artifacts and merge multiple datasets for enhanced visualization.

OCT has been widely used for in vivo retinal imaging of rodent models. This chapter presents motion-corrected 3D OCT images in rat and mouse eyes using SS-OCT. Although current 1050 nm wavelength SS-OCT technology has limited resolution compared to 850 nm SD-OCT, the improved tissue penetration provides additional information in the choroid and sclera. Motion correction enables large volumes to be acquired without motion artifacts and merging improves image quality. Although visibility of features is poorer in the mouse compared with the rat, for retinal imaging, major retinal layers including the retinal nerve fiber layer (RNFL), ganglion cell layer (GCL), inner plexiform layer (IPL), inner nuclear layer (INL), outer plexiform layer (OPL), outer nuclear layer (ONL), external limiting membrane (ELM), photoreceptor inner segment and outer segment (IS/OS) junction, retinal pigment

epithelium (RPE), choroid (CH), and sclera (SC) can be resolved. Doppler OCT provides motion contrast highlighting the retinal vasculature and enables differentiating arteries and veins. Quantitative information of blood flow velocity can also be obtained. No obvious artifacts due to pulsatility remain in the motion-corrected and merged Doppler OCT data which was obtained from multiple orthogonally scanned volumes. The deep penetration into tissue allowed Doppler OCT imaging of the long posterior ciliary arteries.

The main advantages of SS-OCT compared to SD-OCT are increased sensitivities, imaging speed, and imaging range. For rodent eye imaging, the high speeds and extended range enable 3D imaging of the retina, posterior eye, anterior eye and full eye length. Combined with image registration motion correction, we demonstrated 3D in vivo SS-OCT full eye length volumetric imaging while preserving corneal, iris, lens, and retinal topography in both rats and mice. This promises to allow quantitative measurements tracking the changes in morphogenesis and pathological processes in the same animal eye over time.

SS-OCT at 1050 nm may provide new means for in vivo rodent hyaloid vessel and lens development studies. In our results, we were able visualize the hyaloid vessel, lens nucleus, lens opacities, and lens suture patterns. Comparing Figure 5.4D with Figure 5.5B, it can be seen that suture patterns in the anterior and posterior pole of the crystalline lens have opposite orientations. Lens fibers make up the bulk of the lens and form lens suture patterns which produce an upright 'Y' pattern anteriorly and an inverted 'Y' pattern posteriorly. This was the first demonstration of visualizing the lens suture pattern in the rat eye using OCT. In the mouse eye, we could observe lens opacities possibly induced by ketamine-xylazine anesthesia (Figure 4E) suggesting that cataract characterization may be possible.[16] Meanwhile in the mouse full eye length image, the retina remained highly visible despite the lens opacities. This also suggests that the reduced scattering of 1050 nm wavelength light will be useful for OCT retinal imaging even in rodent eyes with cataracts.

For mouse eye imaging and biometry measurements, Wang et al. [17] has described a 28 kHz SS-OCT imaging system with a center wavelength of 1056 nm and 70 nm scanning bandwidth. A subsequent paper demonstrated the ability to measure the heritability of ocular component dimensions in mice. These papers reported the ability to acquire ~17.6 μm axial resolution cross-sectional data in air using a fast Dispersion Encoded Full Range (DEFR) algorithm over a depth range of ±5 mm in air with -18-dB roll-off at ±3 mm in air where conjugate artifacts compromise the alignment of the imaging system. By taking advantage of the longer imaging range with -20-dB roll-off at 5.3 mm in tissue, the higher 6 μm axial resolution in tissue, the 3.6 times faster 100 kHz imaging speed, and the registration motion-

correction algorithm, our results provide motion-corrected 3D OCT data of the full eye length in not only the shorter mouse eye, but also the longer rat eye. Three-dimensional motion-corrected data can be refraction corrected and processed for more accurate biometry measurements unaffected by alignment errors or motion artifacts when acquiring only a single cross-sectional OCT image. Although the limited detector bandwidth along with the limited coherence length of the swept-source laser used in this study affected signal in the rat retina during full eye length imaging (Figure 4B Figure 4C), next generation swept lasers with ultralong coherence lengths will have virtually no signal roll-off within the range needed for rodent full eye length imaging.[18]

We also performed the first demonstration of 4D time resolved volumetric OCT imaging of the mouse and rat full eye length. 4D OCT dynamic imaging could provide spatial-temporal information of 3D volumetric datasets for functional imaging studies. A simple demonstration of pupillometry is shown in this study. In addition to pupil area, 4D OCT provides information of the iris structure. The contraction of the iris was visualized in 3D. Other 4D OCT applications include imaging of structural and blood flow responses to intraocular pressure[19, 20] and the dynamics of neurovascular function in the eye[21, 22].

To conclude, SS-OCT is a powerful imaging technique providing comprehensive 3D information on the rodent eye including motion-corrected posterior eye, anterior eye and full eye length imaging, retinal imaging with Doppler OCT angiography, as well as 4D dynamic imaging of functional responses of the eye. While standard excisional biopsy and histology require enucleating the eye, OCT can perform repeated, noninvasive in situ imaging and quantitative measurements of the rodent retina. Therefore, SS-OCT technology for rodent eye imaging is a potentially useful tool for in vivo imaging of disease phenotypes such as corneal opacity, uveitis, keratitis, glaucoma, cataract, retinoblastoma, retinal degeneration, retinal vascular disease and myopia.

5.3 Clinical Swept-Source / Fourier Domain OCT Systems

A total of three clinical swept-source / Fourier domain OCT systems were built and deployed at our collaborator's clinical sites. In collaboration with Dr. Benjamin Potsaid, Dr. Bernhard Baumann, Martin Kraus, a retinal imaging system was built for Dr. David Huang's group at the Oregon Health Science University in Portland, OR. In collaboration with Dr. Irenuesz Grulkowski and Chen Lu, two systems with retinal and anterior imaging capabilities were built for Dr. Jay Duker's group at the New England Eye Center and Dr. Joel Schuman's group at the University of Pittsburgh Eye Center.

These systems were developed based on Dr. Benjamin Potsaid's initial work.[15] Figure 5.9 shows the schematic of the clinical swept-source / Fourier domain OCT systems. The 1050 nm Axsun laser runs at a 100 kHz sweep rate, with a tuning bandwidth of 105nm. The axial resolution is 6.5μm. The maximum incident power on the eye is 1.9 mW, in accordance to the ANSI safety limits. The imaging depth range in tissue is 2.8 mm with the optical clock and 3.6 with the 400 MHz internal clock. The measured sensitivity is 105 dB. Figure 5.10 are photographs of the deployed systems at their clinical sites.

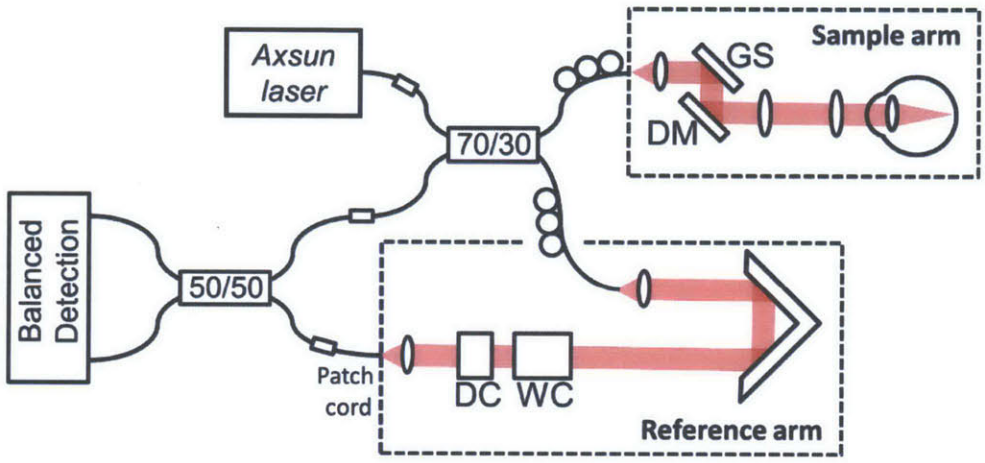

Figure 5.9 Schematic of swept-source / Fourier domain OCT system. GS – galvo scanners, DM – dichoric mirror, DC – dispersion compensation glass, WC – water cell.

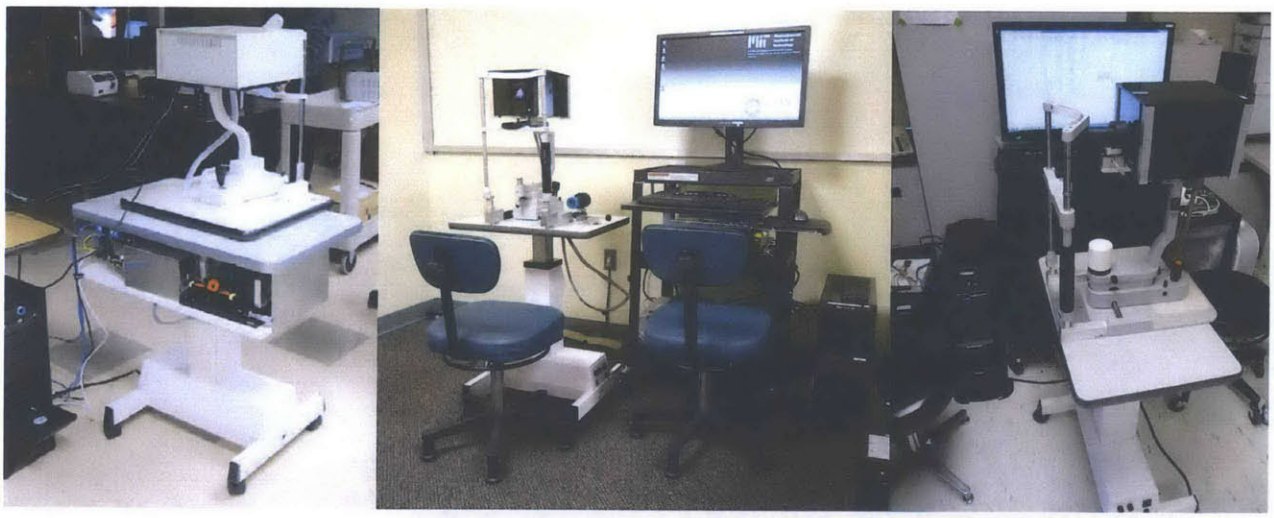

Figure 5.10 Clinical swept-source / Fourier domain OCT systems. (left) OHSU system with all optics mounted on the ophthalmic table. This design has the advantage that the motion of the optical fiber to the sample arm is kept to a minimum, keeping unwanted polarization changes due to system position movement to a minimum. (center) UPMC system with posterior and anterior eye imaging capabilities. The ocular lens on the patient interface is removed in this photo for the anterior imaging mode. (right) NEEC system with the same features as the UPMC system.

5.4 References

1. Fercher AF, Hitzenberger C, Juchem M. Measurement of intraocular optical distances using partially coherent laser-light. J Mod Opt. 1991;38(7):1327-33. doi: 10.1080/09500349114551491. PubMed PMID: WOS:A1991FW41000012.

2. Leitgeb R, Hitzenberger CK, Fercher AF. Performance of Fourier domain vs. time domain optical coherence tomography. Optics Express. 2003;11(8):889-94.

3. Choma MA, Sarunic MV, Yang CH, Izatt JA. Sensitivity advantage of swept source and Fourier domain optical coherence tomography. Optics Express. 2003;11(18):2183-9. PubMed PMID: ISI:000185185000012.

4. de Boer JF, Cense B, Park BH, Pierce MC, Tearney GJ, Bouma BE. Improved signal-to-noise ratio in spectral-domain compared with time-domain optical coherence tomography. Opt Lett. 2003;28(21):2067-9. PubMed PMID: 14587817.

5. Chinn SR, Swanson EA, Fujimoto JG. Optical coherence tomography using a frequency-tunable optical source. Opt Lett. 1997;22(5):340-2. PubMed PMID: ISI:A1997WJ76500029.

6. Golubovic B, Bouma BE, Tearney GJ, Fujimoto JG. Optical frequency-domain reflectometry using rapid wavelength tuning of a Cr4+:forsterite laser. Opt Lett. 1997;22(22):1704-6. PubMed PMID: ISI:A1997YF19400015.

7. Swanson EA, Chinn SR, inventors; Massachusetts Institute of Technology (Cambrige, MA), assignee. Method and apparatus for performing optical measurements using a rapidly frequency-tuned laser. United States1999.

8. Liu JJ, Grulkowski I, Kraus MF, Potsaid B, Lu CD, Baumann B, Duker JS, Hornegger J, Fujimoto JG. In vivo imaging of the rodent eye with swept source/Fourier domain OCT. Biomedical optics express. 2013;4(2):351-63. PubMed PMID: ISI:000314806600016.

9. Leitgeb R, Schmetterer L, Drexler W, Fercher A, Zawadzki R, Bajraszewski T. Real-time assessment of retinal blood flow with ultrafast acquisition by color Doppler Fourier domain optical coherence tomography. Opt Express. 2003;11(23):3116-21. Epub 2003/11/17. doi: 77934 [pii]. PubMed PMID: 19471434.

10. White B, Pierce M, Nassif N, Cense B, Park B, Tearney G, Bouma B, Chen T, de Boer J. In vivo dynamic human retinal blood flow imaging using ultra-high-speed spectral domain optical coherence tomography. Opt Express. 2003;11(25):3490-7. Epub 2003/12/15. doi: 78206 [pii]. PubMed PMID: 19471483.

11. Makita S, Hong Y, Yamanari M, Yatagai T, Yasuno Y. Optical coherence angiography. Opt Express. 2006;14(17):7821-40. Epub 2006/08/21. doi: 97672 [pii]. PubMed PMID: 19529151.

12. Zhi Z, Cepurna W, Johnson E, Shen T, Morrison J, Wang RK. Volumetric and quantitative imaging of retinal blood flow in rats with optical microangiography. Biomed Opt Express. 2011;2(3):579-91. Epub 2011/03/18. doi: 10.1364/BOE.2.000579. PubMed PMID: 21412463; PubMed Central PMCID: PMC3047363.

13. Baumann B, Potsaid B, Kraus MF, Liu JJ, Huang D, Hornegger J, Cable AE, Duker JS, Fujimoto JG. Total retinal blood flow measurement with ultrahigh speed swept source/Fourier domain OCT. Biomed Opt Express. 2011;2(6):1539-52. Epub 2011/06/24. doi: 10.1364/BOE.2.001539 143940 [pii]. PubMed PMID: 21698017; PubMed Central PMCID: PMC3114222.

14. Kraus MF, Potsaid B, Mayer MA, Bock R, Baumann B, Liu JJ, Hornegger J, Fujimoto JG. Motion correction in optical coherence tomography volumes on a per A-scan basis using orthogonal scan patterns. Biomed Opt Express. 2012;3(6):1182-99.

15. Potsaid B, Baumann B, Huang D, Barry S, Cable AE, Schuman JS, Duker JS, Fujimoto JG. Ultrahigh speed 1050nm swept source/Fourier domain OCT retinal and anterior segment imaging at 100,000 to 400,000 axial scans per second. Opt Express. 2010;18(19):20029-48. Epub 2010/10/14. doi: 10.1364/OE.18.020029 205532 [pii]. PubMed PMID: 20940894; PubMed Central PMCID: PMC3136869.

16. Calderone L, Grimes P, Shalev M. Acute reversible cataract induced by xylazine and by ketamine-xylazine anesthesia in rats and mice. Exp Eye Res. 1986;42(4):331-7. Epub 1986/04/01. doi: 0014-4835(86)90026-6 [pii]. PubMed PMID: 3754819.

17. Wang L, Hofer B, Chen YP, Guggenheim JA, Drexler W, Povazay B. Highly reproducible swept-source, dispersion-encoded full-range biometry and imaging of the mouse eye. J Biomed Opt. 2010;15(4):046004. Epub 2010/08/31. doi: 10.1117/1.3463480. PubMed PMID: 20799806.

18. Grulkowski I, Liu JJ, Potsaid B, Jayaraman V, Lu CD, Jiang J, Cable AE, Duker JS, Fujimoto JG. Retinal, anterior segment and full eye imaging using ultrahigh speed swept source OCT with vertical-cavity surface emitting lasers. Biomed Opt Express. 2012;3(11):2733-51. Epub 2012/11/20. doi: 10.1364/BOE.3.002733 172948 [pii]. PubMed PMID: 23162712; PubMed Central PMCID: PMC3493240.

19. Zhi Z, Cepurna WO, Johnson EC, Morrison JC, Wang RK. Impact of intraocular pressure on changes of blood flow in the retina, choroid, and optic nerve head in rats investigated by optical microangiography. Biomed Opt Express. 2012;3(9):2220-33. Epub 2012/10/02. doi: 10.1364/BOE.3.002220 172520 [pii]. PubMed PMID: 23024915; PubMed Central PMCID: PMC3447563.

20. Zhi Z, Yin X, Dziennis S, Wietecha T, Hudkins KL, Alpers CE, Wang RK. Optical microangiography of retina and choroid and measurement of total retinal blood flow in mice. Biomed Opt Express. 2012;3(11):2976-86. Epub 2012/11/20. doi: 10.1364/BOE.3.002976 175442 [pii]. PubMed PMID: 23162733; PubMed Central PMCID: PMC3493231.

21. Srinivasan VJ, Wojtkowski M, Fujimoto JG, Duker JS. In vivo measurement of retinal physiology with high-speed ultrahigh-resolution optical coherence tomography. Opt Lett. 2006;31(15):2308-10. Epub 2006/07/13. doi: 90823 [pii]. PubMed PMID: 16832468.

22. Choi W, Baumann B, Liu JJ, Clermont AC, Feener EP, Duker JS, Fujimoto JG. Measurement of pulsatile total blood flow in the human and rat retina with ultrahigh speed spectral/Fourier domain OCT. Biomed Opt Express. 2012;3(5):1047-61. Epub 2012/05/09. doi: 10.1364/BOE.3.001047 164091 [pii]. PubMed PMID: 22567595; PubMed Central PMCID: PMC3342181.

CHAPTER 6

Enhanced Vitreous Imaging using Ultrahigh Speed Swept-Source / Fourier Domain OCT

6.1 Introduction

The vitreous is a transparent hydrophilic gel, principally composed of water, occupying the space between the lens at the front of the eye and the retina lining the back of the eye. The vitreous functions as a pathway for nutrients utilized by the lens, ciliary body, and retina, and provides structural support to the globe. Aging of the vitreous is characterized by liquefaction and the formation of liquefied vitreous pockets in a process known as synchysis. When vitreous liquefaction and weakening of vitreoretinal adhesion occur concurrently, the vitreous collapses in a process called syneresis, which eventually leads to posterior vitreous detachment (PVD).[1] In vivo imaging of the vitreous can be performed using ophthalmoscopy, slit lamp biomicroscopy, scanning laser ophthalmoscopy, ultrasonography, and optical coherence tomography (OCT).[2] However, due to its transparency, it remains difficult to reliably image the vitreous except in advanced disease.

OCT is a non-invasive, in vivo optical imaging modality analogous to ultrasound, but based on low coherence optical interferometry.[3] Standard time-domain OCT has been used clinically to examine the vitreous in a number of diseases of the vitreomacular interface.[4] Current spectral / Fourier domain OCT (SD-OCT) technology allows better visualization of the vitreoretinal interface and posterior vitreous cortex through improved axial resolution, imaging speed, and signal-to-noise ratio. Currently, SD-OCT is increasingly being used to diagnose and manage vitreoretinal interface disease processes including vitreomacular traction (VMT), epiretinal membrane (ERM), lamellar holes, pseudoholes, and full thickness macular holes (FTMH).[5-8]

The development of swept-source / Fourier domain OCT (SS-OCT) technology has enabled better sensitivity with imaging depth, longer imaging range, higher detection efficiencies, and ability to perform dual balanced detection.[9] Compared to SD-OCT, SS-OCT does not suffer from decreased signal strength with increasing imaging depth, and a tissue of interest does not need to be in close proximity to the zero delay line to enhance visualization, as is the case in enhanced depth imaging (EDI).[10] Using single-line SS-OCT scans, studies have determined the prevalence of the *bursa premacularis* (BPM) and area of Martegiani and measured the dimensions of the BPM.[11, 12]

The ability to correct motion artifacts using orthogonally scanned three-dimensional OCT (3D-OCT) datasets has been demonstrated recently.[13] Although the shortened image acquisition time of

Fourier domain OCT (SD-OCT and SS-OCT) minimizes motion artifacts and avoids the need for motion-correcting algorithms for cross-sectional OCT images in the fast scanning direction, the visualization of topographic features in 3D-OCT data is still compromised by eye motion artifacts in the slow scanning direction. This problem persists even in OCT devices with transverse eye tracking, limiting the ability to visualize 3D-OCT scans in all cross-sectional dimensions. By acquiring multiple 3D-OCT datasets with orthogonal fast scanning directions, the registration motion-correction algorithm can be applied to remove motion artifacts and merge multiple datasets into a single motion-corrected dataset with improved signal. Arbitrary cross-sections can be extracted from the motion-corrected dataset and displayed as an OCT cross-sectional image.

OCT images are typically displayed in logarithmic scale in order to accommodate the large dynamic range of the backscattered light from the retina and vitreous. A typical dynamic range of a Fourier domain OCT image in the eye is ~40 dB, while the detection sensitivity in OCT can be as high as ~100 dB.[14] Since a limited number of color or grey scale levels can be displayed in an image and perceived by the human eye, only a small subset of the entire dynamic range can be chosen to optimize contrast within specific tissue structures. Similar to X-ray computed tomography (CT), where tissues of various densities such as bone, soft-tissue, liver, and lung can be viewed by changing contrast windows, OCT images can also be "windowed" to improve visualization of the vitreous structure.[11, 15, 16] Another complementary approach is tone mapping using adaptive histogram equalization algorithms to convert high-dynamic-range (HDR) images to a displayable range while preserving the contrast, brightness, and fine detail.[17]

The present study describes normal vitreous architecture using wide-field three-dimensional OCT (3D-OCT) scans acquired using a prototype long-wavelength SS-OCT system, along with the use of both windowing and HDR techniques for an enhanced visualization of the anatomic and microstructural features of the vitreous. The aims of this pilot study were: (1) to describe a novel imaging method – enhanced vitreous imaging (EVI), (2) to examine in vivo details of the vitreous structure in healthy eyes with wide-field 3D-OCT scans covering the fovea and optic nerve head regions, (3) to evaluate EVI detection sensitivity of vitreal and vitreoretinal features versus standard OCT imaging displayed in logarithmic scale.

6.2 Methods

A research prototype SS-OCT instrument was built as described in Chapter 5 achieving 100,000 axial scans per second, which is ~4× faster imaging speed than standard clinical SD-OCT devices, with

comparable <6 μm axial image resolution. This prototype SS-OCT device operates at the 1050nm wavelength regime and has better immunity to ocular opacity and improved image penetration into tissue compared to standard clinical OCT devices, which operate at around 840 nm.[9, 18]

Healthy volunteers from the New England Eye Center at Tufts Medical Center (Boston, MA) were prospectively enrolled in the study, which was approved by the institutional review boards at Tufts Medical Center and the Massachusetts Institute of Technology. The research adhered to the Declaration of Helsinki and the Health Insurance Portability and Accountability Act. Signed informed consent was obtained from all participants.

Twenty-two eyes of 22 healthy subjects with normal vision and no history of retinal disease, optic nerve abnormalities, or ocular surgery were imaged at the New England Eye Center at Tufts Medical Center. One randomly selected eye for each subject was imaged using the prototype long-wavelength SS-OCT system. Up to eight orthogonally raster scanned 3D-OCT datasets were acquired in each eye over a 12 mm × 12 mm retinal area (~40°) with 500 A-scans × 500 B-scans centered between the fovea and the optic nerve by a single trained operator. The acquisition time per 3D-OCT dataset was less than 3 seconds. A registration motion-correction algorithm was applied to remove motion artifacts. A minimum of two orthogonally scanned 3D-OCT scans were merged to create a single, motion-corrected volumetric dataset with improved signal. With a three-dimensional (3D) motion-corrected volumetric dataset, arbitrary OCT images can be viewed in any two-dimensional plane. Details of the registration motion-correction algorithm have been described previously.[13]

To enhance visualization of vitreal and vitreoretinal features, each motion-corrected volumetric dataset was displayed in (1) the standard OCT logarithmic scale, (2) EVI vitreous window display – a windowing method analogous to CT that was performed by adjusting the threshold and contrast in each motion-corrected volumetric dataset,[15] and (3) EVI HDR display – a HDR filtering method that was performed by applying a contrast-limited adaptive histogram equalization (CLAHE) filter to the motion-corrected volumetric dataset in linear scale.[17] All EVI image processing was performed using the plugins in ImageJ (NIH, Bethesda, MD). Figure 6.1 is an example of a motion-corrected dataset shown in the standard logarithmic scale display, the EVI vitreous window display, and the EVI HDR display. Figure 6.2 demonstrates 3D EVI OCT where arbitrary cross sections as well as en face images extracted from the 3D volumetric dataset are shown. The hypothesis of this study was that enhanced vitreous imaging (EVI) using the windowing or HDR method improves detection sensitivity of vitreal and vitreoretinal features compared to standard OCT logarithmic scale display.

Each dataset, displayed in 3 forms (Figure 6.1), was reviewed independently by three OCT readers (J.J.L, A.J.W, and M.A. each with 1 year or more full-time ophthalmic OCT research experience in a PhD or research fellowship program). Datasets were reviewed in random order and separated by display methods so each dataset is examined independently for each display method. The presence of specific anatomic and microstructural features within the posterior vitreous and vitreoretinal interface was identified by examining multiple cross-sectional images extracted from the 3D volumetric dataset. Features studied included the BPM, Cloquet's canal (area of Martegiani), Cloquet's/BPM septum, Bergmeister papilla, posterior cortical vitreous (hyaloid) detachment, papillomacular hyaloid detachment, hyaloid attachment to retinal vessel(s), granular opacities within vitreous cortex, granular opacities within Cloquet's canal, and granular opacities within the BPM. (Figure 6.3) Specific locations of microstructural features in each cross-sectional image were recorded by each reader. Disagreement between readers was resolved by open adjudication. The decision of whether to classify each feature as present or absent was determined by combining positive findings from the standard logarithmic scale display, EVI vitreous window display, and EVI HDR display in order to generate the maximum possible level of detection for each feature. More specifically, since there does not exist a standard imaging method to examine all features observed, if there is a positive result in any of the three display methods, the existence of the feature is considered positive. The sensitivity of each display method for the detection of each vitreal and vitreomacular feature was calculated as the proportion of true positives correctly identified as such (Sensitivity = True Positives/(True Positives + False Negatives)). The 95% confidence interval (CI) for detection of all the vitreal and vitreomacular features for each display method was also calculated. All statistical analysis was conducted using Excel (Microsoft Corporation, Redmond, WA).

To demonstrate the ability to analyze posterior vitreous structures in 3D, a motion-corrected volumetric dataset of a selected eye was processed using the EVI vitreous window. In the 3D dataset, the volumes of the BPM and area of Martegiani were measured, both which are optically transparent spaces within the vitreous. The same eye was used to demonstrate mapping of vitreous detachment from the retinal surface. Manual segmentation of the BPM and area of Martegiani and the manual mapping of vitreous detachment were performed using Amira (Visualization Sciences Group, Burlington, MA).

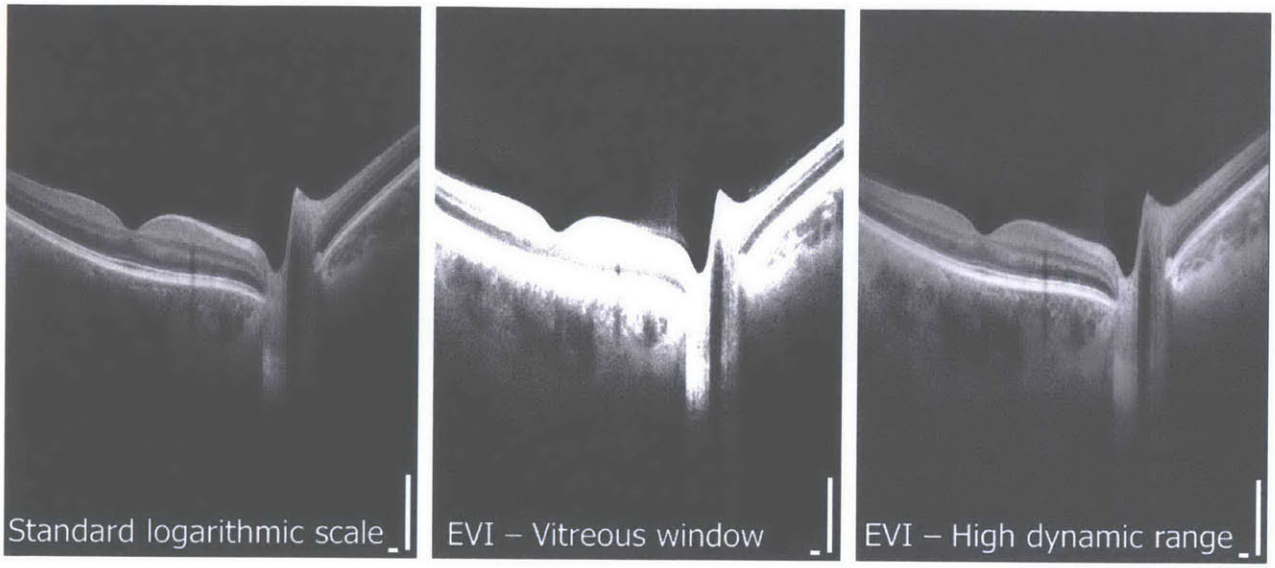

Figure 6.1 Optical coherence tomography (OCT) images are typically displayed in logarithmic scale. Enhanced vitreous imaging (EVI) with the vitreous window and high-dynamic-range methods improves visualization of structure in the posterior vitreous and vitreoretinal interface. Scale bars: 300 μm.

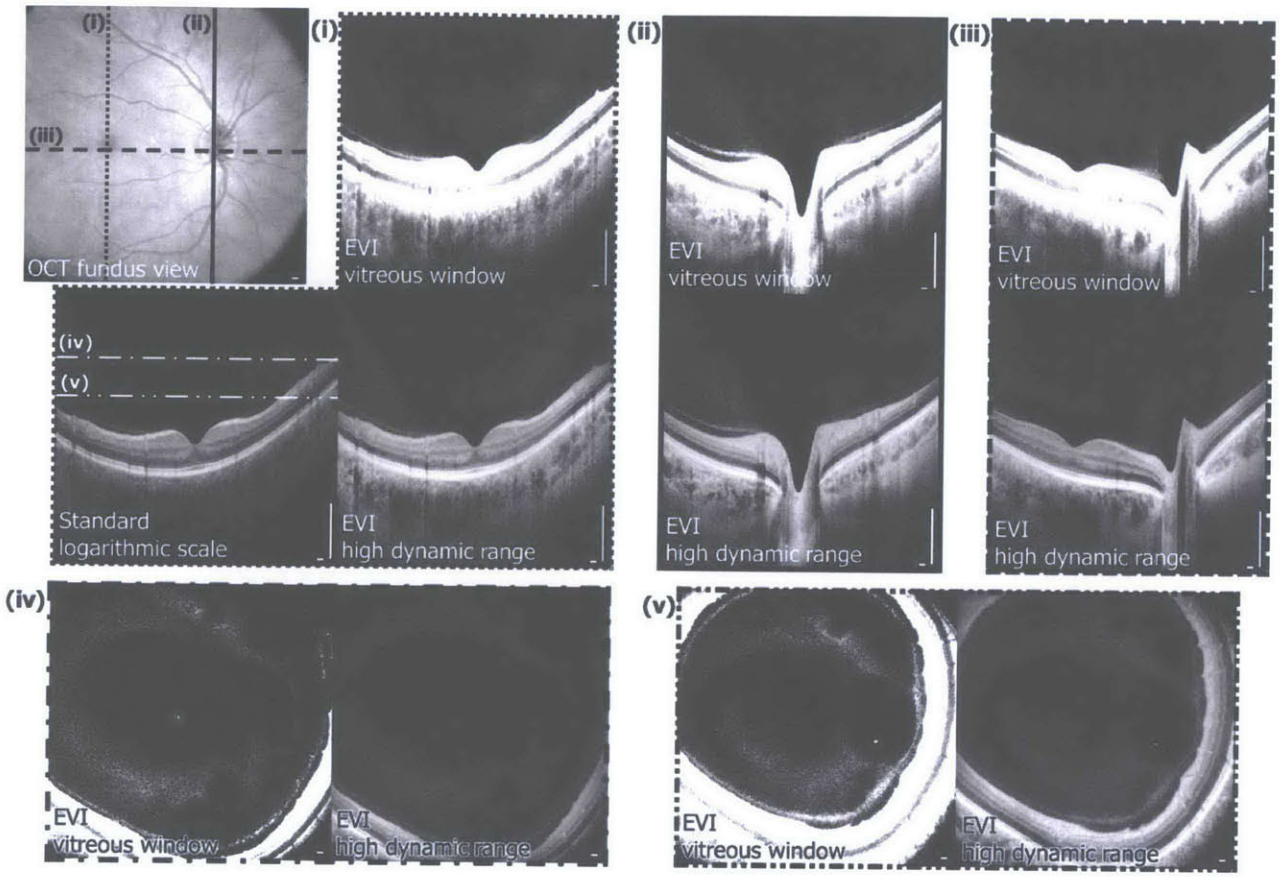

Figure 6.2 Three-dimensional (3D) enhanced vitreous imaging (EVI) enables visualization of the posterior vitreous and vitreoretinal interface in arbitrary cross sections or any en face plane. Arbitrary cross-sectional images and arbitrary en face images are generated from the 3D motion-corrected volumetric dataset with EVI display. Scale bars: 300 μm.

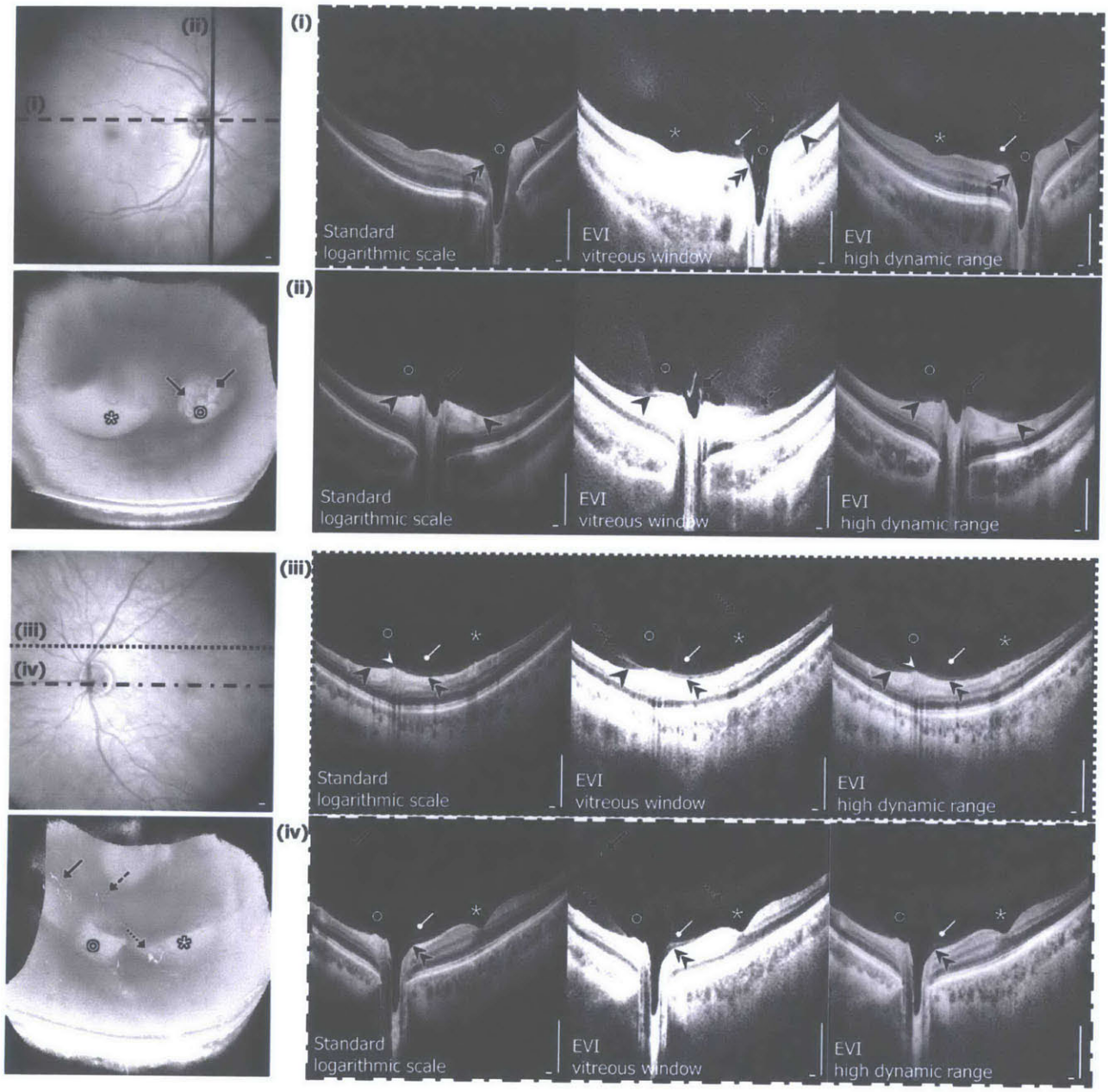

Figure 6.3 Examples of features observed in the posterior vitreous and vitreoretinal interface in healthy eyes. Selected cross sections from two different eyes are shown with their locations marked on the optical coherence tomography (OCT) fundus images. Renderings of the 3D volumetric datasets are also shown. Note the cloudy gray appearance of reflective signal from the

vitreous, where liquefied areas of the vitreous appear transparent and hyperreflective foci appear white. Observed features are marked in the cross-sectional images: *bursa premacularis* (BPM) (white asterisk), Cloquet's canal (Area of Martegiani) (white circle), Cloquet's/BPM septum (white circle arrow), posterior cortical vitreous (hyaloid) detachment (black arrowhead), papillomacular hyaloid detachment (double black arrowheads), Bergmeister papilla (black diamond arrow), hyaloid attachment to retinal vessel (white arrowhead), granular opacities within vitreous cortex (black dashed arrow), granular opacities within BPM (black dotted arrow), granular opacities within Cloquet's (black arrow). Scale bars: 300 μm.

6.3 Results

The mean age of the 22 healthy subjects was 33.0 years, with a range of 23 to 49 years. There were 12 females (54.5%) and 10 males (45.5%). The features of the posterior vitreous and vitreoretinal interface observed with all display methods are shown in Table 6.1.

To test the hypothesis that EVI improves visualization of vitreal and vitreoretinal features, we compared images displayed without enhancement to images enhanced with the two EVI methods. The sensitivity for detection of all vitreal and vitreoretinal features in this study was 75.0% (95% CI: 67.8%-81.1%) for the standard logarithmic scale display, 80.6% (95% CI: 73.8%-86.0%) for the EVI HDR display and 91.9% (95% CI: 86.6%-95.2%) for the EVI vitreous window display. The EVI vitreous window display was able to detect an additional 34 (21.3%) features that were not visible on the standard logarithmic scale display and 30 (18.8%) features that were not visible on the EVI HDR display. The EVI HDR display detected an additional 25 (15.6%) features that were not visible on the standard logarithmic scale display and 10 (6.3%) features that were not visible on the EVI vitreous window display. Three features (1.9%) were visible on the standard logarithmic scale display but not evident on either EVI vitreous window display or the EVI HDR display.

The detection sensitivity for each of the vitreal and vitreoretinal features using the 3 display methods are shown in Table 6.2. The EVI vitreous window display was more sensitive than the standard logarithmic scale display in detecting all the features. The EVI HDR display was more sensitive than the standard logarithmic scale display in detecting the BPM (94.4% vs 77.8%), Cloquet's/BPM septum (100% vs 82.4%), Bergmeister papilla (81.8% vs 63.6%), posterior cortical vitreous (hyaloid) detachment (100% vs 90.0%), and hyaloid attachment to retinal vessel(s) (81.3% vs 68.8%). EVI HDR had a comparable sensitivity to the standard logarithmic scale display in detecting area of Martegiani (93.3%), papillomacular hyaloid detachment (81.3%), granular opacities within Cloquet's (70.6%), and granular opacities within BPM (58.8%) and was less sensitive than the standard logarithmic scale display in

detecting granular opacities within vitreous cortex (30.7% vs 53.8%). The EVI vitreous window display had a higher or comparable sensitivity to EVI HDR display for detecting most vitreal and vitreoretinal features, except for detecting hyaloid attachment to retinal vessels and BPM, where EVI HDR display was more sensitive than the EVI vitreous window display (81.3% vs 75.0% and 94.4% vs. 88.9% respectively).

Using 3D information from a motion-corrected dataset of a selected eye processed using the EVI vitreous window display, the BPM was measured to be 6.84 μL and the area of Martegiani was measured to be 3.06 μL (Figure 6.4). A vitreous detachment map was also generated for this eye, which illustrates remaining vitreal attachment over the macula and optic nerve head region as well as over a retinal vessel nasal to the optic nerve head (Figure 6.5). The measured areas of attachment are 20.9 mm^2 above the macula, 9.7 mm^2 over the optic nerve head, and 0.2 mm^2 along the retinal vessel. All quantitative measurements are performed within the axial imaging range and transverse field of view of the long-wavelength SS-OCT system employed in this study.

To demonstrate the potential utility of EVI in vitreoretinal disease, a clinical example of vitreomacular traction (VMT) syndrome is also displayed using the EVI methods (Figure 6.6). This is a 78-year-old man who presented to the New England Eye Center at Tufts Medical Center with visual distortion in his left eye. His best-corrected visual acuity was 20/40. Dilated fundus examination showed mild retinal pigment epithelium (RPE) changes, mild retinal thickening nasal to the fovea, and an epiretinal membrane (ERM). OCT imaging revealed that the patient had VMT syndrome: a partially-detached and thickened posterior hyaloid with persistent adhesion to the fovea, causing mild distortion of the foveal contour. Using the vitreous enhancement techniques applied to SS-OCT images, the contour and shape of the posterior hyaloid becomes clearly visible. En face images highlight the presence of individual vitreous fibers temporal to the macula; these fibers are also visualized in the 3D reconstruction of the volumetric dataset. The vitreous detachment map highlights that the vitreous remains attached at both the macula and optic nerve head, as well as along retinal arcade vessels and vessels nasal to the optic nerve. The measured areas of attachment are 4.4 mm^2 over the macula and 23.2 mm^2 over the optic nerve head and vessels.

Table 6.1 Features of the posterior vitreous and vitreoretinal interface observed in healthy eyes.

Vitreal or Vitreoretinal Feature	**Healthy Eyes with Feature n, (%)**
Bursa Premacularis (BPM)	18 (81.8%)
Cloquet's canal (Area of Martegiani)	15 (68.2%)
Cloquet's/BPM Septum	17 (77.3%)
Bergmeister papilla	11 (50.0%)
Posterior cortical vitreous (hyaloid) detachment	20 (90.9%)
Papillomacular hyaloid detachment	16 (72.7%)
Hyaloid attachment to retinal vessel(s)	16 (72.7%)
Granular opacities within vitreous cortex	13 (59.1%)
Granular opacities within Cloquet's	17 (77.3%)
Granular opacities within BPM	17 (77.3%)

Table 6.2 Detection of vitreal and vitreoretinal features in healthy eyes.

Observed Features	Sensitivity %, (95% Confidence Interval)		
	Standard OCT Logarithmic Scale Display	EVI: Vitreous Window Display	EVI: HDR Display
Bursa Premacularis (BPM)	77.8 (54.8 to 91.0)	88.9 (67.2 to 96.9)	94.4 (74.2 to 99.0)
Cloquet's canal (Area of Martegiani)	93.3 (70.2 to 98.8)	100.0 (79.6 to 100.0)	93.3 (70.2 to 98.8)
Cloquet's/BPM Septum	82.4 (59.0 to 93.8)	100.0 (81.6 to 100.0)	100.0 (81.6 to 100.0)
Bergmeister papilla	63.6 (35.4 to 84.8)	90.1 (62.3 to 98.4)	81.8 (52.3 to 94.9)
Posterior cortical vitreous (hyaloid) detachment	90.0 (69.9 to 97.2)	100.0 (83.9 to 100.0)	100.0 (83.9 to 100.0)
Papillomacular hyaloid detachment	81.3 (57.0 to 93.4)	93.8 (71.7 to 98.9)	81.3 (57.0 to 93.4)
Hyaloid attachment to retinal vessel(s)	68.8 (44.4 to 85.8)	75.0 (50.5 to 89.8)	81.3 (57.0 to 93.4)
Granular opacities within vitreous cortex	53.8 (29.1 to 76.8)	92.3 (66.7 to 98.6)	30.7 (12.7 to 57.6)
Granular opacities within Cloquet's	70.6 (46.9 to 86.7)	88.2 (65.7 to 96.7)	70.6 (46.9 to 86.7)
Granular opacities within BPM	58.8 (36.0 to 78.4)	88.2 (65.7 to 96.7)	58.8 (36.0 to 78.4)

OCT = Optical Coherence Tomography; EVI = Enhanced Vitreous Imaging; HDR = High Dynamic Range

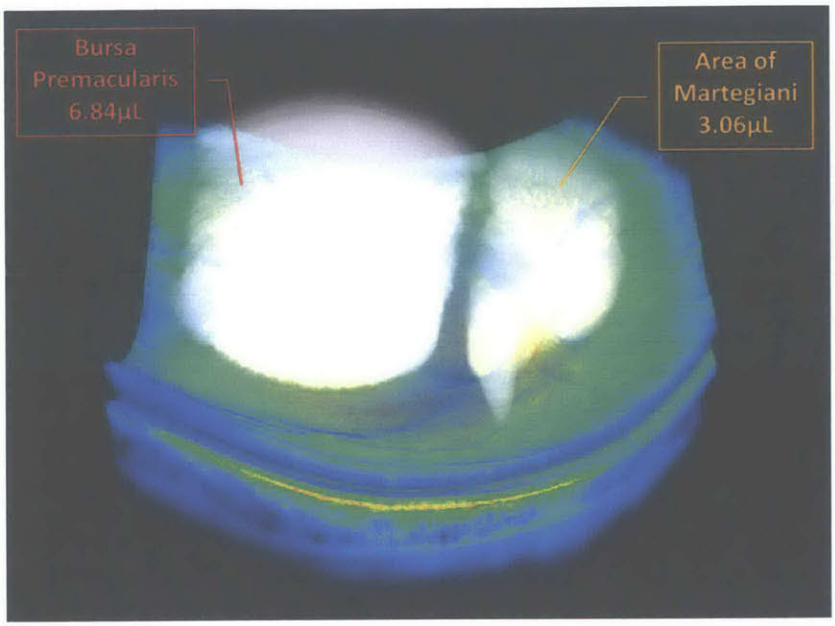

Figure 6.4 Volumetric measurement of vitreal spaces can be performed in three-dimensional (3D) enhanced vitreous imaging (EVI) volumetric datasets. The *bursa premacularis* (BPM) and area of Martegiani are segmented and highlighted. The volume of the BPM and area of Martegiani measured within the imaging range of the dataset is 6.84 µL and 3.06 µL, respectively.

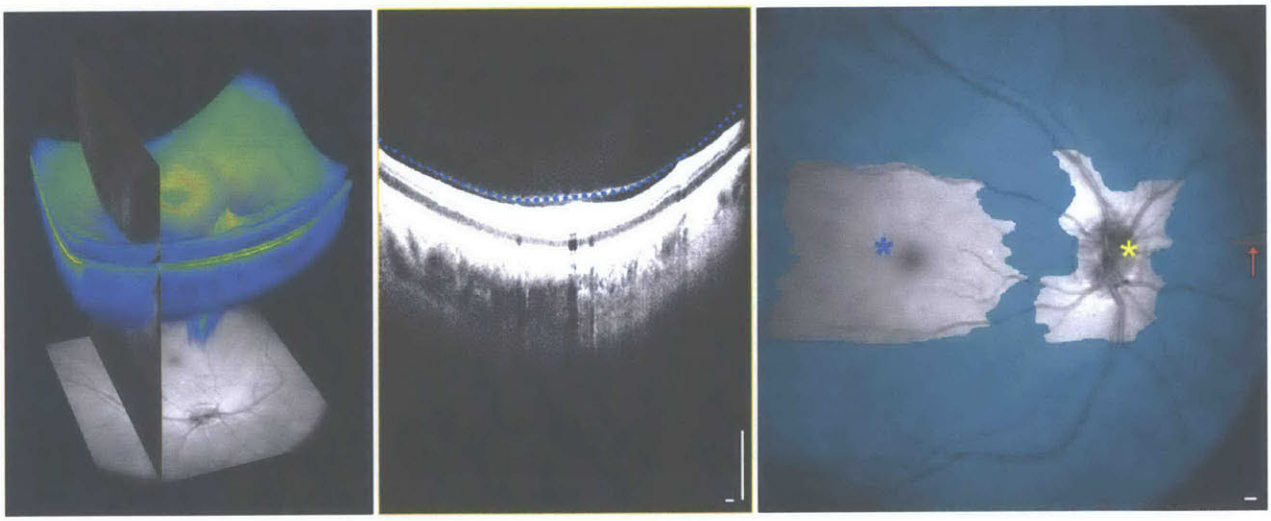

Figure 6.5 Vitreal detachment from the retina can be mapped in three-dimensional (3D) enhanced vitreous imaging (EVI) volumetric datasets by examining each cross-sectional image in a 3D dataset (left) and marking the detached hyaloid (center) to generate a map where the area of vitreal detachment is highlighted (right). Vitreoretinal attachment is present at the macula (blue asterisk) and optic nerve head (yellow asterisk) as well as along a retinal vessel (red arrow) nasal to the optic nerve head. The measured areas of attachment are 20.9 mm^2 above the macula, 9.7 mm^2 over the optic nerve head, and 0.2 mm^2 along the retinal vessel within the imaging range. Scale bars: 300 µm.

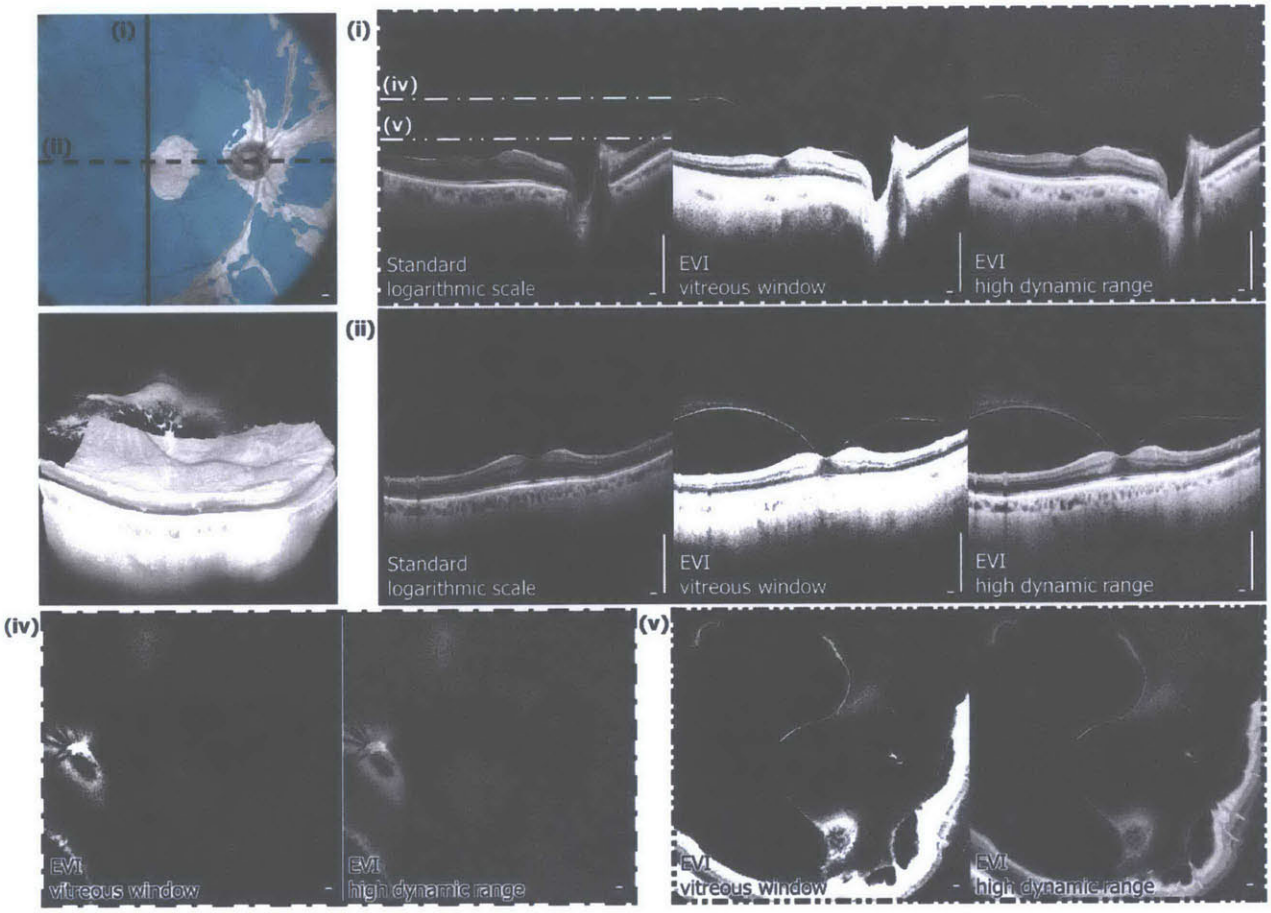

Figure 6.6 Enhanced vitreous imaging (EVI) of vitreomacular traction (VMT). (Top left) Vitreal detachment map where the measured area of attachment is 4.4 mm^2 over the macula and 23.2 mm^2 over the optic nerve head and vessels. (Second row left) Three-dimensional (3D) rendering of the EVI volumetric dataset. Note the improved visualization of the contour and shape of the posterior hyaloid with EVI. The presence of vitreous fibers and hyperreflective reflective foci in the posterior vitreous are clearly visible in the en face EVI images and three-dimensional rendering. Scale bars: 300 μm.

6.4 Discussion

This study describes a new method for improved OCT analysis of the posterior vitreous and vitreoretinal interface: Enhanced Vitreous Imaging (EVI). EVI employs processing of standard logarithmic scale SS-OCT images of healthy eyes using either the windowing technique, the "EVI vitreous windowing display", or the high-dynamic-range (HDR) technique, "EVI HDR display" for vitreous analysis and shows an enhanced sensitivity of EVI vitreous windowing display for detection of vitreal and vitreoretinal features. SS-OCT has an advantage over SD-OCT for vitreous imaging because it

maintains high sensitivity over a long imaging range. The high speed of SS-OCT combined with motion correction and merging enables wide-field volumetric imaging. As a result, SS-OCT with motion correction and EVI provides wide-field 3D information about the posterior vitreous structure, enabling detailed observations of the posterior vitreous and the vitreoretinal interface.

In this study, EVI vitreous windowing display showed statistically significant improvement in overall detection sensitivity of the posterior vitreous features compared to standard logarithmic scale display. While EVI HDR display improves the detection of some vitreal and vitreoretinal features when compared to the standard logarithmic scale display, the EVI vitreous window display seems to provide the most improvement in detecting all of the features when compared to the standard logarithmic scale display and most features when compared to the EVI HDR display. The EVI HDR display is significantly worse in detecting granular opacities compared to the EVI vitreous window display (30.7% vs 92.3%). This may be due to the blurring effect on very small features when applying the CLAHE filter. Conversely, the EVI HDR display was more sensitive in detecting hyaloid attachment to the retinal vessels (81.3% vs 75.0%) and the BPM (94.4% vs. 88.9%) when compared to the EVI vitreous window display. The preserved contrast in the retina, combined with enhanced visualization of the vitreous in the EVI HDR display may be valuable in detecting interactions between the vitreous and the retina, such as at the attachment of the hyaloid to retinal vessels and fibrovascular vitreoretinal adhesions in diseases such as advanced diabetic retinopathy. In addition, the EVI HDR display has the ability to visualize vitreous, retinal, and choroidal structures in a single image similar to the combined depth imaging SD-OCT images shown by Barteselli et al.[19]

Prior studies evaluated features in the posterior vitreous and vitreoretinal interface using commercial SD-OCT and SS-OCT systems. Koizumi et al. presented 3D visualization of the VMT and idiopathic ERM using SD-OCT over a 6 mm × 6mm retinal area where hyperreflectivity of the detached posterior hyaloid was observed.[5] Mojana et al. demonstrated the ability of SD-OCT to image the physiologic and pathologic vitreous structure to provide detailed analysis of the vitreoretinal interface.[20] The authors found that SD-OCT showed a higher prevalence of PVD compared to clinical slit-lamp biomicroscopy examination as well as improved visualization of details in the posterior vitreous and vitreoretinal interface. Observations including the BPM, area of Martegiani, Bergmeister papilla, hyaloid adhesion to retinal vessels, hyperreflective vitreous strands, and granular opacities described as insertion of anteroposterior fibers or cellular aggregations were reported in cross-sectional SD-OCT images. Shimada et al. described the size and dimension of BPMs observed in normal eyes as well as its separation from the pre-papillary Cloquet's canal by a thin wall observed by acquiring single-line 9 mm nasal-temporal and 6 mm superior-inferior cross-sectional SD-OCT scans.[21] Itakura and Kishi further

confirmed the presence of BPM in all ages and observed thickened vitreous cortex and perifoveal posterior vitreous detachment in older individuals by adjusting the contrast in the single-line 9 mm nasal-temporal SD-OCT cross-sectional images, similar to the EVI "windowing" approach performed in the present study.[15] Recent results from Itakura et al. showed clarified boat-shaped BPM structure in vivo using single-line 12 mm nasal-temporal and 12 mm superior-inferior SS-OCT scans where brightness and contrast of the images were adjusted to enhance the vitreous.[11] In addition, Stanga et al. performed anatomical characterization of the cortical vitreous and vitreoretinal interface using the single-line 12 mm nasal-temporal SS-OCT scan by measuring the width and depth of the BPM and classification of the degree of posterior vitreous detachment.[11, 12]

Nevertheless, the analyses in previous studies were either restricted to isolated cross sections or 3D datasets with inadequate cross-sectional image quality as well as limited retina coverage. The present study is the first of its kind to demonstrate that posterior vitreous structure and the vitreoretinal interface can be visualized in 3D using wide-field motion-corrected volumetric SS-OCT datasets and EVI, allowing measurements of the volumes in physiological vitreous spaces such as the BPM and the Cloquet's canal. Moreover, mapping of the locus and area of vitreous detachment from the retina and measurement of the area of vitreoretinal adhesion can also be accomplished in normal eyes as well as eyes with vitreoretinal disease, as demonstrated in an eye with vitreomacular traction syndrome. Such measurements and maps may be helpful to follow vitreous detachment over time, for preoperative planning, and/or to assess treatment response to surgery or enzymatic vitreolysis.

A limitation of this study is that only healthy subjects were included. Studies in diseased eyes using EVI are currently underway and will help better understand the clinical significance of features observed in the posterior vitreous and vitreoretinal interface. Another limitation is the imaging speed and imaging range of our prototype SS-OCT system. Our current prototype SS-OCT already achieves ~4× higher imaging speed (100,000 A-scans/second), ~40% longer imaging range (2.8 mm), and ~2× transverse field of view (12 mm × 12 mm) than commercial SD-OCT systems. However, since the vitreous is a dynamic tissue and its shape and configuration may be altered with eye movement and position, it is possible that the vitreous anatomy changes during the time interval between acquisitions of multiple 3D-OCT datasets[16], which may result in blurring of certain vitreal and vitreoretinal features when the registration motion-correction algorithm is applied. Furthermore, with the current system design we can still only visualize the posterior vitreous and not the entire vitreous. Visualization of structures such as the BPM, area of Martegiani, and vitreal attachment to the retinal vessels in our study is also limited by the axial imaging range and transverse field of view of the prototype SS-OCT system. A study by Mori et al. suggested that imaging the peripheral vitreous provides insights into macular hole

development and progression using a montage SD-OCT technique.[22] Future SS-OCT systems with higher speeds, faster image acquisition, improved sampling, and longer imaging range will be able to help visualize more of the vitreal and vitreoretinal features in both the transverse and anteroposterior dimensions.[23] Another potential limitation of this study is the adjustment of the focus on the retina. In our study, we performed standard OCT image acquisition procedures without special focus adjustments. Other studies have suggested that placing the focus of the OCT instrument on vitreous structure may further improve visualization of vitreous.[11] However, we believe that maintaining optimal visibility of retinal structures is most important, as the retina and the retinal pigment epithelium remain the easiest structure for ophthalmic photographers to focus on during image acquisition. Once images are acquired using a standard OCT image acquisition procedures, EVI techniques as described in this study can be performed. The ideal placement of OCT instrument optical focus during acquisition remains to be determined for vitreous imaging. A final limitation of the study was that 3D processing of images was performed manually, which was time consuming. Future development of computer image analysis algorithms will enable rapid, real time mapping of vitreous detachment.

In conclusion, in this prospective cross-sectional study, greater sensitivity of EVI for the detection of vitreal and vitreoretinal features using SS-OCT is demonstrated. EVI holds promise for an improved analysis of the vitreous for investigational and clinical purposes. EVI SS-OCT could potentially be a new tool for imaging the 3D microstructure of the vitreous in patients with disorders of the vitreomacular interface and assessing treatment response after vitrectomy or pharmacologic vitreolysis.

6.5 References

1. Sebag J, SpringerLink (Online service). The Vitreous: Structure, Function, and Pathobiology. New York, NY: Springer New York; 1989. Available from: http://dx.doi.org/10.1007/978-1-4613-8908-8.

2. Sebag J. Imaging vitreous. Eye (Lond). 2002;16(4):429-39. Epub 2002/07/09. doi: 10.1038/sj.eye.6700201. PubMed PMID: 12101450.

3. Huang D, Swanson EA, Lin CP, Schuman JS, Stinson WG, Chang W, Hee MR, Flotte T, Gregory K, Puliafito CA, et al. Optical coherence tomography. Science. 1991;254(5035):1178-81. Epub 1991/11/22. PubMed PMID: 1957169.

4. Mirza RG, Johnson MW, Jampol LM. Optical coherence tomography use in evaluation of the vitreoretinal interface: a review. Surv Ophthalmol. 2007;52(4):397-421. Epub 2007/06/19. doi: S0039-6257(07)00055-0 [pii] 10.1016/j.survophthal.2007.04.007. PubMed PMID: 17574065.

5. Koizumi H, Spaide RF, Fisher YL, Freund KB, Klancnik JM, Jr., Yannuzzi LA. Three-dimensional evaluation of vitreomacular traction and epiretinal membrane using spectral-domain optical coherence tomography. Am J Ophthalmol. 2008;145(3):509-17. Epub 2008/01/15. doi: 10.1016/j.ajo.2007.10.014 S0002-9394(07)00921-X [pii]. PubMed PMID: 18191099.

6. Chang LK, Fine HF, Spaide RF, Koizumi H, Grossniklaus HE. Ultrastructural correlation of spectral-domain optical coherence tomographic findings in vitreomacular traction syndrome. Am J Ophthalmol. 2008;146(1):121-7. Epub 2008/04/29. doi: 10.1016/j.ajo.2008.03.001 S0002-9394(08)00166-9 [pii]. PubMed PMID: 18439563; PubMed Central PMCID: PMC2987706.

7. Johnson MW. Posterior vitreous detachment: evolution and complications of its early stages. Am J Ophthalmol. 2010;149(3):371-82 e1. Epub 2010/02/23. doi: 10.1016/j.ajo.2009.11.022 S0002-9394(09)00885-X [pii]. PubMed PMID: 20172065.

8. Barak Y, Ihnen MA, Schaal S. Spectral domain optical coherence tomography in the diagnosis and management of vitreoretinal interface pathologies. J Ophthalmol. 2012;2012:876472. Epub 2012/06/16. doi: 10.1155/2012/876472. PubMed PMID: 22701779; PubMed Central PMCID: PMC3373197.

9. Potsaid B, Baumann B, Huang D, Barry S, Cable AE, Schuman JS, Duker JS, Fujimoto JG. Ultrahigh speed 1050nm swept source/Fourier domain OCT retinal and anterior segment imaging at 100,000 to 400,000 axial scans per second. Opt Express. 2010;18(19):20029-48. Epub 2010/10/14. doi: 10.1364/OE.18.020029 205532 [pii]. PubMed PMID: 20940894; PubMed Central PMCID: PMC3136869.

10. Spaide RF, Koizumi H, Pozzoni MC. Enhanced depth imaging spectral-domain optical coherence tomography. Am J Ophthalmol. 2008;146(4):496-500. Epub 2008/07/22. doi: 10.1016/j.ajo.2008.05.032 S0002-9394(08)00418-2 [pii]. PubMed PMID: 18639219.

11. Itakura H, Kishi S, Li D, Akiyama H. Observation of posterior precortical vitreous pocket using swept-source optical coherence tomography. Invest Ophthalmol Vis Sci. 2013;54(5):3102-7. Epub 2013/04/20. doi: 10.1167/iovs.13-11769 [pii]. PubMed PMID: 23599325.

12. Stanga PE, Sala-Puigdollers A, Caputo S, Jaberansari H, Cien M, Gray J, D'Souza Y, Charles SJ, Biswas S, Henson DB, McLeod D. In-vivo Imaging of Cortical Vitreous using 1,050nm Swept-Source Deep Range Imaging Optical Coherence Tomography (DRI-OCT1 Atlantis®). Am J Ophthalmol. 2013. doi: http://dx.doi.org/10.1016/j.ajo.2013.10.008.

13. Kraus MF, Potsaid B, Mayer MA, Bock R, Baumann B, Liu JJ, Hornegger J, Fujimoto JG. Motion correction in optical coherence tomography volumes on a per A-scan basis using orthogonal scan patterns. Biomed Opt Express. 2012;3(6):1182-99. Epub 2012/06/29. doi: 10.1364/BOE.3.001182 164364 [pii]. PubMed PMID: 22741067; PubMed Central PMCID: PMC3370961.

14. Brezinski ME. Optical coherence tomography : principles and applications. Amsterdam ; Boston: Academic Press; 2006. xxvii, 599 p. p.

15. Itakura H, Kishi S. Aging changes of vitreomacular interface. Retina. 2011;31(7):1400-4. Epub 2011/01/15. doi: 10.1097/IAE.0b013e318206cb43. PubMed PMID: 21233785.

16. Itakura H, Kishi S. Alterations of Posterior Precortical Vitreous Pockets with Positional Changes. Retina. 2013. Epub 2013/03/22. doi: 10.1097/IAE.0b013e31827d262a. PubMed PMID: 23514794.

17. Pizer SM, Amburn EP, Austin JD, Cromartie R, Geselowitz A, Greer T, ter Haar Romeny B, Zimmerman JB, Zuiderveld K. Adaptive histogram equalization and its variations. Computer Vision, Graphics, and Image Processing. 1987;39(3):355-68. doi: http://dx.doi.org/10.1016/S0734-189X(87)80186-X.

18. Unterhuber A, Povazay B, Hermann B, Sattmann H, Chavez-Pirson A, Drexler W. In vivo retinal optical coherence tomography at 1040 nm - enhanced penetration into the choroid. Opt Express. 2005;13(9):3252-8. Epub 2005/05/02. doi: 83715 [pii]. PubMed PMID: 19495226.

19. Barteselli G, Bartsch DU, El-Emam S, Gomez ML, Chhablani J, Lee SN, Conner L, Freeman WR. Combined depth imaging technique on spectral-domain optical coherence tomography. Am J Ophthalmol. 2013;155(4):727-32, 32 e1. Epub 2012/12/21. doi: 10.1016/j.ajo.2012.10.019 S0002-9394(12)00764-7 [pii]. PubMed PMID: 23253912; PubMed Central PMCID: PMC3608846.

20. Mojana F, Kozak I, Oster SF, Cheng L, Bartsch DU, Brar M, Yuson RM, Freeman WR. Observations by spectral-domain optical coherence tomography combined with simultaneous scanning laser ophthalmoscopy: imaging of the vitreous. Am J Ophthalmol. 2010;149(4):641-50. Epub 2010/02/09. doi: 10.1016/j.ajo.2009.11.016 S0002-9394(09)00879-4 [pii]. PubMed PMID: 20138610.

21. Shimada H, Hirose T, Yamamoto A, Nakashizuka H, Hattori T, Yuzawa M. Depiction of the vitreous pocket by optical coherence tomography. Int Ophthalmol. 2011;31(1):51-3. Epub 2010/09/22. doi: 10.1007/s10792-010-9398-4. PubMed PMID: 20857172.

22. Mori K, Kanno J, Gehlbach PL, Yoneya S. Montage images of spectral-domain optical coherence tomography in eyes with idiopathic macular holes. Ophthalmology. 2012;119(12):2600-8. Epub 2012/08/16. doi: 10.1016/j.ophtha.2012.06.027 S0161-6420(12)00558-1 [pii]. PubMed PMID: 22892150.

23. Grulkowski I, Liu JJ, Potsaid B, Jayaraman V, Lu CD, Jiang J, Cable AE, Duker JS, Fujimoto JG. Retinal, anterior segment and full eye imaging using ultrahigh speed swept source OCT with vertical-

cavity surface emitting lasers. Biomed Opt Express. 2012;3(11):2733-51. Epub 2012/11/20. doi: 10.1364/BOE.3.002733 172948 [pii]. PubMed PMID: 23162712; PubMed Central PMCID: PMC3493240.

CHAPTER 7

Vertical-Cavity Surface-Emitting Laser Swept-Source / Fourier Domain OCT

7.1 Background

Wavelength-swept lasers are the key underlying technology for swept-source / Fourier domain OCT. One of the first wavelength swept lasers built for OCT in 1997 employed an external cavity design with a galvanometer-tuned grating or a sequence of prisms, achieving 10 Hz and 2 kHz sweep repetition rates, respectively.[1, 2] Eventually, dramatic increase in speed was obtained with designs using tunable dispersive elements such as dispersion prisms, rotating polygons, resonant scanning mirrors, diffraction gratings, and scanning filters.[3-9] Most external cavity tunable lasers use bulk optics or fiber components, making resonators relatively long and limiting sweep rates. New laser techniques such as Fourier-domain mode locking (FDML) has overcome such limitations.[10] Nowadays, swept laser designs can achieve MHz range sweep rates.[11, 12] Recent advances include the development of fully integrated lasers as well as miniaturized lasers using microelectromechanical systems (MEMS) technology.[13-18]

A new wavelength-swept light source based on vertical cavity surface-emitting laser (VCSEL) technology offers superior performance for OCT imaging.[19-22] The unique features of the VCSEL light source include high speeds with real time adjustability of both the sweep rate and wavelength tuning range because of its micron-scale cavity length and the rapid MEMS response time.[23] Moreover, the VCSEL operates with a single longitudinal mode instead of multiple modes and therefore has an extremely narrow instantaneous linewidth compared with other lasers. This results in a very long coherence length and makes a long imaging range possible. Therefore, MEMS-tunable VCSELs is an extraordinary technology for the exploration of both high speed and long range swept-source / Fourier domain OCT imaging.

Swept-source / Fourier domain OCT using the VCSEL light source has the advantage that the wavelength sweep range and repetition rate of the light source can be adjusted in order to tailor the resolution, imaging range and axial scan rate to specific imaging applications. Tradeoff in these parameters provides flexibility for easily reconfigurable OCT system performance. By taking advantage of different operating points of the OCT system it is possible to explore versatile functionalities which contribute to a diversity of new applications. In collaboration with Praevium and Thorlabs, VCSEL light source technology was developed to enable ultrahigh speeds, long imaging range, and adjustable speed, range and resolution. Figure 7.1 is an illustration of the VCSEL structure and VCSEL light source module.

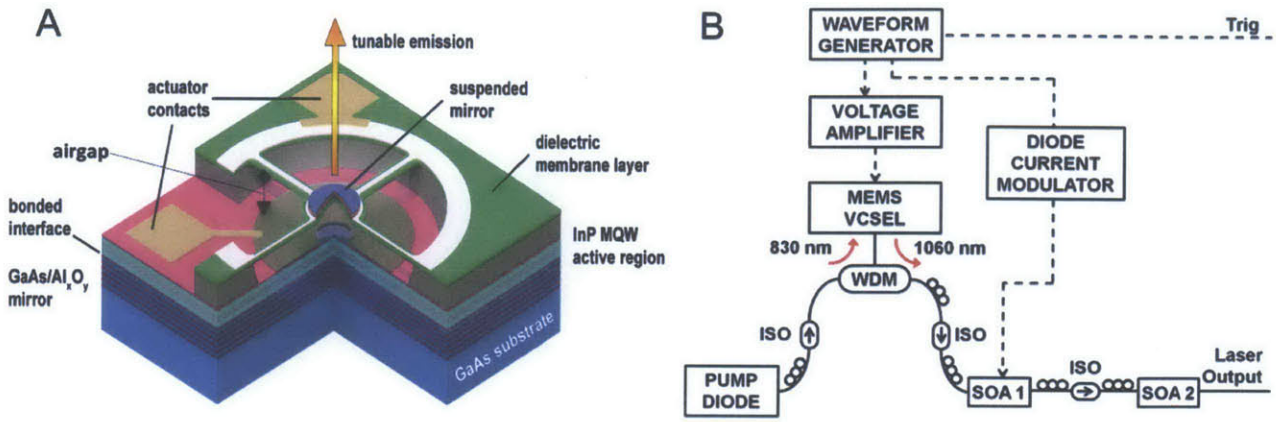

Figure 7.1 (A) Schematic of a MEMS-tunable VCSEL structure. GaAs – gallium arsenide, AlxOy – aluminum oxide, InP – indium phosphide, MQW – multiple quantum well. (B) Schematic of VCSEL light source module: WDM – wavelength-division multiplexer, ISO – isolator, SOA – booster optical amplifiers. Electrical signals indicated by dashed lines.[25]

7.2 Ophthalmic Imaging Using VCSEL Swept-Source / Fourier Domain OCT

A schematic diagram of a prototype VCSEL swept-source / Fourier domain OCT (SS-OCT) imaging system along with a photograph of an ophthalmic prototype OCT instrument is shown in Figure 7.2. The VCSEL light source was designed and manufactured by Praevium Inc. and Thorlabs Inc. The output of the swept-source laser was divided between the OCT interferometer and a Mach-Zehnder interferometer (MZI) for sweep calibration. Light entering the OCT interferometer was split through another fiber coupler into the sample and reference arms. The sample arm of the OCT interferometer was attached to an imaging interface for scanning the eye. The light incident on the eye was 1.9 mW, consistent with American National Standard Institute (ANSI) standards (ANSI Z136.1-2007).[24] The system had a telecentric anterior eye imaging configuration with an f = 150 mm, 2" diameter lens. Retinal imaging required adding an adapter lens to collimate the incident beam on the eye and relay the beam scanning pivot point to the pupil. A dichroic mirror coupled a fixation target channel into the OCT beam scanning path. Light from a single pass reference arm and sample arm was interfered with a fiber coupler and the signal detected by a prototype high speed, dual-balanced InGaAs photodetector receiver PDB1 (custom prototype; Thorlabs Inc.). Signal from the dual-balanced photodetector was digitized by a high speed A/D converter. An additional trigger output from the programmable waveform generator served as a start signal for sweep acquisition (Figure 1a). Another prototype dual-balance photodiode PDB2 (custom prototype; Thorlabs Inc.) was used to detect interference fringes from the calibration MZI. A 12-bit 500 MSPS A/D converter (ATS9350; Alazar Technologies Inc.) was used for the retinal imaging mode. Both anterior segment and full eye length imaging required a faster sampling rate to support sufficient imaging

depth range. Accordingly, an 8-bit card 1GSPS A/D converter (ATS9870; Alazar Technologies Inc.) was used for anterior segment and full eye length imaging.

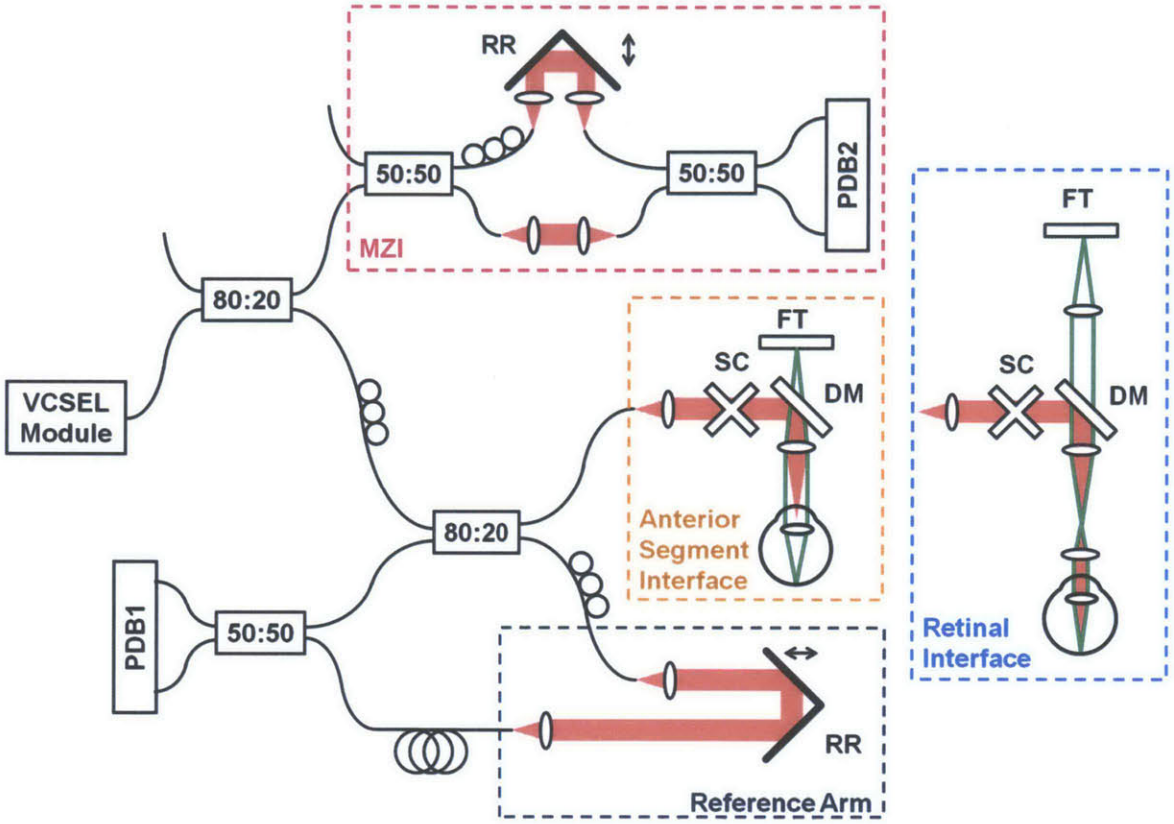

Figure 7.2 Ophthalmic VCSEL swept-source / Fourier domain OCT setup. Retinal imaging was performed by adding ocular lens to anterior segment configuration and adjusting the fixation target path. SC – galvanometric scanners, FT – fixation target, DM – dichroic mirror, DC – dispersion compensation glass, RR – retroreflector, PDB1/PDB2 – balanced photodetectors, MZI – Mach-Zehnder interferometer.[25]

The OCT system integrated multiple imaging modes in a single instrument. The operating modes included retinal imaging, anterior segment imaging and full eye length imaging. Details of the configuration and system performance for each operating mode are presented in Table 7.1. The effective axial scan rate was two times higher than MEMS VCSEL drive frequency if both forward and backward sweeps were acquired and processed (100% duty cycle). The VCSEL design allowed for adjustment of frequency / wavelength sweep range to modify imaging depth range and/or axial resolution.

Table 7.1 Configuration and performance of integrated SS-OCT system.[25]

Parameter	Retinal imaging			Anterior segment imaging	Full eye length imaging / ocular biometry
A/D acquisition card	ATS9350 (AlazarTech)			ATS9870 (AlazarTech)	ATS9870 (AlazarTech)
Detector bandwidth	330 MHz			1.5 GHz	1.5 GHz
Acquisition scheme	Forward sweep / Dual channel (OCT signal + MZI)		Dual sweep / Single channel	Forward sweep / Dual channel (OCT signal + MZI)	Forward sweep / Dual channel (OCT signal + MZI)
Clocking scheme	Internal clock			Internal clock	Internal clock
Clocking rate	500 MS/s			1 GS/s	1 GS/s
VCSEL tuning frequency	100 kHz	200 kHz	290 kHz	100 kHz	50 kHz
Effective A-scan rate	100 kHz	200 kHz	580 kHz	100 kHz	50 kHz
Acquired samples / sweep / channel	2048	896	1280	4096	7424
Wavelength tuning range	83 nm	83 nm	83 nm	85 nm	45 nm
Axial resolution*	9.0 μm	8.8 μm	8.9 μm	9.0 μm	12.4 μm
Transverse resolution	20 μm §	20 μm §	20 μm §	73 μm †	73 μm †
Imaging depth range*	6.8 mm	2.6 mm	1.9mm	13.6 mm	37.7 mm
Sensitivity	100.5 dB	97.4 dB	96.3 dB	98.8 dB	100.0 dB
-6-dB roll-off depth‡	6.8 mm	2.9 mm	2.2 mm	11.0 mm	39.0 mm

* in tissue (refractive index n=1.35); § estimated based on aberration-free model eye; † measured using a beam profiler; ‡ in air

Retinal imaging was performed using internally clocked A/D acquisition at 500 MSPS. Retinal imaging at sweep rates ranging from 100 kHz to 580 kHz were tested. Since the clock rate was fixed, increasing the axial scan rates resulted in a reduction of the imaging range (from 6.8 mm to 1.9 mm in tissue). In addition, faster imaging speeds resulted in lower sensitivity (decreasing from 100.5 dB at axial scan rates of 100 kHz to 96.3 dB at 580 kHz). The sensitivity was measured using 1.9 mW of optical power incident on a test mirror with a calibrated attenuator. Figure 7.3 shows sensitivity roll-off for the different operating modes. Similar to imaging depth range, the sensitivity -6-dB drop depth becomes shallower as the sweep rate increases. The axial image resolution was ~9 μm.

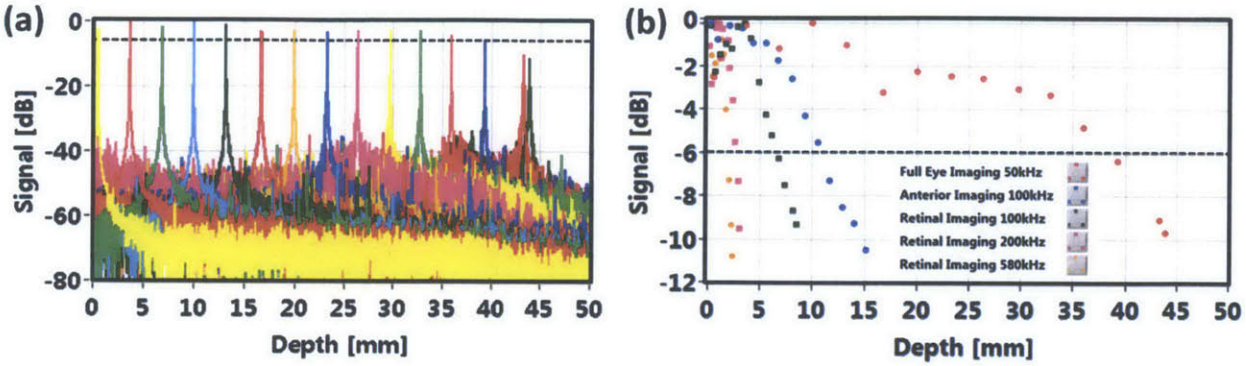

Figure 7.3 Sensitivity roll-offs of VCSEL-OCT system: (a) point spread functions at different depths in air for the full eye length imaging mode at 50 kHz, (b) signal roll-offs for different imaging modes. -6-dB signal drop is indicated by the dashed line.[25]

Anterior segment imaging required modification of the patient interface to telecentrically scan and focus the OCT beam onto the anterior chamber (Figure 7.2). The transverse resolution of this configuration was 73 μm. Since the anterior chamber and crystalline lens span a longer axial range than the retina, the imaging range must be extended by trading off axial resolution and/or reducing imaging speed. The anterior segment imaging mode operated at axial scan rates of 100 kHz using an A/D data acquisition card at a fixed 1 GSPS sampling rate with dual channel acquisition. Simultaneous acquisition of OCT signal and MZI fringes was required to calibrate of each laser sweep and account for sweep-to-sweep variation. The anterior segment imaging mode had a 13.6 mm imaging range in tissue and enabled visualizing ocular structures spanning the cornea to posterior surface of the crystalline lens. The axial resolution was 9 μm and the measured sensitivity was 98.8 dB, dropping by 6 dB at a depth of 11mm in air (Figure 7.3). Corneo-scleral imaging was performed using parameters analogous to those used for retinal imaging at 100 kHz axial scan rates.

Finally, full eye length imaging was performed at axial scan rates of 50 kHz. The data acquisition scheme was similar to that used for anterior segment imaging and the sweep range was reduced to 45nm in order to extend the imaging range to ~50mm in air (~38mm in tissue). This long imaging range enabled OCT imaging of the anterior segment and retina in a single dataset. The very long VCSEL coherence length and broad detection bandwidth supported a -6-dB signal roll-off at a 40 mm range in air (Figure 7.3). The OCT system sensitivity remained the same as in the 100 kHz retinal imaging mode. However, the reduced sweep range caused a decrease in axial resolution to 12 μm in tissue. Full eye length imaging is an extremely challenging operating mode because it requires long imaging range to visualize both anterior and retinal structures (minimum of 40 mm in air) as well as an optical focusing and scanning design to collect light from both the anterior segment and retina.

Refractive errors in the eye can make it difficult to simultaneously maximize collection efficiency from both anterior segment and retina. Imaging was performed using the anterior segment scanning configuration with a long focal length (f = 150 mm) ocular lens and a 73 μm incident spot size on the anterior segment of the eye. This provided sufficient depth of focus to image the anterior segment while normal ocular refraction produced focusing onto the retina. The beam spot size at the retina depended on the refraction status of the eye.

The procedures involving human subjects were approved by the Committee on Use of Humans as Experimental Subjects (COUHES) at MIT. The study was complaint with the tenets of the Declaration of Helsinki. Written informed consent was obtained prior to the study.

7.2.1 Retinal and Choroidal Imaging

Volumetric OCT datasets were acquired by raster scanning at sweep rates of 100 kHz, 200 kHz and 580 kHz. The images shown are from a 32 year old normal subject with myopia. Fundus views and corresponding cross-sectional images are shown in Figure 5. The transverse scan sampling density was kept constant at 12 μm per axial scan (~2× less than estimated spot size at the retina) by scaling the transverse scan area by the number of axial scans.

A total measurement time of ~2 seconds was used for each volume, consistent with a typical clinically acceptable acquisition time. The datasets comprised of 400 × 400, 600 × 600 and 1000 × 1000 axial scans and covered a scanned areas of 5 × 5 mm^2, 7 × 7 mm^2 and 12 × 12 mm^2 for sweep rates of 100 kHz, 200 kHz and 580 kHz, respectively. The scanned area at 100 kHz required separate acquisitions for the central macular region versus the optical nerve head (ONH), whereas imaging at 580 kHz enabled an almost six-fold increase in scanned field covering both macular and optical nerve head in a single dataset. All cross-sectional images in Figure 7.4 were cropped to show a depth of 1.5mm in tissue and the aspect ratio was kept constant. The 9 μm axial resolution enables visualization of the retinal layers. Enhanced light penetration at 1060 nm allowed imaging of the choroid.

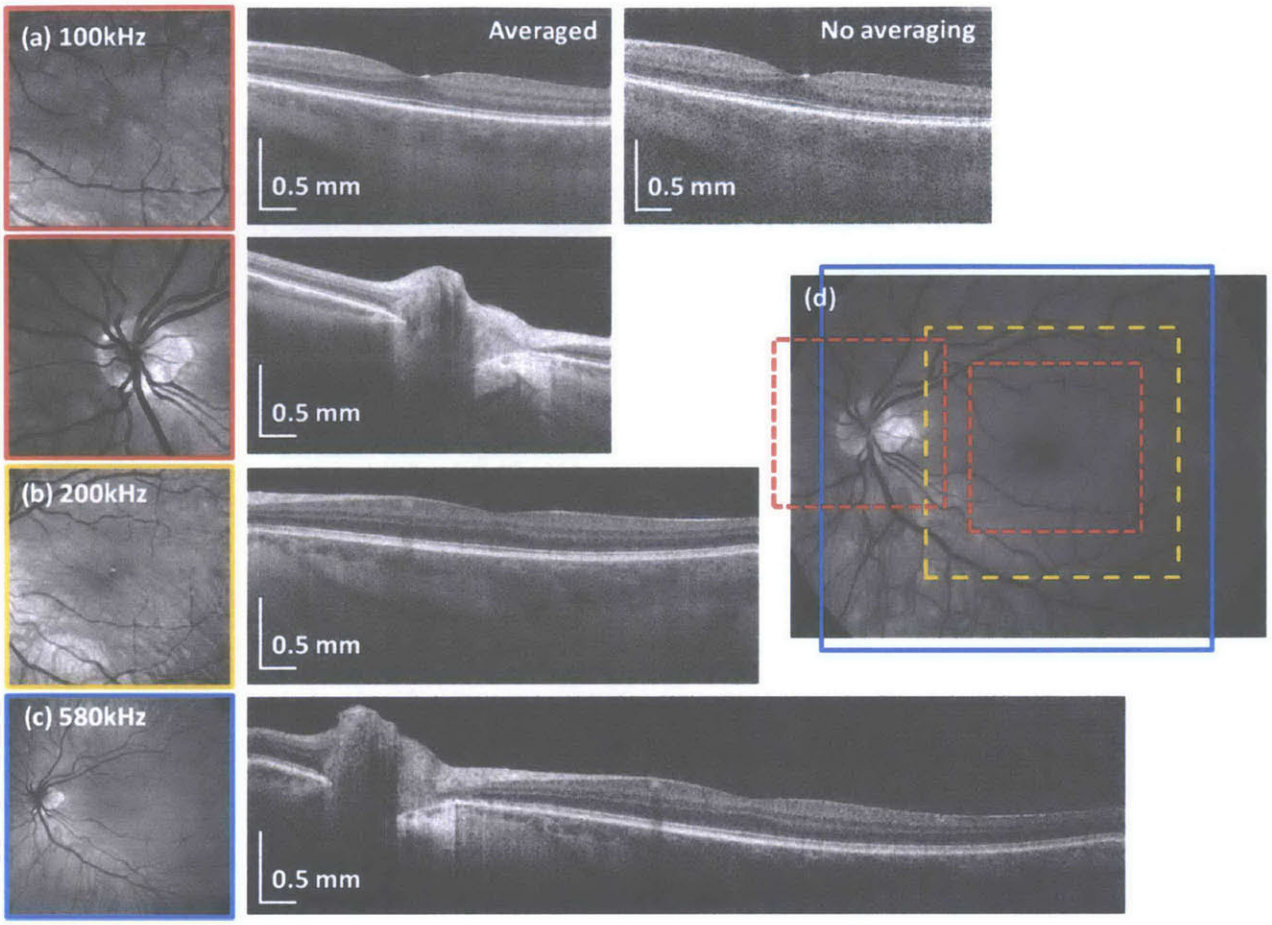

Figure 7.4 Retinal OCT imaging using VCSEL-tunable light source. Fundus images and selected cross-sections from volumetric datasets acquired at 100 kHz (a), 200 kHz (b) and 580 kHz (c). Red-free fundus photograph indicating scanned areas at different speeds (d). Transverse sampling density and acquisition time are kept constant. Aspect ratio of all presented cross-sections is the same. High speeds enable densely-scanned wide-field imaging.[25]

7.2.2 Anterior Segment Imaging

Anterior segment architecture can also be imaged using the longer imaging range, intermediate axial scan rate operating mode of the OCT instrument. Figure 7.5 shows a rendering of a volumetric dataset covering a 16 × 16 mm^2 area of the anterior eye. The volume consists of 500 × 500 axial scans and was acquired in 2.6 seconds. The cross-sectional image shows the cornea, iris and the entire crystalline lens and spans the entire transverse anterior chamber width, from limbus to limbus. The cross-sectional image in Figure 7.5(b) is generated by averaging 5 consecutive B-scans to enhance signal to noise. Zoomed inserts show corneal sublayers such as the epithelium, Bowman's membrane, stroma and endothelium (Figure 7.5(c)).

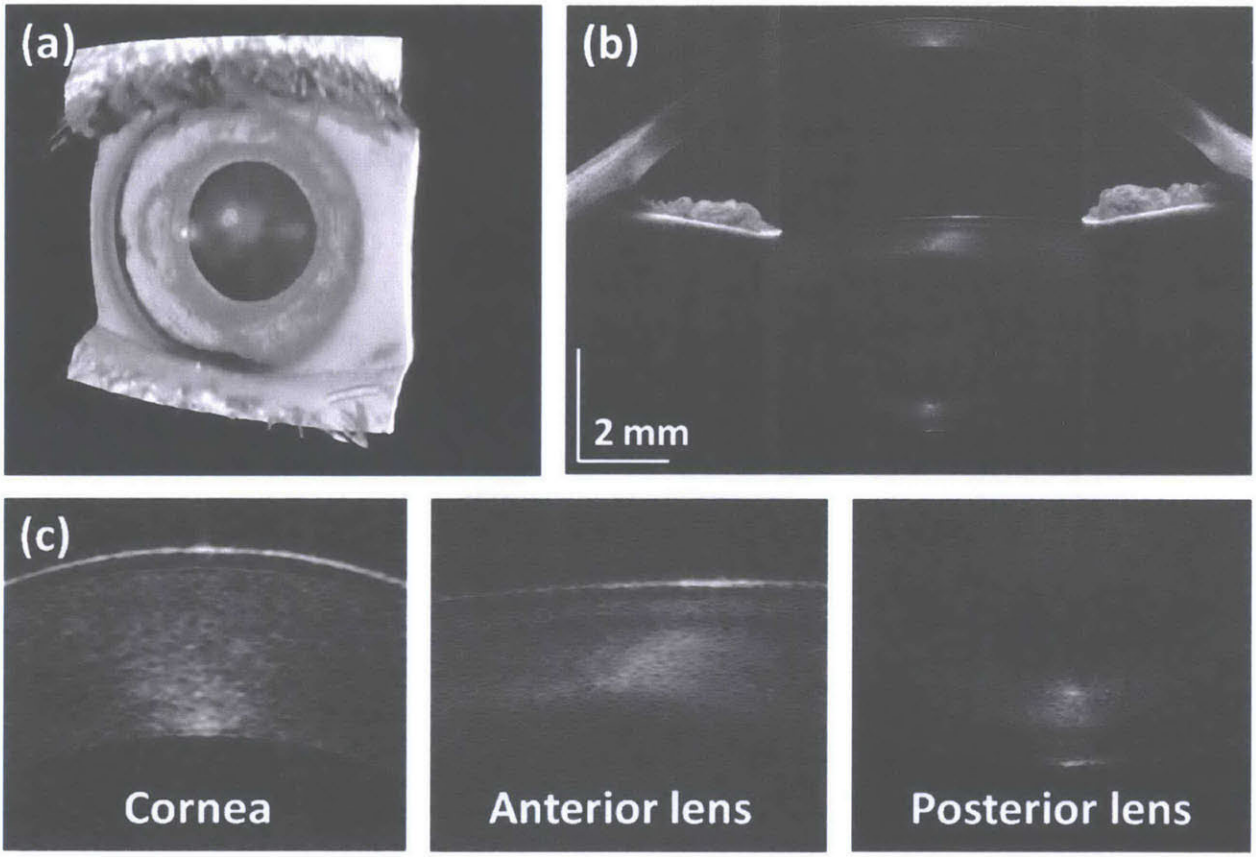

Figure 7.5 Anterior segment imaging with VCSEL-OCT: (a) rendering of the volume, (b) central averaged cross-sectional image, (c) zoomed fragments of the B-scan showing details of the corneal and the crystalline lens.[25]

7.2.3 Full Eye Length Imaging and Axial Eye Length Measurement

Intraocular distances such as axial eye length or anterior chamber depth are parameters that are essential for accurate intraocular lens (IOL) calculation. The long imaging range needed to span axial eye length was achieved by reducing the laser sweep range, trading off axial resolution. Imaging was performed on a normal subject with myopia (-7 diopters). The left eye was scanned over 15x15mm^2 area with 350×350 axial scans with an acquisition time of 2.6 seconds. Figure 7.6(a) shows a rendering of the full eye from the cornea to the retina. This was the first demonstration of 3D full eye length imaging using OCT.

Figure 7.6(b) shows a selected cross-sectional image spanning the entire eye from anterior chamber and crystalline lens to the retina. The components of the eye introduce dispersion mismatch. Therefore, the retinal signal was dispersion corrected in post-processing by selecting the bottom part of the image using a Heaviside function, and inverse Fourier transforming back into frequency or wavenumber. The argument of Heaviside step function was a pixel depth position close to the retinal signal. The dispersion correction coefficients were then selected, the spectral signal was phase corrected and Fourier transformed. The anterior segment and retinal signals were merged to create a final B-scan where the anterior and retinal signal had separate dispersion compensation parameters. Because the OCT beam is refracted towards the fovea as it propagates to the retina, the effective scanning area becomes smaller with increasing depth. Ultimately the retinal signal in Figure 7.6 came from nearly a single point on the fundus (if there were no aberrations or motion during acquisition). A star-like pattern in the crystalline lens was visible in the 3D reconstruction (Figure 7.6(a)) and en face view (Figure 7.6b) which comes from the sutures of the lens. The depth profile shown in Figure 7.6(c) is an averaged axial scan from the central 100 axial scans (central 10 × 10 axial scan square). This enables measurement of intraocular distances after correcting for the refractive index of each ocular component. The axial resolution was 12 μm over almost 40 mm in tissue. The intensity peaks in Figure 7.6(c) can be identified as the reflections from the anterior and posterior surfaces of the cornea, anterior and posterior interfaces of the crystalline lens, and retina. The standard measurement of axial eye length requires finding the distance between corneal vertex and RPE/Bruch's membrane.

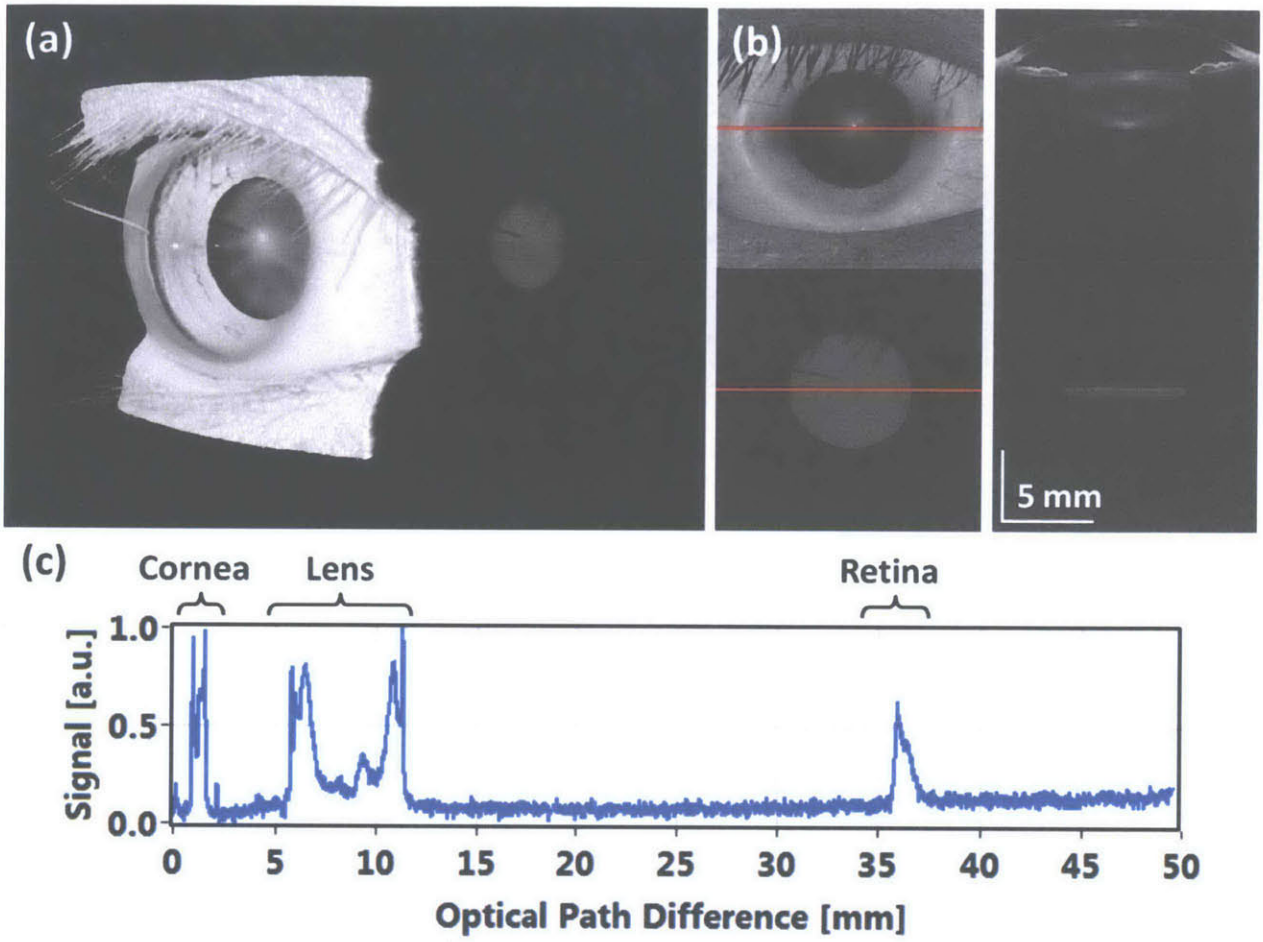

Figure 7.6 Full eye length imaging with ultralong depth range OCT: (a) 3D rendering of volumetric dataset, (b) central cross-sectional image, (c) central B-scan extracted from dataset corrected for light refraction, (d) central depth profile with echoes from the cornea, crystalline lens and the retina allows for determination of intraocular distances.[25]

7.3 Four-Dimensional Imaging Using VCSEL Swept-Source / Fourier Domain OCT

In this section, time resolved volumetric data using four-dimensional (4D) OCT with speeds up to forty volumes per second is demonstrated to image pupillary reactions, anterior eye focusing dynamics, tear film break up, and retinal blood flow. The real-time dynamics of the human eye is captured and analyzed for characterizing visual functions.

The VCSEL light source based prototype SS-OCT system described in 7.2 was used. The laser was operated in four different modes with center wavelengths at around 1060 nm (Table 7.2). To image the pupillary reaction, the VCSEL light source was operated at an axial scan rate of 200 kHz with 85 nm tuning range yielding 9 μm resolution and 5.6 mm Nyquist-limited imaging range in tissue. To image

anterior eye accommodation dynamics, the axial scan rate was reduced to 100 kHz to achieve a 10.3 mm Nyquist-limited imaging range in tissue. To image tear film break up, the VCSEL light source was operated at a reduced axial scan rate of 50 kHz and reduced 30 nm tuning range for 19 μm resolution and 60 mm Nyquist-limited imaging range in tissue. Finally, to image retinal blood flow, the VCSEL light source was operated at an axial scan rate of 800 kHz and 50 nm tuning range for 12 μm resolution and 2.5mm Nyquist-limited imaging range in tissue. A/D data acquisition cards (ATS9870 & ATS9350; AlazarTech) at either a fixed 1 GSPS or a fixed 500 MSPS sampling rate with dual channel acquisition were used. The incident power on the cornea for all imaging modes was 1.9 mW, within the American National Standard Institute (ANSI) safety limits.

Table 7.2 Configuration of VCSEL SS-OCT system for 4D imaging.[29]

Parameter	Pupillary response	Accommodation	Tear film break up	Retinal blood flow
Effective imaging speed	200,000 A-scans/s	100,000 A-scans/s	50,000 A-scans/s	800,000 A-scans/s
Wavelength tuning range	85 nm	85 nm	30 nm	50 nm
Axial resolution (tissue)	9 μm	9 μm	19 μm	12 μm
Sample arm interface	Anterior segment	Anterior segment	Full eye length	Retinal
Transverse resolution	30 μm	30 μm	73 μm	25 μm
Acquisition card	ATS9870 (1 GSPS)	ATS9870 (1 GSPS)	ATS9870 (1 GSPS)	ATS9350 (500 MSPS)

7.3.1 Pupillary Reflex

The iris is a dynamic structure whose configuration regularly changes in response to light and during accommodation. Dynamic changes in intraocular structures caused by illumination or dilation are suggested to be risk factors for glaucoma development. Studying the dynamic response of the pupil to dark-light stimulus may provide a more comprehensive assessment of risks to primary-angle closure development and may help understand the pathophysiology of angle closure glaucoma.[26-28] We demonstrated 4D imaging of the pupil response to light stimulus from an LED positioned adjacent to the eye, where sequential 150 × 150 axial-scan volumes over 17 mm × 17 mm were acquired at ~8 volumes per second for 5 seconds with an axial scan rate of 200 kHz enabling the visualization of changes in the iris in time and in three dimensions. The pupillary response is shown in Figure 7.7 where two time points in the 4D data are displayed. The iris response to light stimulus can be quantitatively analyzed by measuring pupil size/area changes in time. As shown in Figure 7.7(A), the pupil area decreased drastically when light stimulus was applied. In contrast, the time constant of the pupil diameter recovery was longer than when stimulus was applied.

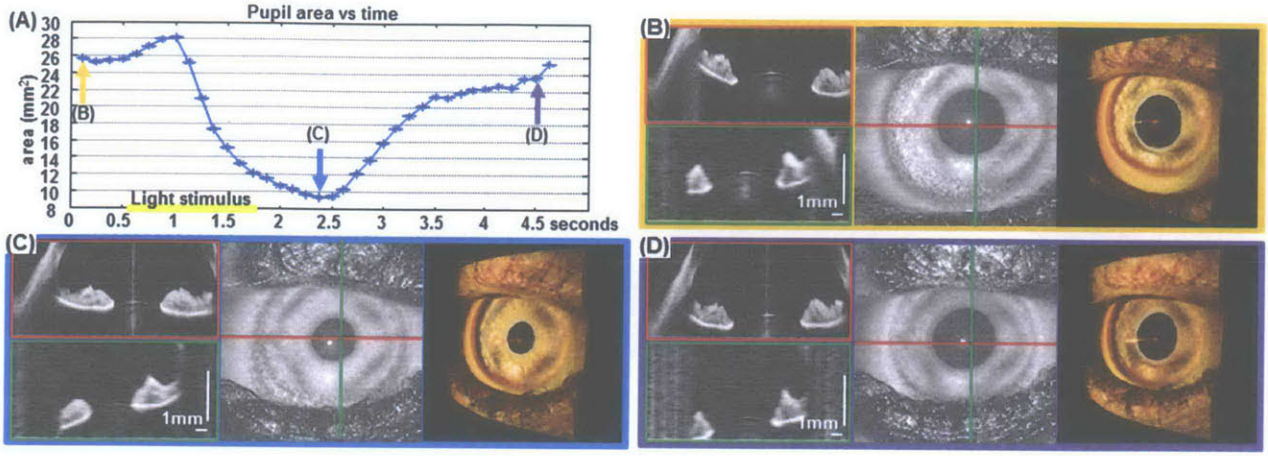

Figure 7.7 4D OCT imaging of the pupillary reflex. (A) Plot of pupil area vs time. (B) Volume#1 at 0.13 seconds. (C) Volume#19 at 2.38 seconds. (D) Volume#38 at 4.5 seconds. The constriction of the iris and the decrease in pupil area is apparent when comparing volume#1 and volume#19. The dilation of the iris and increase in pupil area is visible when comparing volume#19 and volume #38. The cross-sectional OCT images show the iris structure while the enface OCT image depicts the pupil area.[29]

7.3.2 Accommodation Dynamics

In the anterior eye, accommodation is the process by which the eye focuses on near objects. This occurs mainly through the deformation of the crystalline lens geometry. Studies of the dynamics of far to near focusing processes may enable understanding several aspects like the age-dependent loss of accommodative amplitude in presbyopia, the development of myopia, and the ageing of the crystalline lens as well as the mechanism of accommodation.[30] We performed 4D imaging of the focusing process in the anterior eye acquiring 100 × 100 axial-scan volumes over 15 mm × 15 mm at ~10 volumes per second for 5 seconds at an axial scan rate of 100 kHz. The target was moved in position from far to near and the subject was asked to focus on the target and accommodate the target's position change. Two time points are shown from the 4D data in Figure 7.8. Pupil diameter decreases when the eye focuses at near positions. The iris becomes smaller while the crystalline lens becomes thicker with surfaces curvature changes.

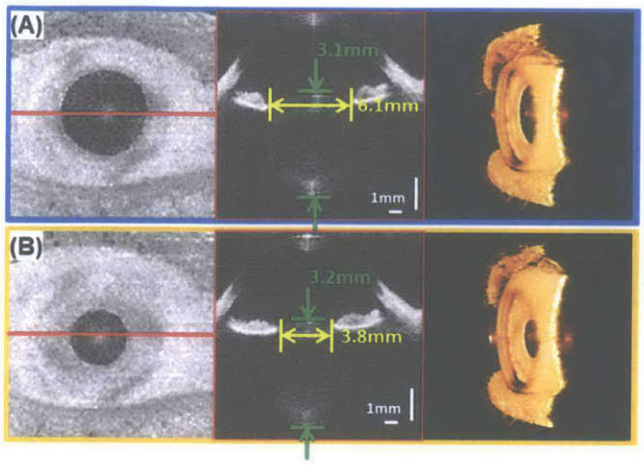

Figure 7.8 4D OCT imaging of the anterior eye focusing on a near object. A) Volume#5 at 0.5 seconds. B) Volume #30 at 3 seconds. The decrease in pupil size and increase in lens thickness is observed and measured.[29]

7.3.3 Tear Film Break Up

The tear film is the first refractive surface for light incident on the eye and plays an important role in the optical quality of the human eye. Tear film dynamics has been used to evaluate the tear system and diagnose dry eye. Tear film break up time (TBUT) is defined as the time interval between a complete blink and the appearance of the first randomly distributed dry spot.[31] A TBUT of less than ten seconds is considered abnormal.[32] Fluorescein dye is typically used for clinical TBUT measurements. OCT allows for non-invasive tear film dynamics imaging without the need of fluorescein staining. We implemented a 4D scan protocol with 300 × 300 axial-scan volumes over 8.5 mm × 8.5 mm at ~0.5 volumes per second for 20 seconds at an axial scan rate of 50 kHz. In order to best visualize tear film break up, we examine the shadowing effect by summing the signal between the anterior surface and the posterior surface of the crystalline lens. Tear film break up can be clearly observed in the frame-by-frame breakdown (Figure 7.9).

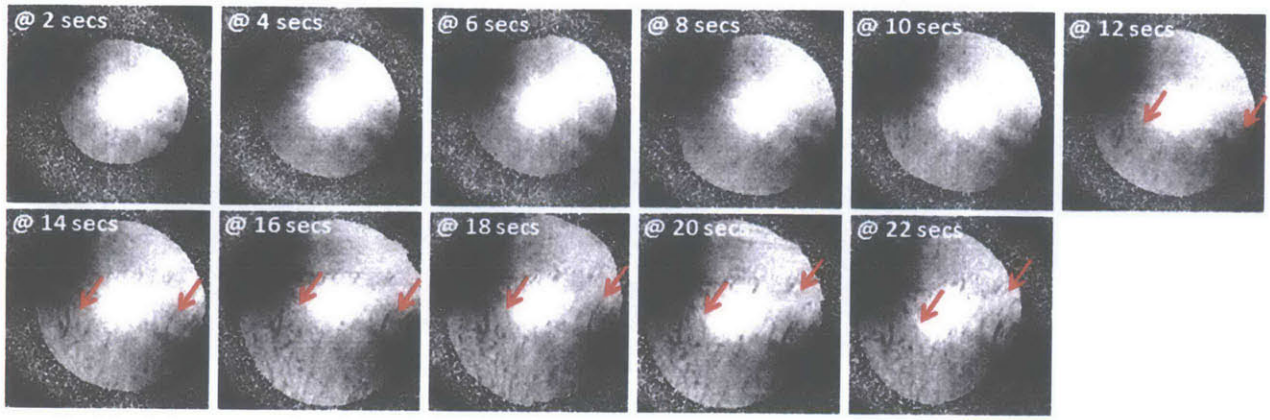

Figure 7.9 Tear film break up observed in enface images extracted from 4D OCT data. Tear film break up is observed beginning at ~12 seconds where vertical streaking patterns appear.[29]

7.3.4 Retinal Blood Flow

Retinal blood flow may play a role in the pathogenesis of diseases such as diabetic retinopathy, age-related macular degeneration, and glaucoma. The ability to monitor retinal blood flow may be important not only for treatment, but also for understanding the pathophysiology of these diseases.[33-35] We acquired 4D data in the retina with 200 × 100 axial-scan volumes over 1 mm × 0.5 mm at ~40 volumes per second for 1 second at an axial scan rate of 800 kHz. Since the galvanometer scanners are driven at very high speeds, a conservative flyback pattern is chosen resulting in only a 0.5 mm × 0.5 mm evenly sampled region. Images from a single time point is extracted and shown in Figure 7.10(B)(C)(D). By taking the variance of maximum intensity projection images at all time points from multiple volumes, we are able to visualize capillaries from the inner to the outer plexiform layers (Figure 7.10(E)).

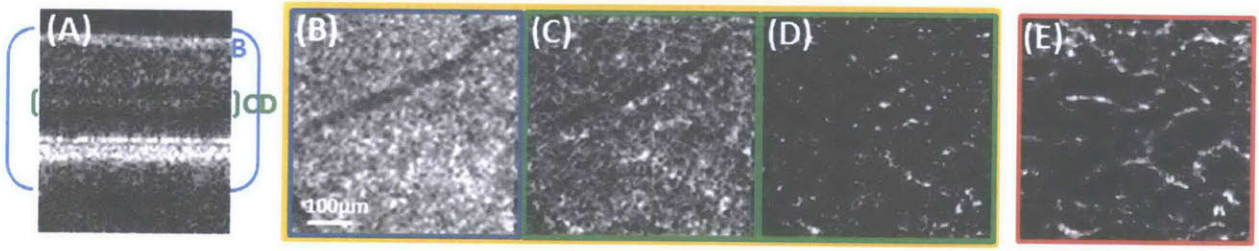

Figure 7.10 4D OCT imaging of retinal blood flow. A) Cross-sectional OCT image. B) Enface summation image in the axial direction of a single volume. C) Enface summation image of a region of interest in the axial direction of a single volume. D) Maximum projection image of a region of interest in the axial direction of a single volume. E) Variance image generated from maximum projection images (like E) of multiple volumes in the 4D data. The maximum projection image from a single volume shows moving highly reflective scatters. The variance image generated from multiple volumes highlight retinal capillaries.[29]

7.4 References

1. Chinn SR, Swanson EA, Fujimoto JG. Optical coherence tomography using a frequency-tunable optical source. Opt Lett. 1997;22(5):340-2. PubMed PMID: ISI:A1997WJ76500029.

2. Golubovic B, Bouma BE, Tearney GJ, Fujimoto JG. Optical frequency-domain reflectometry using rapid wavelength tuning of a Cr4+:forsterite laser. Opt Lett. 1997;22(22):1704-6. PubMed PMID: ISI:A1997YF19400015.

3. Yun SH, Boudoux C, Tearney GJ, Bouma BE. High-speed wavelength-swept semiconductor laser with a polygon-scanner-based wavelength filter. Opt Lett. 2003;28(20):1981-3. PubMed PMID: ISI:000185746300041.

4. Yun SH, Boudoux C, Pierce MC, de Boer JF, Tearney GJ, Bouma BE. Extended-cavity semiconductor wavelength-swept laser for biomedical imaging. IEEE Photonics Technol Lett. 2004;16(1):293-5.

5. Yasuno Y, Madjarova VD, Makita S, Akiba M, Morosawa A, Chong C, Sakai T, Chan KP, Itoh M, Yatagai T. Three-dimensional and high-speed swept-source optical coherence tomography for in vivo investigation of human anterior eye segments. Optics Express. 2005;13(26):10652-64. PubMed PMID: ISI:000234263000022.

6. Choma MA, Hsu K, Izatt JA. Swept source optical coherence tomography using an all-fiber 1300-nm ring laser source. J Biomed Opt. 2005;10(4):no. 044009 PubMed PMID: ISI:000232799200019.

7. Huber R, Wojtkowski M, Taira K, Fujimoto JG, Hsu K. Amplified, frequency swept lasers for frequency domain reflectometry and OCT imaging: design and scaling principles. Optics Express. 2005;13(9):3513-28. PubMed PMID: ISI:000228896200038.

8. Goldberg BD, Vakoc BJ, Oh WY, Suter MJ, Waxman S, Freilich MI, Bouma BE, Tearney GJ. Performance of reduced bit-depth acquisition for optical frequency domain imaging. Optics Express. 2009;17(19):16957-68. PubMed PMID: ISI:000269736100066.

9. Okabe Y, Sasaki Y, Ueno M, Sakamoto T, Toyoda S, Yagi S, Naganuma K, Fujiura K, Sakai Y, Kobayashi J, Omiya K, Ohmi M, Haruna M. 200 kHz swept light source equipped with KTN deflector for optical coherence tomography. Electron Lett. 2012;48(4):201-2. doi: Doi 10.1049/El.2011.4057. PubMed PMID: ISI:000300605700006.

10. Huber R, Wojtkowski M, Fujimoto JG. Fourier Domain Mode Locking (FDML): A new laser operating regime and applications for optical coherence tomography. Optics Express. 2006;14(8):3225-37. PubMed PMID: ISI:000237144700014.

11. Oh WY, Vakoc BJ, Shishkov M, Tearney GJ, Bouma BE. > 400 kHz repetition rate wavelength-swept laser and application to high-speed optical frequency domain imaging. Opt Lett. 2010;35(17):2919-21. PubMed PMID: ISI:000281522700031.

12. Wieser W, Biedermann BR, Klein T, Eigenwillig CM, Huber R. Multi-Megahertz OCT: High quality 3D imaging at 20 million A-scans and 4.5 GVoxels per second. Optics Express. 2010;18(14):14685-704. PubMed PMID: ISI:000279639900041.

13. Amano T, Hiro-Oka H, Choi D, Furukawa H, Kano F, Takeda M, Nakanishi M, Shimizu K, Ohbayashi K. Optical frequency-domain reflectometry with a rapid wavelength-scanning superstructure-grating distributed Bragg reflector laser. Appl Optics. 2005;44(5):808-16. doi: Doi 10.1364/Ao.44.000808. PubMed PMID: ISI:000227154400020.

14. Liu AQ, Zhang XM. A review of MEMS external-cavity tunable lasers. J Micromech Microeng. 2007;17(1):R1-R13. doi: Doi 10.1088/0960-1317/17/1/R01. PubMed PMID: ISI:000242825800001.

15. Fujiwara N, Yoshimura R, Kato K, Ishii H, Kano F, Kawaguchi Y, Kondo Y, Ohbayashi K, Oohashi H. 140-nm quasi-continuous fast sweep using SSG-DBR lasers. IEEE Photonics Technol Lett. 2008;20(9-12):1015-7. doi: 10.1109/lpt.2008.923544. PubMed PMID: WOS:000256966100114.

16. Potsaid B, Baumann B, Huang D, Barry S, Cable AE, Schuman JS, Duker JS, Fujimoto JG. Ultrahigh speed 1050nm swept source/Fourier domain OCT retinal and anterior segment imaging at 100,000 to 400,000 axial scans per second. Opt Express. 2010;18(19):20029-48. Epub 2010/10/14. doi: 10.1364/OE.18.020029 205532 [pii]. PubMed PMID: 20940894; PubMed Central PMCID: PMC3136869.

17. Totsuka K, Isamoto K, Sakai T, Morosawa A, Chong CH. MEMS scanner based swept source laser for optical coherence tomography. P Soc Photo-Opt Ins. 2010;7554. doi: Artn 75542q Doi 10.1117/12.841528. PubMed PMID: ISI:000285578400058.

18. Minneman MP, Ensher J, Crawford M, Derickson D. All-Semiconductor High-Speed Akinetic Swept-Source for OCT. Optical Sensors and Biophotonics Iii. 2011;8311. doi: Artn 831116 Doi 10.1117/12.912119. PubMed PMID: ISI:000298372300031.

19. Jayaraman V, Jiang J, Li H, Heim PJS, Cole GD, Potsaid B, Fujimoto JG, Cable A, editors. OCT imaging up to 760 kHz axial scan rate using single-mode 1310nm MEMS-tunable VCSELs with >100nm tuning range. Lasers and Electro-Optics (CLEO), 2011 Conference on; 2011 1-6 May 2011.

20. Potsaid B, Jayaraman V, Fujimoto JG, Jiang J, Heim PJS, Cable AE. MEMS tunable VCSEL light source for ultrahigh speed 60kHz-1MHz axial scan rate and long range centimeter class OCT imaging. Proc SPIE 8213, Optical Coherence Tomography and Coherence Domain Optical Methods in Biomedicine XVI. 2012. doi: 10.1117/12.911098. PubMed PMID: ISI:000302605000010.

21. Jayaraman V, Jiang J, Potsaid B, Cole G, Fujimoto J, Cable A. Design and performance of broadly tunable, narrow line-width, high repetition rate 1310nm VCSELs for swept source optical coherence tomography. Vertical-Cavity Surface-Emitting Lasers Xvi. 2012;8276. doi: Artn 82760d Doi 10.1117/12.906920. PubMed PMID: ISI:000300250900012.

22. Jayaraman V. MEMS-based VCSEL reaches record 150 nm tuning range. Laser Focus World. 2012;48(9):10-. PubMed PMID: ISI:000308970700004.

23. Jayaraman V, Potsaid B, Jiang J, Cole GD, Robertson ME, Burgner CB, John DD, Grulkowski I, Choi W, Tsai TH, Liu J, Stein BA, Sanders ST, Fujimoto JG, Cable AE. High-speed ultra-broad tuning

MEMS-VCSELs for imaging and spectroscopy. Smart Sensors, Actuators, and Mems Vi. 2013;8763. doi: Unsp 87630h Doi 10.1117/12.2018345. PubMed PMID: ISI:000323607500016.

24. American National Standard for Safe Use of Lasers, ANSI Z136.1. New York: American National Standards Institute; 2007.

25. Grulkowski I, Liu JJ, Potsaid B, Jayaraman V, Lu CD, Jiang J, Cable AE, Duker JS, Fujimoto JG. Retinal, anterior segment and full eye imaging using ultrahigh speed swept source OCT with vertical-cavity surface emitting lasers. Biomedical optics express. 2012;3(11):2733-51. PubMed PMID: ISI:000310644700005.

26. Leung CKS, Cheung CYL, Li H, Dorairaj S, Yiu CKF, Wong AL, Liebmann J, Ritch R, Weinreb R, Lam DSC. Dynamic analysis of dark-light changes of the anterior chamber angle with anterior segment OCT. Investigative Ophthalmology & Visual Science. 2007;48(9):4116-22. PubMed PMID: ISI:000249061900030.

27. Cheung CYL, Liu S, Weinreb RN, Liu J, Li HT, Leung DYL, Dorairaj S, Liebmann J, Ritch R, Lam DSC, Leung CKS. Dynamic Analysis of Iris Configuration with Anterior Segment Optical Coherence Tomography. Investigative Ophthalmology & Visual Science. 2010;51(8):4040-6. doi: Doi 10.1167/Iovs.09-3941. PubMed PMID: ISI:000280194100031.

28. Lee Y, Sung KR, Na JH, Sun JH. Dynamic changes in anterior segment (AS) parameters in eyes with primary angle closure (PAC) and PAC glaucoma and open-angle eyes assessed using AS optical coherence tomography. Invest Ophthalmol Vis Sci. 2012;53(2):693-7. Epub 2012/01/10. doi: 10.1167/iovs.11-8389 [pii]. PubMed PMID: 22222269.

29. Liu JJ, Grulkowski I, Potsaid B, Jayaraman V, Cable AE, Kraus MF, Hornegger J, Duker JS, Fujimoto JG. 4D dynamic imaging of the eye using ultrahigh speed SS-OCT. Proc SPIE 8567, Ophthalmic Technologies XXIII. 2013. doi: 10.1117/12.2004369.

30. Ruggeri M, Uhlhorn SR, De Freitas C, Ho A, Manns F, Parel JM. Imaging and full-length biometry of the eye during accommodation using spectral domain OCT with an optical switch. Biomed Opt Express. 2012;3(7):1506-20. Epub 2012/07/19. doi: 10.1364/BOE.3.001506 166403 [pii]. PubMed PMID: 22808424; PubMed Central PMCID: PMC3395477.

31. Lemp MA, Hamill JR, Jr. Factors affecting tear film breakup in normal eyes. Arch Ophthalmol. 1973;89(2):103-5. Epub 1973/02/01. PubMed PMID: 4683600.

32. Lemp MA, Dohlman CH, Kuwabara T, Holly FJ, Carroll JM. Dry eye secondary to mucus deficiency. Trans Am Acad Ophthalmol Otolaryngol. 1971;75(6):1223-7. Epub 1971/11/01. PubMed PMID: 5151803.

33. Baumann B, Potsaid B, Kraus MF, Liu JJ, Huang D, Hornegger J, Cable AE, Duker JS, Fujimoto JG. Total retinal blood flow measurement with ultrahigh speed swept source/Fourier domain OCT. Biomed Opt Express. 2011;2(6):1539-52.

34. Jia YL, Morrison JC, Tokayer J, Tan O, Lombardi L, Baumann B, Lu CD, Choi W, Fujimoto JG, Huang D. Quantitative OCT angiography of optic nerve head blood flow. Biomedical optics express. 2012;3(12). PubMed PMID: ISI:000312709500008.

35. Choi W, Baumann B, Liu JJ, Clermont AC, Feener EP, Duker JS, Fujimoto JG. Measurement of pulsatile total blood flow in the human and rat retina with ultrahigh speed spectral/Fourier domain OCT. Biomedical Optics Express. 2012;3(5):1047-61. PubMed PMID: ISI:000303537400019.

CHAPTER 8

Future Work and Outlook

8.1 Quantitative Doppler OCT

Dr. Bernhard Baumann from our group has reported total retinal blood flow measurements in the retina using an en face Doppler OCT method.[1] Using a 200,000 axial scan per second swept-source / Fourier domain OCT prototype system, dense three-dimensional sampling of the retina near the optic nerve head enables for en face measurement of retinal blood flow. In addition, the reduced fringe washout using swept-source / Fourier domain OCT and the high axial scan rate enables better detection of high flow velocities, while the 1 μm wavelength range provides deeper penetration into tissue to provide access to vessels near the central retinal artery and vein. Figure 3.1 illustrates and compares the en face Doppler OCT method with conventional Doppler OCT methods for measuring flow. By measuring the Doppler OCT velocities at the en face plane, the requirement of measuring the vessel angle no longer exists.

Using the en face Doppler OCT method, total retinal blood flow can be estimated as shown in Figure 3.2 where the blood flow in each artery and vein near the optic nerve head is measured individually. However, since the acquisition time for the volume is longer than a cardiac pulse cycle, the measurement remains susceptible to error due to pulsatility. Time resolved volumetric imaging can be achieved with even higher OCT imaging speeds, which was later demonstrated by WooJhon Choi from our group in a later paper performing Doppler OCT measurements of pulsatile blood flow in both human and rat eyes.[2]

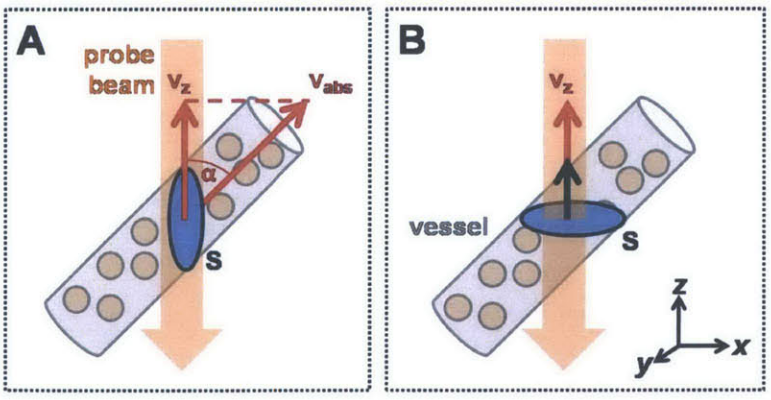

Figure 8.1 En face Doppler OCT flow measurement. (A) In conventional Doppler methods, the angle α between the vessel and the OCT beam is measured to compute absolute velocity. Total flow can then be calculated with the measurement of the cross-sectional area of the vessel. (B) In the En face Doppler OCT method, total flow is calculated by integrating the axial velocity components in the surface whose normal vector is parallel to the OCT beam.[1]

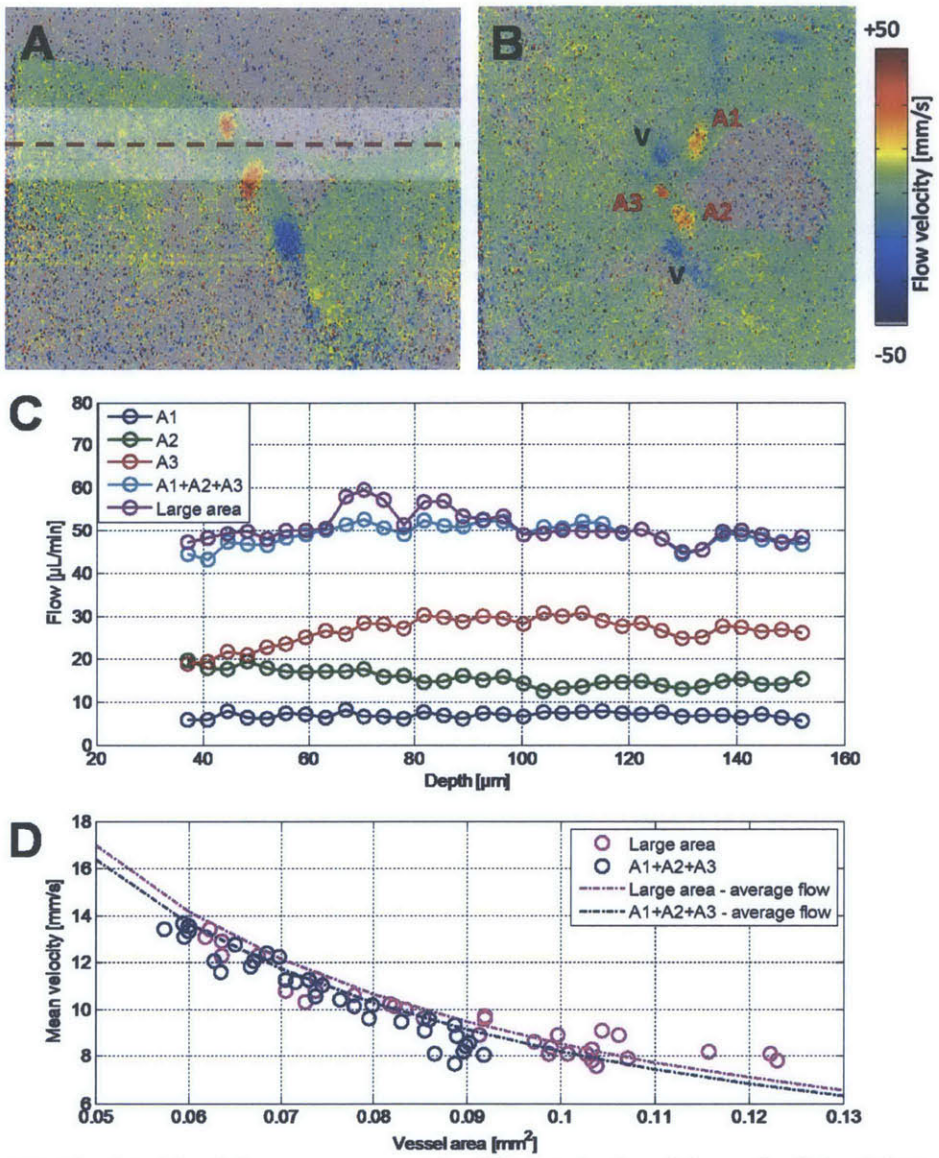

Figure 8.2 Absolute blood flow measurement in different depths of the optic disk. (A) Doppler B-scan image. The depth range in which en face flow measurements were performed is indicated; the dashed line shows the location of image (B). (B) En face Doppler image. Cross sections of central retinal arteries labeled A1 – A3 and veins (V) can be observed. (C) Blood flow measured at different depths in A1 – A3 and total arterial blood flow computed by summing the flow values retrieved for the single retinal arteries (A1+A2+A3) as well as by integrating blood flow towards the OCT beam in a large area covering all vessels. (D) Relationship between total vessel area and mean flow velocity. Each magenta and cyan circle indicates one depth-resolved flow measurement for evaluating the large area and for summing the single vessel measurements, respectively. The expected relations assuming the average flow are plotted as dash-dotted lines for the respective measurements.[1]

8.2 OCT Angiography

Dr. Yali Jia and our collaborators at the Oregon Health Science University developed an OCT angiography method known as split-spectrum amplitude-decorrelation angiography (SSADA)[3] using the swept-source / Fourier domain OCT system developed at MIT described in Chapter 5. Similar to other OCT angiography methods, SSADA takes advantage of the high imaging speeds of Fourier domain OCT to perform repeated scanning of cross-sections with in a three-dimensional dataset to extract scattering changes due to blood flow through examining the decorrelation between repeated scans. Figure 8.3 and Figure 8.4 show SSADA imaging of the optic nerve head and macular regions, respectively.

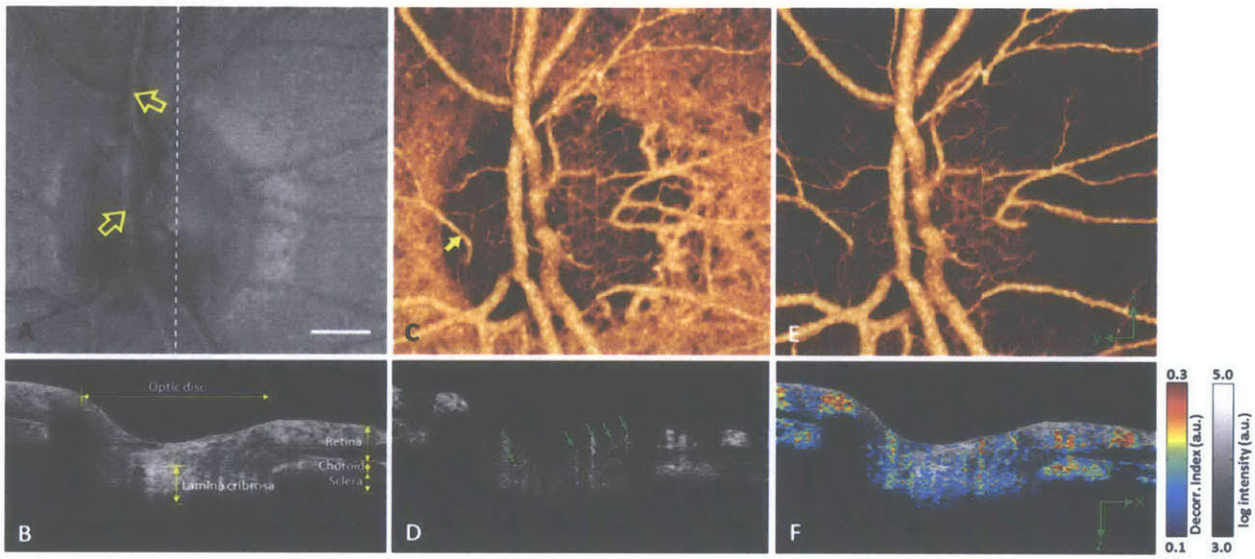

Figure 8.3 In vivo 3D-OCT of the optic nerve head over a 3 mm × 3 mm region on the retina. (A) En face maximum reflectance intensity projecti0on shows branches of the central retinal artery and vein (yellow arrows point to superior branches). (B) OCT cross section at the plane marked by white dash in (A). (C) En face maximum decorrelation projection angiogram computed with the SSADA algorithm. It shows many orders of branching from the central retinal artery and vein, a dense capillary network shows in the disc, a cilioretinal artery (yellow arrow), and a near continuous sheet of choroidal perfusion around the disc. (D) Decorrelation cross section (same plane as B) shows blood flow in disc vessels (green arrows), peripapillary retinal vessels, and choroid. (E) En face maximum decorrelation projection angiogram after removing the choroid (pixels below the level retinal pigment epithelium). (F) Overlayed cross-sectional image where flow (color scale representing decorrelation) is merged with structure (gray scale representing reflectance intensity) shows how the disc, retina, and choroid are perfused. Scale bar: 500μm.[3]

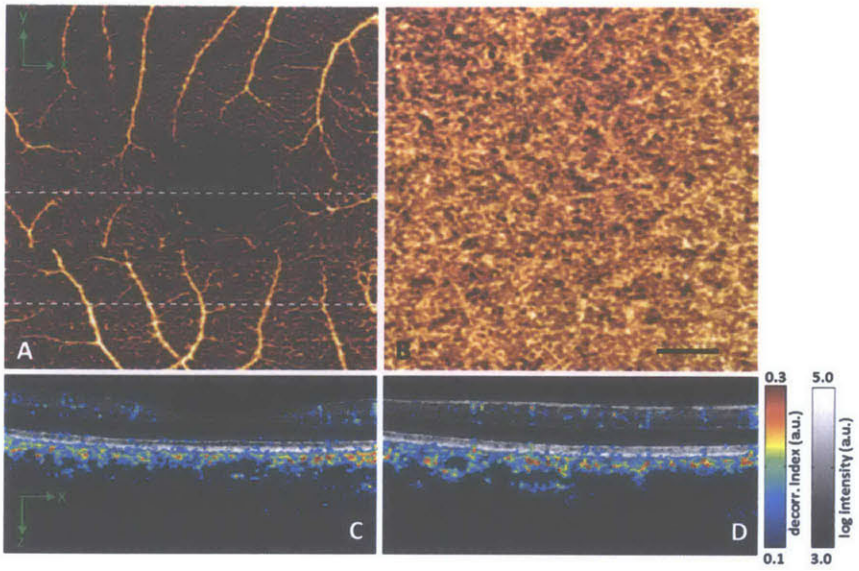

Figure 8.4 In vivo 3D volumetric (3.0 (x) ×3.0 (y) ×2.9 (z) mm) OCT of the macula processed with the SSADA algorithm. (A) En face maximum decorrelation projection angiogram of the retinal circulation. (B) En face maximum decorrelation projection angiogram of the choroidal circulation. (C) Horizontal OCT cross section through the foveal center (dotted line in center of A) with merged flow (decorrelation represented in color scale) and structure (reflectance intensity represented in gray scale) information. (D) Merged horizontal cross section of the inferior macula (dotted line below center of A). Scale bar: 500μm.[3]

8.3 Future Clinical Studies with Ultrahigh Speed OCT

In a team effort between WooJhon Choi, ByungKun Lee, Chen Lu, and myself, our group has recently deployed a VCSEL swept-source / Fourier domain OCT system with 400,000 axial scan per second imaging speed to the New England Eye Center. In addition to structural imaging with high density scanning, the high imaging speed will enable measurement of pulsatile retinal blood flow as well as OCT angiography. Figure 8.5 is a schematic of the system which includes optical clocking and a fiber Bragg grating for phase stabilization, Mach-Zehnder interferometer for clock signal generation, and spectrometer for monitoring the VCSEL status and controls feedback.

Diseases such as diabetic retinopathy, age-related macular degeneration, and glaucoma are related to changes in vascular structure and blood flow in the eye. The new clinical VCSEL swept-source / Fourier domain OCT system will enable imaging and analysis of blood flow and vasculature.

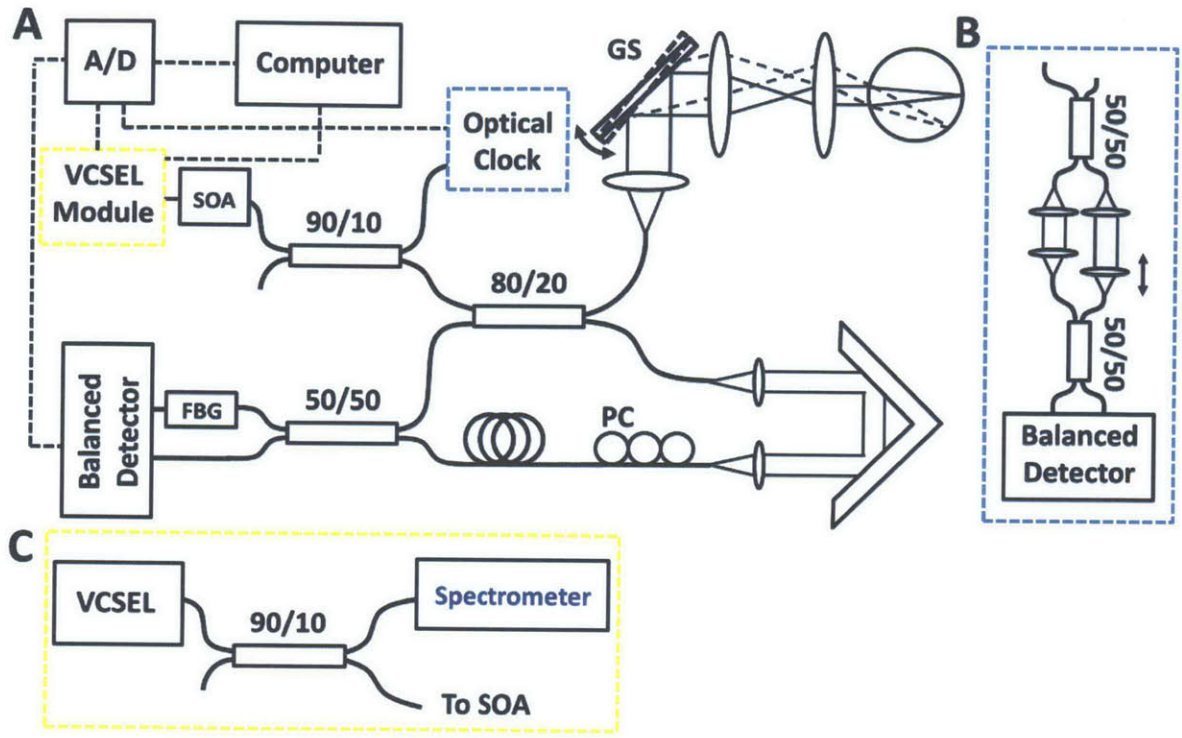

Figure 8.5 VCSEL clinical system schematic. (A) An optically clocked swept-source / Fourier domain OCT setup with a fiber Bragg grating before the balance detection to correct for trigger jittering. (B) Mach-Zehnder interferometer setup used as a dispersion-free optical delay with a balanced detector to generate the optical clock signal. (C) A spectrometer was used to monitor the VCSEL spectrum and control the driving voltage automatically in real-time. A/D – analog-to-digital converter, VCSEL – vertical cavity surface-emitting laser, GS – galvanometric scanners, SOA – booster optical amplifier, FBG – fiber Bragg grating.

8.4 Conclusions

In conclusion, this thesis has demonstrated that advancement in OCT technology has the possibility of opening new avenues to both clinical diagnosis and understanding of diseases in the eye. The development of ultrahigh speed, ultrahigh resolution imaging using spectral / Fourier domain OCT and ultrahigh speed, ultralong range imaging using swept-source / Fourier domain OCT may enable finding structural and functional markers for disease. Future development of swept-source laser technology at 840 nm wavelengths may enable ultrahigh speed, ultrahigh resolution, and ultralong range imaging of the eye. The collaboration between physicians, engineers, and statisticians to perform long-term clinical studies will be an important step towards demonstrating the utility of advanced OCT technology as a clinical tool in ophthalmology.

8.5 References

1. Baumann B, Potsaid B, Kraus MF, Liu JJ, Huang D, Hornegger J, Cable AE, Duker JS, Fujimoto JG. Total retinal blood flow measurement with ultrahigh speed swept source/Fourier domain OCT. Biomed Opt Express. 2011;2(6):1539-52.

2. Choi W, Baumann B, Liu JJ, Clermont AC, Feener EP, Duker JS, Fujimoto JG. Measurement of pulsatile total blood flow in the human and rat retina with ultrahigh speed spectral/Fourier domain OCT. Biomedical Optics Express. 2012;3(5):1047-61. PubMed PMID: ISI:000303537400019.

3. Jia YL, Tan O, Tokayer J, Potsaid B, Wang YM, Liu JJ, Kraus MF, Subhash H, Fujimoto JG, Hornegger J, Huang D. Split-spectrum amplitude-decorrelation angiography with optical coherence tomography. Optics Express. 2012;20(4):4710-25. PubMed PMID: ISI:000301041900134.